Ph D. Thesis

Crystal Structures and Mechanical Properties of Luminescent Gold(I) Complexes

Hokkaido University
Graduate School of Chemical Science and Engineering
Organoelement Chemistry Laboratory

Chi Feng

Contents

I General Introduction

1.1. Mechanical properties of molecular crystals

Crystals play an essential role in modern technology. Organic crystals have attracted much attention in optical and optoelectronic applications because of their anisotropic photophysical properties, intense luminescence, and high carrier mobility.[1–3] However, owing to the weak intermolecular interactions, most organic crystals are usually brittle and fracture when external stresses are applied (**Figure 1**). This fragility destroys the long-range structural order of the crystal and thus its photophysical and electrical properties.[1] Moreover, the fragility of organic crystals leads to severe limitations for the actual application, particularly in flexible optical and optoelectronic devices. Recently, mechanically deformable molecular crystals are becoming new attractive targets because of their properties as both flexible and functional substances, offering them prospects for practical applications.[4–13] For example, flexible electronics are made possible by the mechanical properties of organic semiconductors.[3, 13] In the pharmaceutical industry, the study of the mechanical properties of drugs has facilitated the loading of trays and formulations.[14]

Elasticity and plasticity are used to describe the mechanical flexibility of solid materials (Figure 1).[15–22] Single crystals that can be plastically bent will retain their deformed shape permanently, while single crystals that are elastically bendable will recover their original shape after the applied force is removed. Whether molecular crystals can bend elastically or plastically is closely related to their crystal structure. The crystal structure characteristics of brittleness, elasticity, and plasticity have been summarized based on the discovery of a large number of flexible crystals.[15–22]

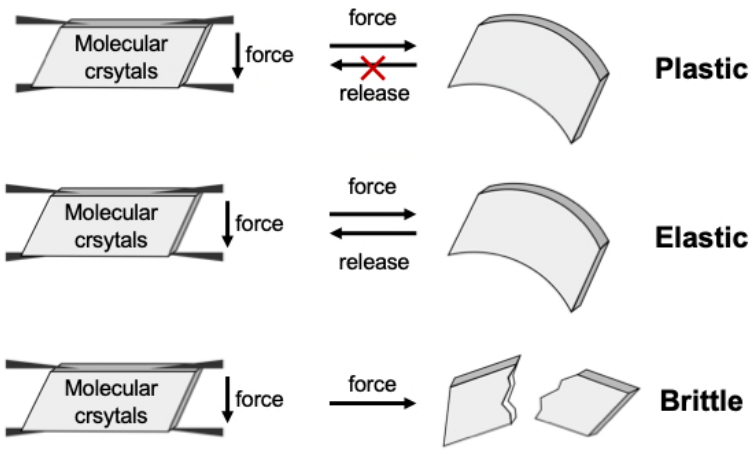

Figure 1. Mechanical properties of organic crystals.

The effect of stress on a molecular crystal is characterized by a stress-strain curve that determines whether the crystal is classified as elastic or plastic. All materials exhibit some degree of mechanical elastic behavior when an external force is applied. In one dimension, strain (ε) is defined as the change in length of the material as a result of the caused deformation (Equation (1)). This generates an internal stress (σ) in the material, the ratio of force to cross-sectional area (Equation (2)). Deformation is elastic (reversible) when the ratio of stress and strain is a constant, and this constant is called the Young's modulus (Y or E, Equation (3)).

$$\varepsilon = \frac{\Delta l}{l_0} \quad (1)$$

$$\sigma = \frac{F}{A} \quad (2)$$

$$\sigma = Y\varepsilon \quad (3)$$

Nanoindentation, a well-established instrumental technique in materials science, can be used to study the mechanical properties of macro- and nanoscale crystals and to characterize the Young's modulus.[23–25] Thus, nanoindentation can be used to systematically evaluate the structure-mechanical property correlations of molecular crystals. As shown in Figure 2, although elasticity and plasticity are defined by the main macroscopic behaviors observed, all materials have a certain degree of elasticity. Once a certain internal stress is reached, either the material fractures or the mechanical response becomes irreversible (plastic). It is called the yield point when this occurs (Figure 2). Although all materials have some elastic behavior, not all materials exhibit plastic deformation.[26]

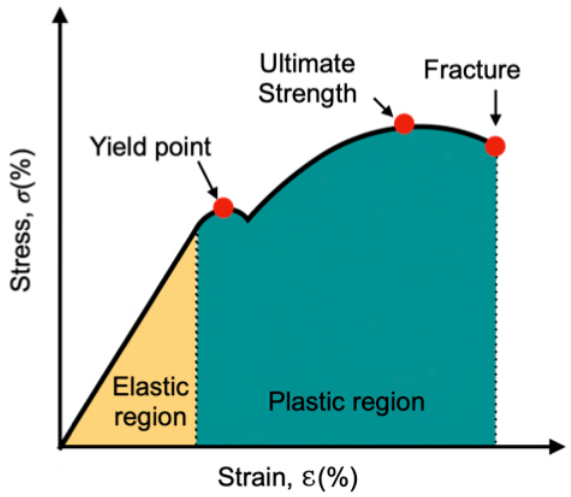

Figure 2. A typical stress–strain curve of a material with both elastic and plastic behavior.

Single crystal X-ray diffraction analysis is an important measurement technique that allows us to understand why some molecular materials exhibit elastic behavior while others exhibit plastic behavior.[27] Single crystal data can also provide detailed information about structural changes in deformed crystals by measuring the crystals after deformation (Figure 3).[28] The recently established micro-focused X-ray technique determines the changes in the crystal structure during bending and finally allows to determine the deformation mechanism.[22]

Mechanical properties can also be studied using other techniques, such as IR and micro-Raman spectroscopy, to gain insight into the deformation mechanisms.[25]

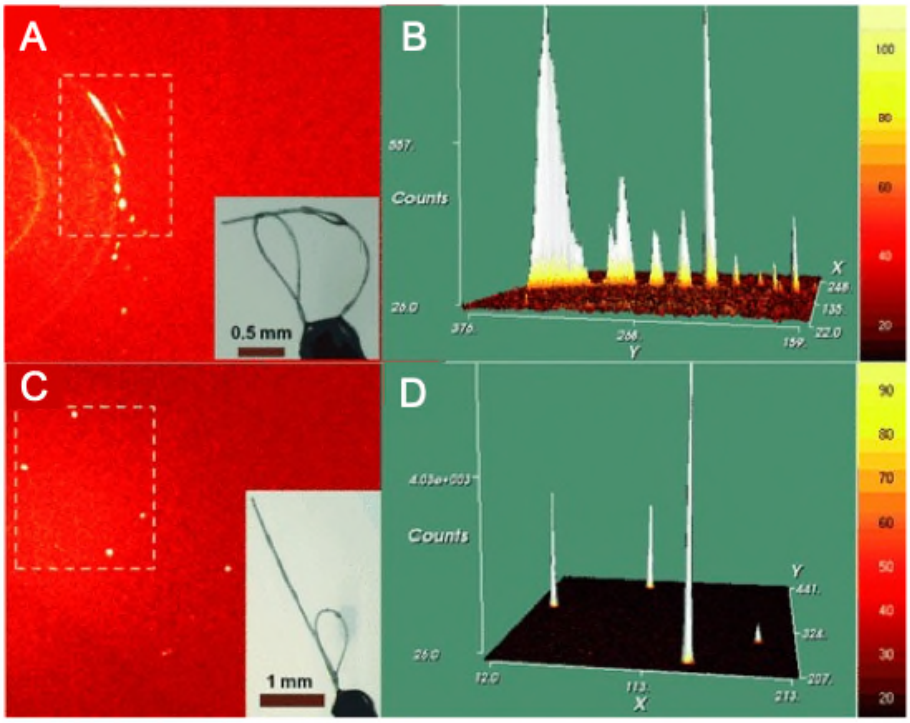

Figure 3. X-ray measurement of elastic crystals. A) Diffraction image of a bent crystal mounted on a nylon ring. B) 3D view of the region marked in (A) shows a clear elongation of the reflection. C) Diffraction image of a mechanically relaxed crystal. D) the region marked in (C). Figure adapted and reproduced from Ref. 28 with permission.

1.2 Elastic and plastic crystals

To date, a large number of examples of elastic crystals have been reported. A wide variety of organic molecules and coordination complexes[22,29,30] have been identified which include single-component crystals[8,31–45] and multi-component systems (co-crystals) [28,46–47] (Figure 4). Most organic

crystals are discovered by chance. They have also been obtained by screening a series of compounds with functional groups similar to those of known elastic crystals.[41–45] In general, it takes a considerable amount of time and effort to discover elastic crystals. The crystal structure characteristics of elasticity have been summarized based on the discovery of a large number of flexible crystals. The structure of these elastic crystals suggests that the elasticity of molecular crystals requires: 1) Interlocking but non-rigid structure that should be interlocked to suppress long distance displacement within the crystal, 2) Near-isotropic packing structures, 3) Buffering region, typically consisting of weak dispersive interactions, that accommodates stress without permanent slippage of molecules, and 4) Reversible movement of parallel domains with change in there intermolecular distance.[18] Significant progress has been made in predicting mechanical properties by understanding structure-mechanical property relationships.

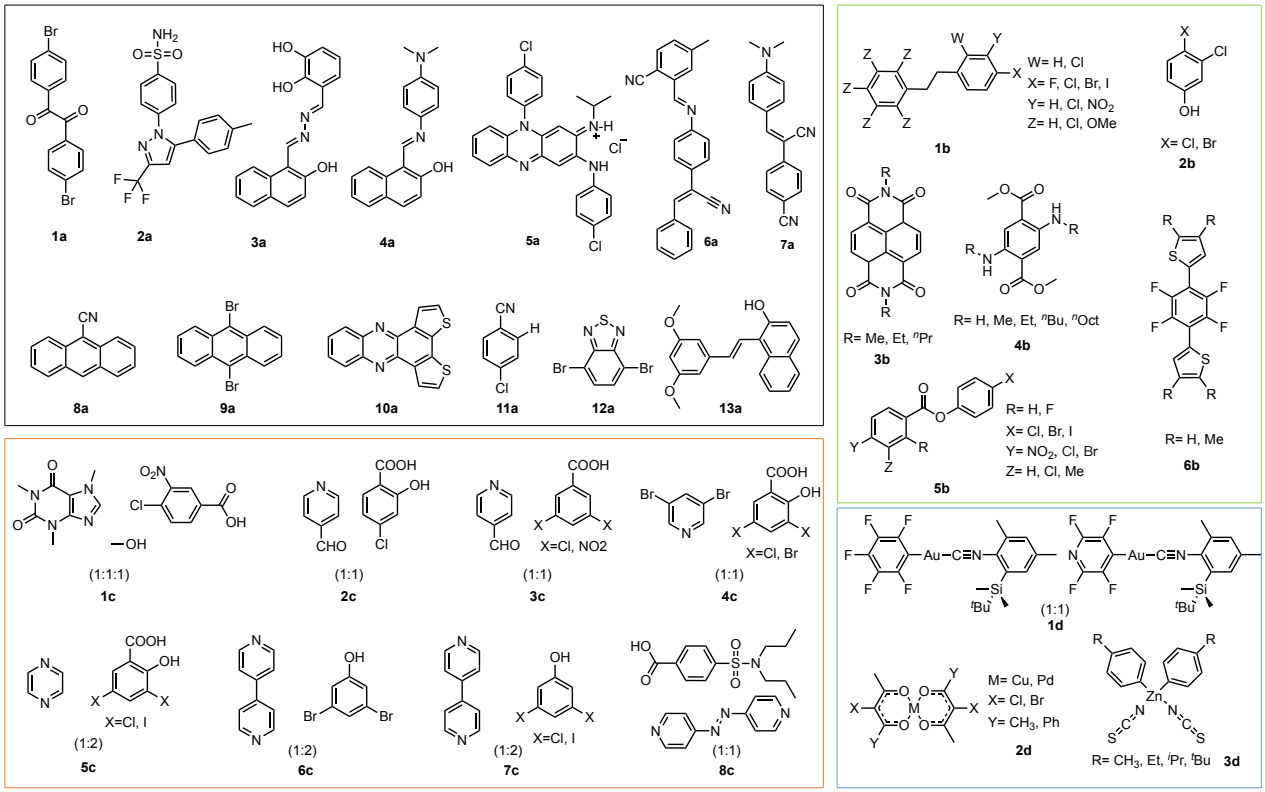

Figure 4. Chemical structures of reported elastic crystals. Organic crystals with single component (**1a**–**13a**), co-crystals (**1c**–**8c**), organometallic complexes (**1d** and **2d**). And small structural changes alter the mechanical properties (plasticity, elasticity, brittleness) of organic crystals (**1b**–**6b**).

The first example of elastic crystals was reported by Reddy and co-workers in 2012.[28] The crystals consist of a co-crystal of caffeine, 4-chloro-3-nitrobenzoic acid, and methanol solvate (**1c**) (Figure 4). These crystals can fold into loops when applied to external forces and return to their original shape when the forces are removed (Figure 5). An interlocking structural feature and channels of

solvent molecules as well as three-dimensional weak and dispersive interactions can be observed in the unbent crystal structure. Crystals with elasticity are characterized by the absence of significant slip planes and dispersive C-H···π interactions in the crystal stacks (Figure 4C and D). Furthermore, solvent molecules were thought to assist bending by facilitating mobility. The interlocked crystal packing hypothesis suggests that the crystal packing resembles a series of hinges that allow it to contract and expand upon bending (Figure 4E).[18]

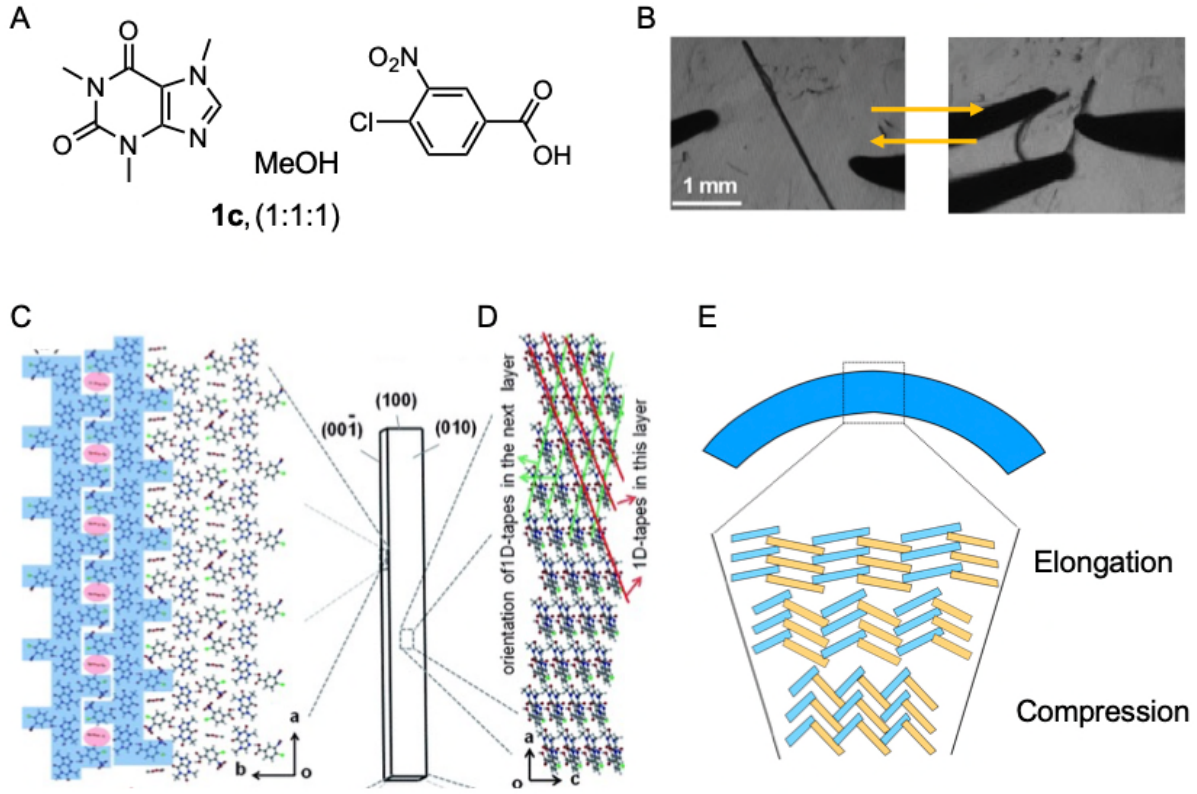

Figure 5. A) Chemical structures of co-crystals **1c**. B) Photographs of the bending crystals of **1c**. C) Interlocked the crystal packing. D) Crystal packing on the (010) face. E) Schematic representation of the interlocked crystal packing mechanism of elastic deformation. Figure adapted and reproduced from Ref. 28 with permission.

Plastic materials usually have structural characteristics of sliding planes, which undergo permanent deformation due to irreversible structural sliding under the action of external forces. Plastic deformation is often observed in metals, which have structures that are easily sliding. Similar to the observations in metals, plastic deformation can be observed in molecular crystals characterized by a sliding plane structure. The plastic deformation in molecular crystals was first observed in single crystals of hexachlorobenzene by Desiraju and co-workers.[48] Subsequently, it was shown to be a general phenomenon. Subsequently, it was shown to be a universal phenomenon along with the discovery of a large number of flexible crystals.[49] And the mechanical properties of the crystals can be

shifted among plasticity, elasticity, and brittleness by structural modification in the substituent groups (Figure 6). The structure of plastic crystals suggests that the plasticity of molecular crystals requires: 1) Crystal structure typically has columnar stacking, 2) Anisotropic structure with strong orientation along the column and weak interaction patterns appearing almost perpendicular to the column, 3) Irreversible migration of molecules along the column without need any significant change in distance.[18]

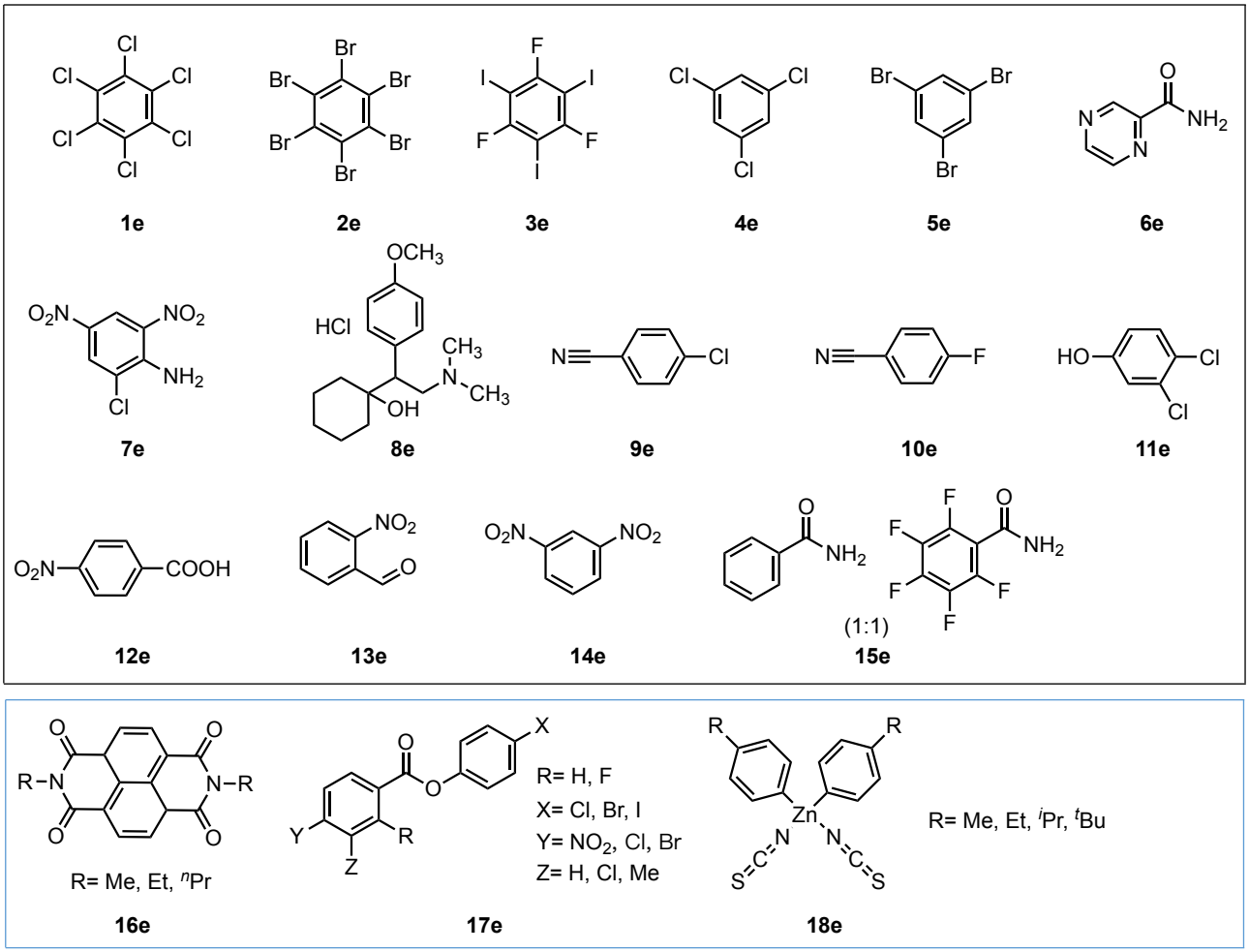

Figure 6. Chemical structures of reported plastic crystals (**1e–15e**). And small structural changes alter the mechanical properties (plasticity, elasticity, brittleness) of organic crystals (**16e**–**18e**).

The first plastic bending example is the crystal of hexachlorobenzene (**1e**).[48] The archetype **1e** exhibits anisotropic bending in that it can only deform along [001] (Figure 7). Anisotropic packing is necessary for plastic deformation. In this crystal, the π-stack columns along the length of the crystal exhibit stronger contacts, and the π-stack columns are linked by weaker Cl···Cl interactions. This plasticity is carried out by separating the bent parts into flexible layers that slide over each other. Diffraction analysis of the bent crystals shows that maintaining crystal integrity when stress is applied at the (001) surface requires sliding layers by breaking and reforming halogen-halogen interactions.

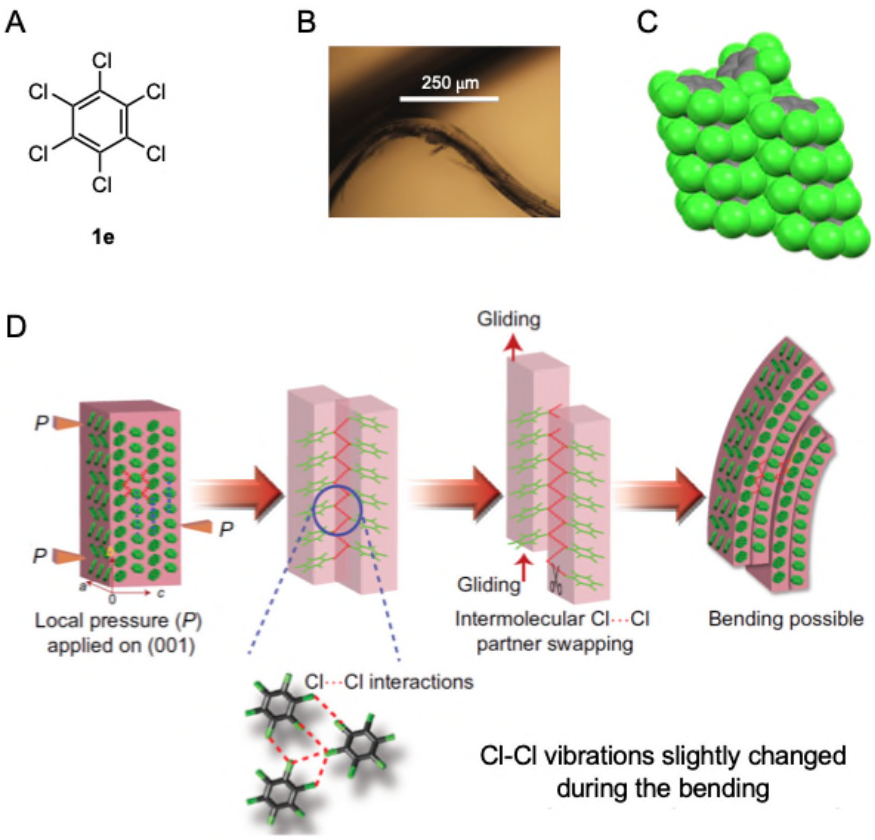

Figure 7. A) Chemical structures of crystals **1e**. B) Photographs of the bending crystals of **1e**. C) columnar stacking of **1e**. D) Schematic mechanism of plastic deformation of **1e**. Figure adapted and reproduced from Ref. 50 with permission.

1.3 Ferroelastic and Superelastic crystals

Recently discovered organic ferroelastic and superelastic crystals that undergo plastic deformation under special cases can also be considered as the flexible crystals (Figure 8). In such systems, stress loading causes deformation twinning or single crystal to single crystal (SCSC) phase transformation.[51-56] Thereby, the stress-strains curves of ferroelasticity and superelasticity are different from the elasticity and plasticity (Figure 9). Figure 9B depicts a typical stress-strain curve for superelastic, which undergoes a phase transition when stress is applied. A moderately deformed superelastic crystal is able to recover its shape by undergoing a reverse SCSC phase transition. A typical elastic material does not dissipate elastic energy and structural phase transformation does not occur during mechanical loading and unloading. On the other hand, superelastic materials partially loss its elastic energy when subjected to an external force because of a phase transition. It is comparable to the well-known martensitic phase transformation in shape memory alloys.[57,58]

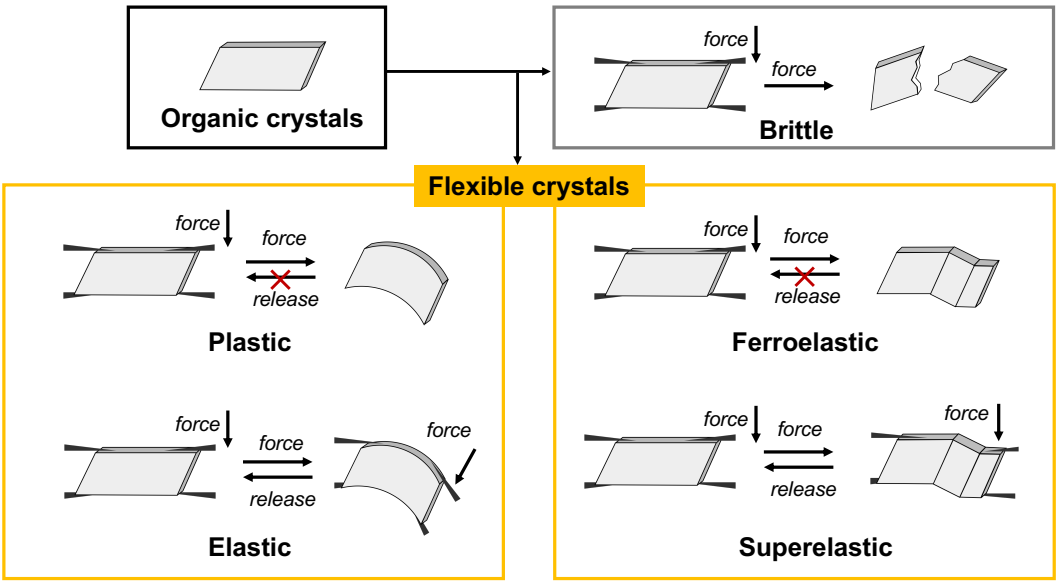

Figure 8. General classification of mechanical properties of molecular crystals.

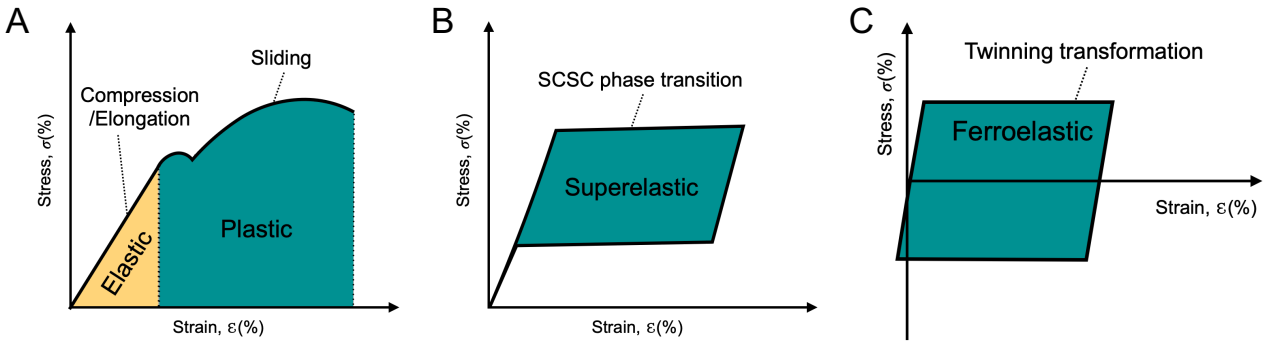

Figure 9. Typical stress-strains curves for elastic, plastic, superelastic, and ferroelastic deformation.

Molecular crystals can also exhibit superelasticity and ferroelasticity, although the intermolecular interactions in molecular solids are significantly different from those in inorganic materials. Perhaps because of the unavailability of sophisticated equipment for mechanical testing, in the absence of studies related to superelasticity and ferroelasticity, the twinning deformation has been reported.[60–62] In 2014, the first organic superelasticity crystal was found in terephthalamide (**1f**) by Takamizawa and co-workers.[52] Subsequently, ferroelasticity was also found in crystals of 5-chloro-2-nitroaniline (**1g**). [63] This research is at an early stage and the number of superelastic[52,54,56, 64–69] and ferroelastic[63,70–73] crystals found so far is small (Figure 10). The reported superelastic and ferroelastic crystals were obtained by scanning from a large number of crystals because the structural features are not well defined. In addition, mechanistic studies are needed to elucidate why some stress-induced phase changes or twinning transformation are accompanied by deformation.

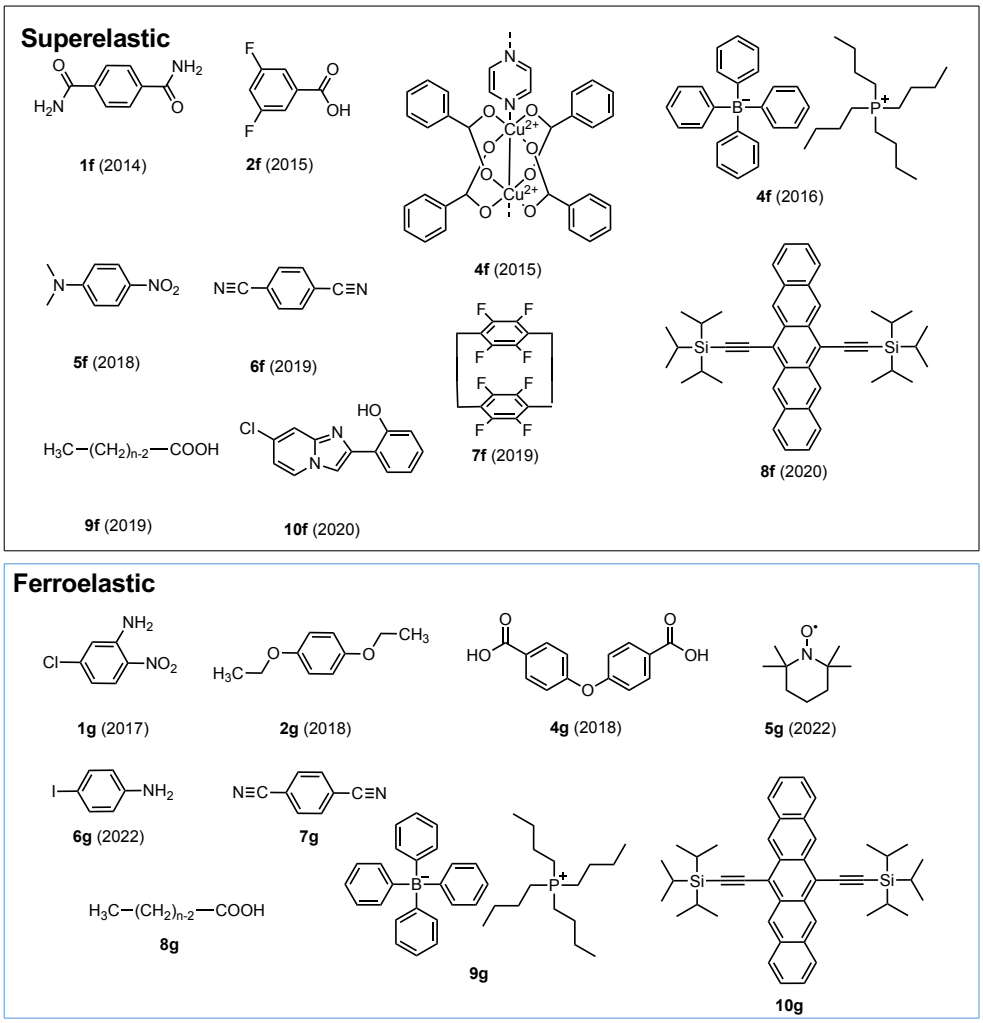

Figure 10. Chemical structures of reported superelastic crystals (**1f–10f**) and ferroelastic crystals (**1g–10g**). The crystals of **4f**, **6f**, **8f**, and **9f** exhibit both superelasticity and ferroelasticity at different temperatures or stress directions.

The superelasticity can be achieved by the SCSC phase transition or twinning. Recently, Takamizawa and co-workers reported superelasticity in organic crystals of terephthalamide (**1f**).[52] External shear stress applied to the crystal **1f** causes bending accompanied by SCSC phase transition. (Figure 11). Notably, the bent crystal spontaneously recovers its original shape after the force is removed by an inverse phase transition, thus demonstrating superelastic behavior. The superelasticity of **1f** is the result of the change of molecular conformation under shear stress. Under the applied stress, the stacking pattern of the crystal **1f** is transformed from the AAAA arrangements (α-phase) to the A'BA'B arrangement (β phase). It may be due to the relatively unstable A'BA'B arrangement, which will transform back to the AAAA arrangements arrangement after the external force disappears. The crystal of 3,5-difluorobenzoic acid (**2f**) also exhibits superelastic behavior; however, instead of SCSC phase transition, twin deformation occurs during bending (Figure 11).[53] Although this bent part (α_1)

and the unbent part (α_1) show different relative molecular orientations, their crystal structures are the same. For the superplastic crystals with twinning deformation, the origin of the recovery stress may be related to a slight molecular conformational change at the interface.[53] Therefore it is of great interest to study in depth the molecular packing/alignment of the intermediate phase at the bending interface.

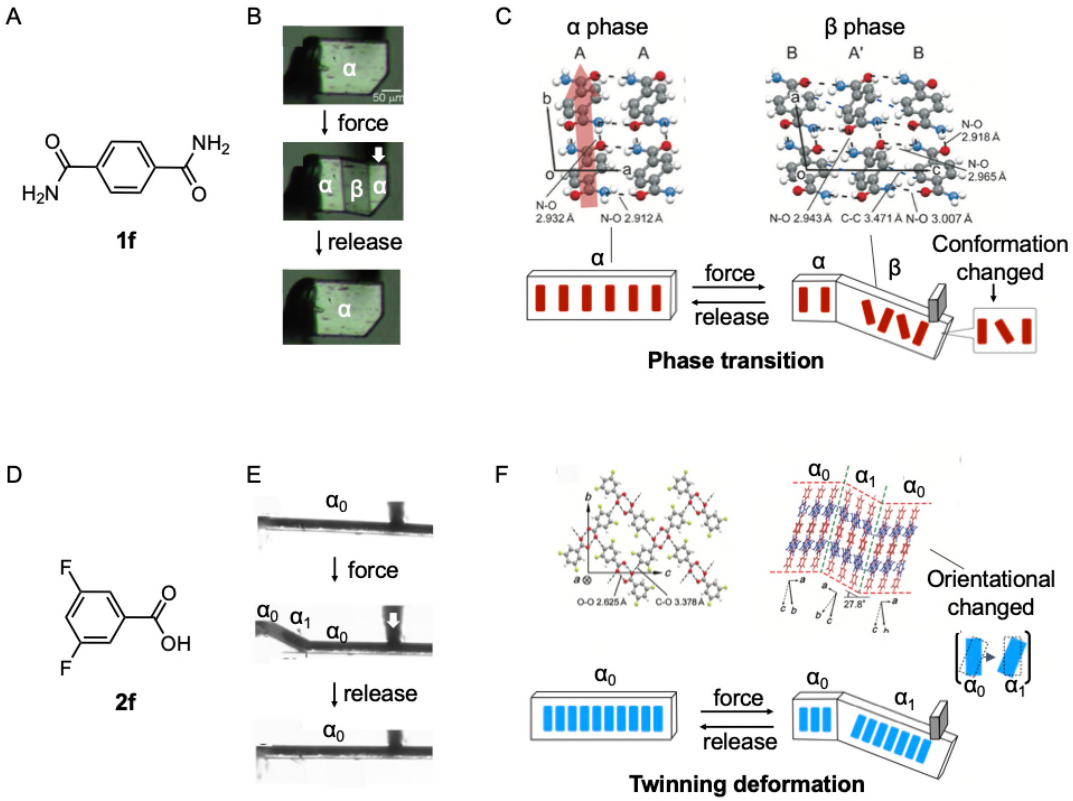

Figure 11. A and D) Chemical structures of crystals **1f** and **2f**. B and E) Photographs of the crystals **1f** and **2f**. C and F) Crystal packing and schematic mechanism of superelastic deformation of **1f** and **2f**. Figure adapted and reproduced from Ref. 52 and 53 with permission.

In most cases, the twinning deformation does not produce a restoring force and it is categorized as ferroelasticity. Crystals of 5-chloro-2-nitro- aniline (**1g**) exhibit ferroelasticity and can be deformed into a zig-zag shape upon application of stress (Figure 12A).[63] The ferroelastic deformation is accompanied by twin transformations in which the bent and unbent parts have the identical crystal structure, but have different relative molecular orientations. The bent shape will not return to its original shape after the external force is released. However, in contrast to the typical plastic deformation, the bent crystal can be recovered to its original shape by applying an external force in the opposite direction. The combination of ferroelasticity and thermal phase transition can provide crystals with a shape memory effect similar to the shape memory properties observed in shape memory alloys. The crystal tetrabutylphosphonium tetraphenylborate (**9g**) exhibits not only ferroelasticity, but also thermal phase transition (Figure 12B).[63] The bent crystals of **9g** could returns to its original shape upon

heating at about 150 °C. Single crystal X-ray diffraction studies indicate that a thermal phase change occurred during the heat treatment process. Moreover, a simple experiment was established to determine the potential of the shape memory effect for practical applications in ferroelastic organic crystals.

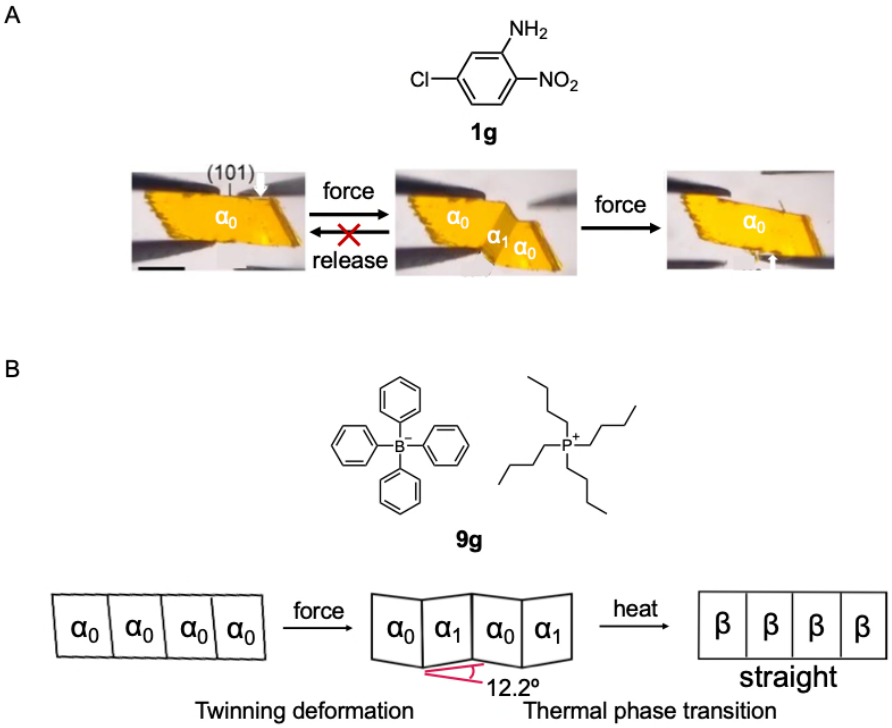

Figure 12. Ferroelasticity in organic crystals. A) The first ferroelastic crystal of 5-chloro-2-nitro-aniline (**1g**). B) The example of shape memory effect in organic crystal tetrabutylphosphonium tetraphenylborate (**9g**).

1.4 Luminescent plastic/elastic/superelastic crystals

So far, many flexible crystals have been reported, but the number of luminescent plastic/elastic crystals is limited and there is only one example of a luminescent superelastic crystal. The luminescence properties of fluorescent molecular crystals are significantly influenced by their packing structure and molecular conformation. This is because their electronic environment determines the photophysical properties of molecular crystals, which are related to inter- and intra-molecular interactions.[74] Because the photophysical properties are related to their electronic environment, changes in the packing structures or molecular conformation can alter their electronic environment. Thus, changes in molecular packing and molecular conformation induced by mechanical deformation can be used to alter their photophysical properties. Controlling the luminescence

properties in the solid phase is a difficult subject because plastic deformation and elastic deformation usually do not lead to significant molecular conformational changes or crystal structure changes. Fortunately, the deformation of superelastic crystals is accompanied by SCSC phase transitions.[52] Luminescent superelastic molecular crystals are expected to be able to change their luminescent color at bent part.

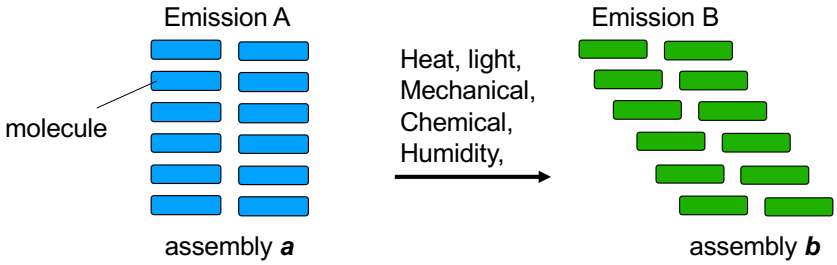

Figure 13. Representation of the external stimulation-responsive luminescence of solid-state molecular materials.

As an example, 9,10-dibromoanthracene (**9b**), which exhibits elastic deformation and green emission, was found to be different from each other in the external (elongated), central (neutral) and internal (contracted) photoluminescence spectra.[37] It was found that straight crystals of **9b** can bend after applying stress and recover to their initial straight shape after removing stress. The photoluminescence spectra of the bent crystals confirm the apparent deformation-induced fluorescence shift; the exterior and interior of the bent crystals show red and blue shifts, respectively (Figure 14). Additionally, XRD analysis and theoretical simulations suggest that the exterior and interior of the bent part show increasing J- and H-aggregation features due to different sliding patterns in the anthracene plane, which could explain the opposite direction of the spectral shift.

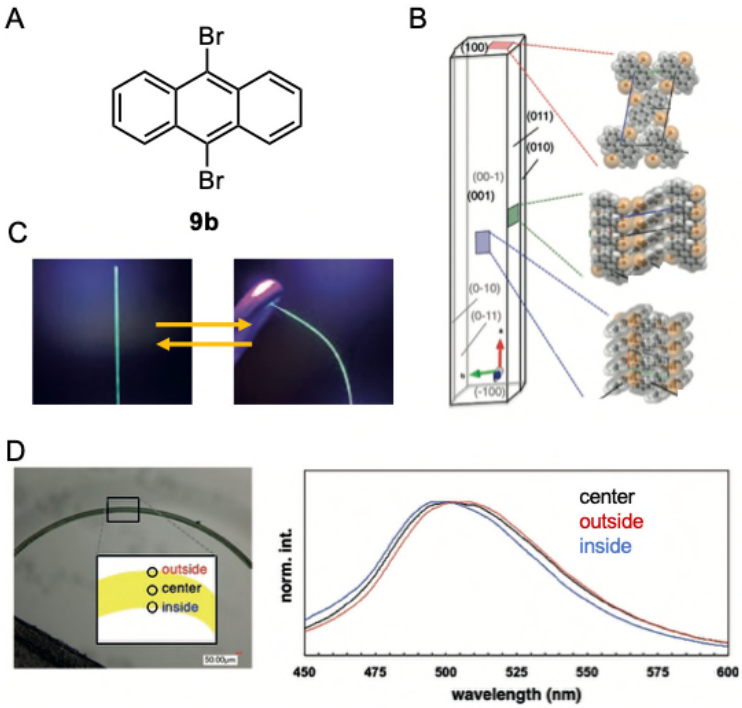

Figure 14. A) Chemical structures of crystals **9b**. B) Its crystal packing with face indices. C) Photographs of the crystals **9b**. D) Microscopic image and emission spectra of the bent crystal **9b** at inside, center, and outside. Figure adapted and reproduced from Ref. 37 with permission.

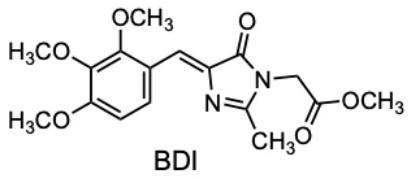

BDI

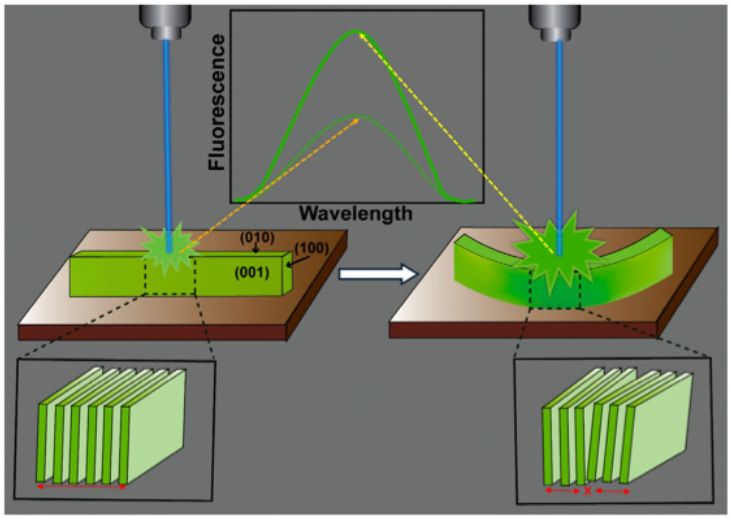

Figure 15. Chemical structures of crystals **BDI** and depiction of fluorescence intensity enhancement in plastic crystals, upon mechanical bending due to plausible strain in the stacking of molecular columns (bottom). Figure adapted and reproduced from Ref. 75 with permission.

Plastic crystals of ethyl[(4Z)-2-methyl-5-oxo-4-(2,3,4-trimethoxybenzylidene)-4,5-dihydro-1H-imidazol-1-yl] (**BDI**) have been reported to enhance luminescence upon mechanical bending.[75] Notably, in mechanically bent crystals of BDI, a clear correlation was observed between the luminescence enhancement and the degree of bending during deformation (Figure 15). The plastic behavior of **BDI** is attributed to the sliding of π-stacking columns in the crystal structure. The discontinuity or weakening of π-π stacking interactions after deformation prevents luminescence quenching and leads to an increase in luminescence intensity.

Superplastic crystals undergo SCSC phase transition in the bent part, which can lead to significant luminescence changes. The first luminescent superelastic example is the crystal of 7-chloro-2-(2'-hydroxyphenyl)imidazo[1,2-a]pyridine (**10f**).[69] The luminescence of **10f** in the solid state is related to the excited state intramolecular proton transfer upon photoexcitation. Therefore, the luminescence of **10f** is sensitive to the crystal structure. The superelastic crystal of **10f** was mechanically stimulated to undergo a single-crystal-to-single-crystal phase transition, resulting in a change in luminescence color at the bent part (Figure 16). Interestingly, the ratio of the two-color luminescence of **10f** can be arbitrarily controlled by shear stress.

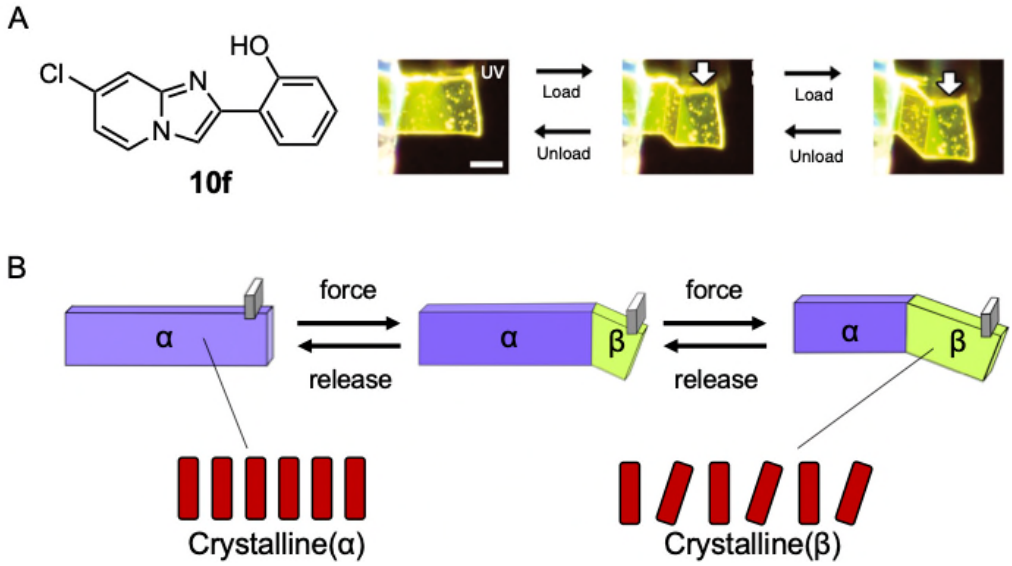

Figure 16. A) Chemical structures and photographs of crystals **10f**. B) Schematic mechanism of superelastic deformation of **10f**. Figure adapted and reproduced from Ref. 69 with permission.

1.5 Mechanical stimuli responsive luminescent gold(I) complexes

Luminescent materials of organic crystals are attracting attention because their luminescent properties vary depending on their crystal structure and assembly state.[76–83] Among these, the

development of solid-state light-emitting materials whose luminescence properties can be switched by mechanical stimulation such as "rubbing" or "grinding" with a spatula or mortar has been actively studied in recent years. The phenomenon in which the luminescence color of a solid changes when mechanically stimulated is called luminescent mechanochromism. The factor that causes the luminescence color to change is the change in crystal structure that occurs upon mechanical stimulation. In the case of solid-state light-emitting materials whose luminescence color is affected by intermolecular interactions, the luminescence color also changes when the crystal structure is altered by mechanical stimulation. These mechanochromic molecules have potential applications in memory and sensor materials that respond to mechanical stimuli. This research is still in its early stages, and detailed studies to develop new mechanochromic molecules and to elucidate their luminescence properties are essential.

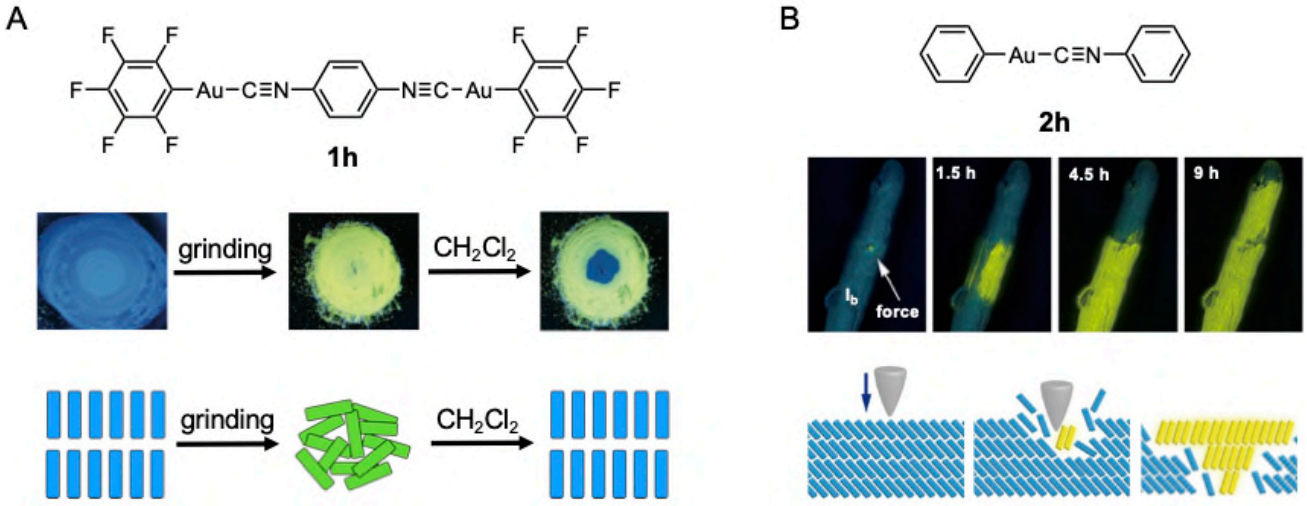

Figure 17. Examples of mechanical stimuli responsive luminescent gold(I) isocyanide complexes corresponding to the crystal structure transformation. A) Chemical structures and photographs of crystals **1h**. B) Chemical structures and photographs of crystals **2h**. Figure adapted and reproduced from Ref. 84 and 85 with permission.

Organometallic compounds are often used to design mechanochromic molecules because the emission properties of the complexes are often greatly altered due to the formation of metal-metal interactions. For example, the mechanochromism in gold(I) isocyanide complex was first reported in 2008.[84] The synthesized powder gold(I) isocyanide complex of [(C6F5Au)2(μ-1,4-Diisocyanobenzene)] (**1h**) immediately showed a blue luminescence under UV light irradiation (Figure 17A). When **1h** was ground with a spatula or mortar, the color of the emission changed to yellow. When dichloromethane was added dropwise to the grinded **1h**, the color of the emission changed from yellow to blue. The mechanism of luminescence color change is the change of crystal structure. The **1h** before grinding was a crystalline powder, while the **1h** powder after grinding was non-crystalline. The structurally simple phenyl(phenyl isocyanide)gold(I) complex (**2h**) was an example of the mechanochromic material with a mechanically stimulated SCSC phase transition.[85] Upon local

stimulation of single crystal **2h** with a needle, the emitted color changes to yellow only in the stimulated region (Figure 17B). This yellow emitting domain spontaneously propagates to the surrounding area and eventually transforms the entire crystal. Under mechanical stimulation, the crystal **2h** exhibits a SCSC phase transition, which leads to a change in the crystal structure. The emission color changed due to the Au-Au interaction formed in the structure after the phase transition. Recently, compounds of **3h** that change their ligands from isocyanates to *N*-heterocyclic carbene (NHC) have been found to exhibit the mechaochromism (Figure 18).[86]

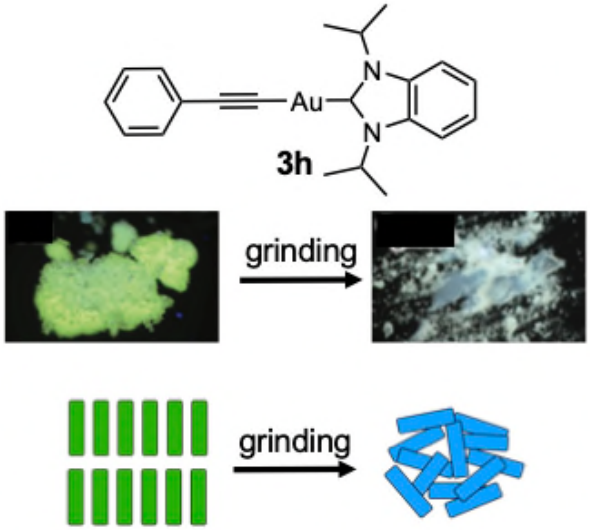

Figure 18. Example of mechanical stimuli responsive luminescent gold(I) *N*-heterocyclic carbene (NHC) complexes corresponding to the crystal structure transformation. A) Chemical structures and photographs of crystals **3h**. Figure adapted and reproduced from Ref. 86 with permission.

1.6 Overview

None of the ferroelasticity of organometallic complexes showing luminescent properties has been reported so far. I focus on NHC gold complexes to achieve ferroelastic molecular crystals that exhibit luminescent properties. Gold(I) complex crystals have previously reported characteristics of molecules exhibiting ferroelasticity, such as linear coordination geometry, chemical stability in air, small NHC ligands, and good crystallinity. The gold(I) complexes are also known to exhibit luminescent mechanochromism upon external stimuli. Based on previous studies of gold (I) complexes containing these isocyanides and NHC ligands, I have found the first ferroelastic behavior of in the luminescent NHC gold(I) complexes **1i** (Figure 19A). Interestingly, NHC Au(I) complexes of **1j**, also exhibit ferroelasticity and show reversible shape-changing effects with luminescent color changes (Figure 19B).

Chapter 2 describes the ferroelastic properties of NHC gold (I) complexes that exhibit luminescent properties.[87] In order to achieve materials with both ferroelasticity and luminescent properties, I prepared NHC gold complexes with various structures and investigated their mechanical properties. It was found that NHC gold complex **1i** exhibited ferroelasticity (Figure 19A). When the

crystals of gold complex **1i** were subjected to pressure, they did not fracture and instead bent. The results of the X-ray structural analysis confirmed that the crystals show twinning deformation. The investigation of the stress-strain properties revealed that the crystals exhibit spontaneous strain. Hysteresis can be observed in the stress-strain curves.

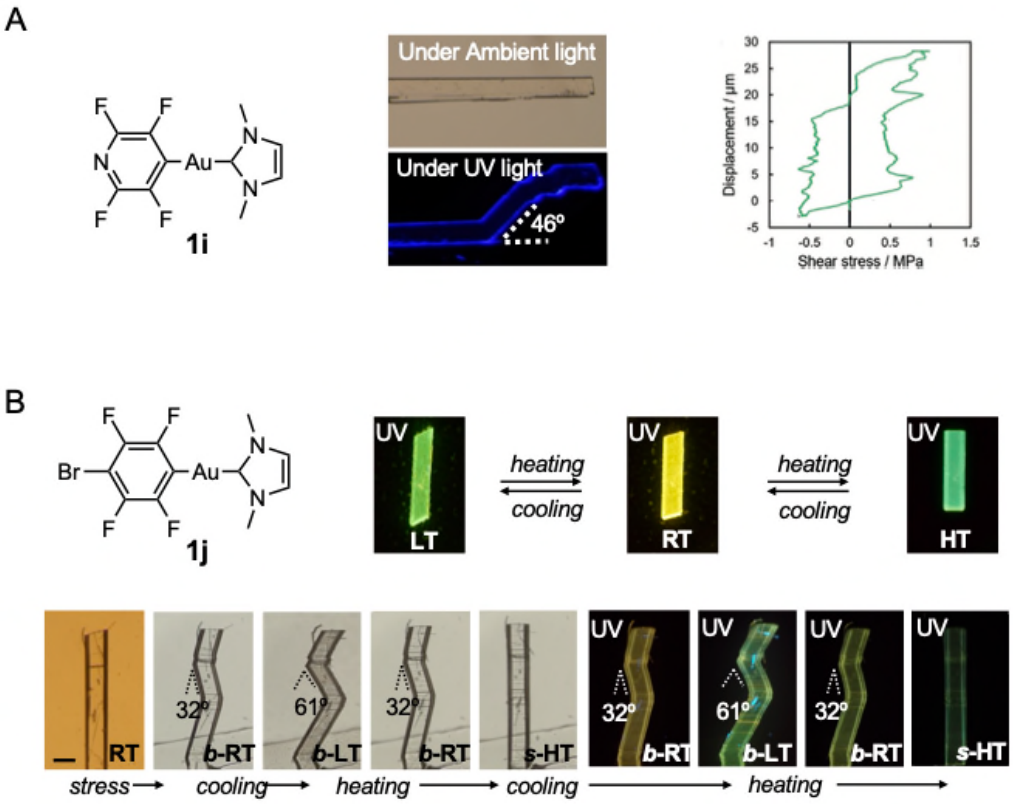

Figure 19. A) Graphical abstract of Chapter 2. B) Graphical abstract of Chapter 3.

Chapter 3 describes a reversible multi-stage shape-changing effect in a mechanically bent molecular crystal with reversible shape change and luminescent color change induced by a multi-step thermal phase transition (Figure 19B).[88] Using single-crystal structure and thermal analyses as well as mechanical property measurements, I found that the reversible multi-stage shape-changing effect was achieved by a combination of a twinning deformation and multi-step thermal phase transitions. It is suggested novel strategies for imparting known shape-memory materials with additional functionalities.

1.6 References

[1]. Wang, Y.; Sun, L.; Wang, C.; Yang, F.; Ren, X.; Zhang, X.; Dong, H.; Hu, W. Organic crystalline materials in flexible electronics. *Chem. Soc. Rev.* **2019**, *48*, 1492–1530.

[2]. Catalano, L.; Commins, P.; Schramm, S.; Karothu, D. P.; Rezgui, R.; Hadef, K.; Naumov, P. Filled organic crystal as hybrid large-bandwidth optical waveguide. *Chem. Commun.* **2019**, *55*, 4921–4924.

[3]. Chen, Y.; Chang, Z.; Zhang, J.; Gong, J. Bending for Better: Flexible Organic Single Crystals with Controllable Curvature and Curvature-Related Conductivity for Customized Electronic Devices. *Angew. Chem. Int. Ed.* **2021**, *60*, 22424–22431.

[4]. Ahmed, E.; Karothu, D. P.; Naumov, P. Crystal adaptronics: mechanically reconfigurable elastic and superelastic molecular crystals. *Angew. Chem. Int. Ed.* **2018**, *57*, 8837–8846.

[5]. Khalil, A.; Ahmed, E.; Naumov, P. Metal-coated thermosalient crystals as electrical fuses. *Chem. Comm.* **2017**, *53*, 8470–8473.

[6]. Liu, B.; Liu, W.; Wang, C.; Wang, Y.; Zhang, H. Red-Emissive Organic Crystals of a Single-Benzene Molecule: Elastically Bendable and Flexible Optical Waveguide. *J. Phys. Lett.* **2019**, *10*, 1437–1442.

[7]. Panda, M. K.; Ghosh, S.; Yasuda, N.; Moriwaki, T.; Mukherjee, G. D.; Reddy, C. M.; Naumov, P. Spatially resolved analysis of short-range structure perturbations in a plastically bent molecular crystal. *Nat. Chem.* **2015**, *7*, 65–72.

[8]. Wang, K.; Mishra, M. K.; Sun, C. C. Exceptionally Elastic Single-Component Pharmaceutical Crystals. *Chem. Mater*. **2019**, *31*, 1794–1799.

[9]. Liu, B.; Lu, Z.; Tang, B.; Liu, H.; Liu, H.; Zhang, Z.; Ye, K.; Zhang, H. Self-Waveguide Single-Benzene Organic Crystal with Ultralow-Temperature Elasticity as a Potential Flexible Material. *Angew. Chem. Int. Ed.* **2020**, *59*, 23117–23121.

[10]. Annadhasan, M.; Basak, S.; Chandrasekhar, N.; Chandrasekar, R. Next-Generation Organic Photonics: The Emergence of Flexible Crystal Optical Waveguides. *Adv Opt Mater.* **2020**, *8*, 2000959.

[11]. Hayashi, S.; Koizumi, T. Elastic Organic Crystals of a Fluorescent π-Conjugated Molecule. *Angew. Chem. Int. Ed.* **2016**, *55*, 2701–2704.

[12]. Kenny, E. P.; Jacko, A. C.; Powell, B. J. Mechanomagnetics in Elastic Crystals: Insights from [Cu(acac)2]. *Angew. Chem. Int. Ed.* **2019**, *58*, 15082–15088.

[13]. Tang, Q.; Tong, Y.; Zheng, Y.; He, Y.; Zhang, Y.; Dong, H.; Hu, W.; Hassenkam, T.; Bjørnholm, T.; Organic Nanowire Crystals Combine Excellent Device Performance and Mechanical

Flexibility. *Small* **2022**, *7*, 189–193.

[14]. Sun, C. C. Decoding Powder Tabletability: Roles of Particle Adhesion and Plasticity. J. *Adhes. Sci. Technol*. **2011**, *25*, 483–499.

[15]. Naumov, P.; Chizhik, S.; Panda, M. K.; Nath, N. K.; Boldyreva, E. Mechanically Responsive Molecular Crystals. *Chem. Rev.* **2015**, *115*, 12440–12490.

[16]. Das, S.; Mondal, A.; Reddy, C. M. Harnessing molecular rotations in plastic crystals: a holistic view for crystal engineering of adaptive soft materials. *Chem. Soc. Rev*. **2020**, *49*, 8878–8896.

[17]. Thompson, A. J.; Chamorro Orué, A. I.; Nair, A. J.; Price, J. R.; McMurtrie, J.; Clegg, J. K. Elastically flexible molecular crystals. *Chem. Soc. Rev.* **2021**, *50*, 11725–11740.

[18]. Saha, S.; Mishra, M. K.; Reddy, C. M.; Desiraju, G. R. From Molecules to Interactions to Crystal Engineering: Mechanical Properties of Organic Solids. *Acc. Chem. Res.* **2018**, *51*, 2957–2967.

[19]. Reddy, C. M.; Gundakaram, R. C.; Basavoju, S.; Kirchner, M. T.; Padmanabhan, K. A.; Desiraju, G. R. Structural basis for bending of organic crystals. *Chem. Commun.* **2005**, 3945–3947.

[20]. Commins, P.; Karothu, D. P.; Naumov, P. Is a Bent Crystal Still a Single Crystal?. *Angew. Chem. Int. Ed.* **2019**, *58*, 10052–10060.

[21]. Panda, M. K.; Ghosh, S.; Yasuda, N.; Moriwaki, T.; Mukherjee, G. D.; Reddy, C. M.; Naumov, P. Spatially resolved analysis of short-range structure perturbations in a plastically bent molecular crystal. *Nat. Chem*. **2015**, *7*, 65–72.

[22]. Worthy, A.; Grosjean, A.; Pfrunder, M. C.; Xu, Y.; Yan, C.; Edwards, G.; Clegg, J. K.; McMurtrie, J. C. Atomic resolution of structural changes in elastic crystals of copper(II) acetylacetonate. *Nat. Chem.* **2017**, *10*, 65–69.

[23]. Varughese, S.; Kiran, M. S. R. N.; Ramamurty, U.; Desiraju, G. R. Nanoindentation in Crystal Engineering: Quantifying Mechanical Properties of Molecular Crystals. *Angew. Chem. Int. Ed.* **2013**, *52*, 2701–2712.

[24]. Mishra, M. K.; Ramamurty, U.; Desiraju, G. R. Mechanical Property Design of Molecular Crystals. *Curr. Opin. Solid State Mater. Sci.* **2016**, *20*, 361–370.

[25]. Dey, S.; Das, S.; Bhunia, S.; Chowdhury, R.; Mondal, A.; Bhattacharya, B.; Devarapalli, R.; Yasuda, N.; Moriwaki, T.; Mandal, K.; Mukherjee, G. D.; Reddy, C. M. Mechanically interlocked architecture aids an ultra-stiff and ultra-hard elastically bendable cocrystal. *Nat. Commun.* **2019**, *10*, 3711.

[26]. Giacovazzo, C. Fundamentals of Crystallography. *Oxford Press*, Oxford, **2011**.

[27]. Thompson, A. J.; Worthy, A.; Grosjean, A.; Price, J. R.; McMurtrie, J. C.; Clegg, J. K. Determining the mechanisms of deformation in flexible crystals using micro-focus X-ray diffraction. *CrystEngComm*. **2021**, *23*, 5731–5737.

[28]. Ghosh, S.; Reddy, C. M. Elastic and bendable caffeine cocrystals: implications for the design of flexible organic materials. *Angew. Chem. Int. Ed.* **2012**, *51*, 10319–10323.

[29]. Seki, T.; Toyoshima, N.; Ito, H. Mixed crystal formation of two gold isocyanide complexes with various ratios for continuous tuning of photophysical properties. *Dalton Trans.* **2020**, *49*, 2073–2076.

[30]. Tang, Z.; Sun, X.; Wang, S.; Ji, X.; Yao, Z.; Tao, J. Altering elastic-plastic mechanical response of a series of isostructural metal-organic complex crystals. *Sci. China Chem.* 2022, *65*, 710–718.

[31]. Liu, H.; Bian, Z.; Cheng, Q.; Lan, L.; Wang, Y.; Zhang, H. Controllably realizing elastic/plastic bending based on a room-temperature phosphorescent waveguiding organic crystal. *Chem. Sci.* **2019**, *10*, 227–232.

[32]. Saini, A. K.; Natarajan, K.; Mobin, S. M.; A new multitalented azine ligand: elastic bending, single-crystal-to-single-crystal transformation and a fluorescence turn-on Al(iii) sensor. *Chem. Commun.* **2017**, *53*, 9870–9873.

[33]. Horstman, E. M.; Keswani, R. K.; Frey, B. A.; Rzeczycki, P. M.; LaLone, V.; Bertke, J. A.; Kenis, P. J.; Rosania, G. R. Elasticity in Macrophage-Synthesized Biocrystals. *Angew. Chem. Int. Ed.* **2017**, *56*, 1815–1819.

[34]. Liu, H.; Ye, K.; Zhang, Z.; Zhang, H. An Organic Crystal with High Elasticity at an Ultra-Low Temperature (77 K) and Shapeability at High Temperatures. *Angew. Chem. Int. Ed.* **2019**, *58*, 19081–19086.

[35]. Lu, Z.; Zhang, Y.; Liu, H.; Ye, K.; Liu, W.; Zhang, H. Optical Waveguiding Organic Single Crystals Exhibiting Physical and Chemical Bending Features. *Angew. Chem. Int. Ed.* **2020**, *59*, 4299–4303.

[36]. Mishra, M. K.; Kadambi, S. B.; Ramamurty, U.; Ghosh, S. Elastic flexibility tuning via interaction factor modulation in molecular crystals. *Chem. Commun.* **2018**, *54*, 9047–9050.

[37]. Hayashi, S.; Ishiwari, F.; Fukushima, T.; Mikage, S.; Imamura, Y.; Tashiro, M.; Katouda, M. Anisotropic Poisson Effect and Deformation-Induced Fluorescence Change of Elastic 9,10-Dibromoanthracene Single Crystals. *Angew. Chem. Int. Ed.* **2020**, *59*, 16195–16201.

[38]. Annadhasan, M.; Agrawal, A. R.; Bhunia, S.; Pradeep, V. V.; Zade, S. S.; Reddy, C. M.; Chandrasekar, R.; Mechanophotonics: Flexible Single-Crystal Organic Waveguides and

Circuits. *Angew. Chem. Int. Ed.* **2020**, *59*, 13852–13858.

[39]. Rather, S. A.; Saha, B. K. Thermal Expansion Study as a Tool to Understand the Bending Mechanism in a Crystal. *Cryst. Growth Des.* **2018**, *18*, 2712–2716.

[40]. Liu, H.; Lu, Z.; Tang, B.; Qu, C.; Zhang, Z.; Zhang, H. A Flexible Organic Single Crystal with Plastic-Twisting and Elastic-Bending Capabilities and Polarization-Rotation Function. *Angew. Chem. Int. Ed.* **2020**, *59*, 12944–12950.

[41]. Ghosh, S.; Mishra, M. K.; Kadambi, S. B.; Ramamurty, U.; Desiraju, G. R. Designing Elastic Organic Crystals: Highly Flexible Polyhalogenated N-Benzylideneanilines. *Angew. Chem. Int. Ed.* **2015**, *54*, 2674–2678.

[42]. Devarapalli, R.; Kadambi, S. B.; Chen, C. T.; Krishna, G. R.; Kammari, B. R.; Buehler, M. J. Ramamurty, U.; Reddy, C. M. Remarkably Distinct Mechanical Flexibility in Three Structurally Similar Semiconducting Organic Crystals Studied by Nanoindentation and Molecular Dynamics. *Chem. Mater.* **2019**, *31*, 1391–1402.

[43]. Huang, R.; Wang, C.; Wang, Y.; Zhang, H. Elastic Self-Doping Organic Single Crystals Exhibiting Flexible Optical Waveguide and Amplified Spontaneous Emission. *Adv. Mater.* **2018**, *30*, 1800814.

[44]. Hayashi, S.; Koizumi, T. Elastic Organic Crystals of a Fluorescent π-Conjugated Molecule. *Angew. Chem. Int. Ed.* **2016**, *55*, 2701–2704.

[45]. Saha, S.; Desiraju, G. R. Crystal Engineering of Hand-Twisted Helical Crystals. *J. Am. Chem. Soc.* **2017**, *139*, 1975–1983.

[46]. Saha, S.; Desiraju, G. R. σ-Hole and π-Hole Synthon Mimicry in Third-Generation Crystal Engineering: Design of Elastic Crystals. *Chem. Eur. J.* **2017**, *23*, 4936–4943.

[47]. Saha, S.; Desiraju, G. R. Using structural modularity in cocrystals to engineer properties: elasticity. *Chem. Commun.* **2016**, *52*, 7676–7679.

[48]. Reddy, C. M.; Gundakaram, R. C.; Basavoju, S.; Kirchner, M. T.; Padmanabhan, K. A.; Desiraju, G. R. Structural basis for bending of organic crystals. *Chem. Commun.* **2005**, 3945.

[49]. Reddy, C. M.; Padmanabhan, K. A.; Desiraju, G. R. Structure−Property Correlations in Bending and Brittle Organic Crystals. *Cryst. Growth Des.* **2006**, *6*, 2720–2731.

[50]. Panda, M. K.; Ghosh, S.; Yasuda, N.; Moriwaki, T.; Mukherjee, G. D.; Reddy, C. M.; Naumov, P. Spatially resolved analysis of short-range structure perturbations in a plastically bent molecular crystal. *Nat. Chem.* **2015**, *7*, 65–72.

[51]. Karothu, D. P.; Weston, J.; Desta, I. T.; Naumov, P. Shape-memory and self-healing effects in mechanosalient molecular crystals. *J. Am. Chem. Soc.* **2016**, *138*, 13298–13306.

[52]. Takamizawa, S.; Miyamoto, Y. Superelastic organic crystals. *Angew. Chem. Int. Ed.* **2014**, *53*, 6970–6973.

[53]. Takamizawa, S.; Takasaki, Y. Superelastic Shape Recovery of Mechanically Twinned 3,5-Difluorobenzoic Acid Crystals. *Angew. Chem. Int. Ed.* **2015**, *54*, 4815–4817.

[54]. Takasaki, Y.; Takamizawa, S. Active porous transition towards spatiotemporal control of molecular flow in a crystal membrane. *Nat. Commun.* **2015**, *6*, 89346.

[55]. Takamizawa, S.; Takasaki, Y. Shape-memory effect in an organosuperelastic crystal. *Chem. Sci.* **2016**, *7*, 1527–1534.

[56]. Takamizawa, S.; Takasaki, Y. Superelastic Shape Recovery of Mechanically Twinned 3,5-Difluorobenzoic Acid Crystals. *Angew. Chem. Int. Ed*. **2015**, *54*, 4815–4899.

[57]. Ferreira, M. A.; Luersen, M. A.; Borges, P. C. Nickel-titanium alloys: a systematic review. *Dental Press J. Orthod.* **2012**, *17*, 71–82.

[58]. Nayan, N.; Buravalla, V.; Ramamurty, U. Effect of mechanical cycling on the stress–strain response of a martensitic Nitinol shape memory alloy. *Mater. Sci. Eng. A* **2009**, *525*, 60–67.

[59]. Schwenk, H.; Neumair, K.; Andres, K.; Wudl, F.; Aharon-Shalom, E. Meissner Anisotropy in Deuterated $(TMTSF)_2ClO_4$ *Mol. Cryst. Liq. Cryst.* **1982**, *79*, 633–638.

[60]. Reddy, C. M.; Kirchner, M. T.; Gundakaram, R. C.; Padmanabhan, K. A.; Desiraju, G. R. Isostructurality, Polymorphism and Mechanical Properties of Some Hexahalogenated Benzenes: The Nature of Halogen···Halogen Interactions. *Chem. Eur. J.* **2006**, *12*, 2222–2234.

[61]. Bandyopadhyay, R.; Grant, D. J. W. Plasticity and Slip System of Plate-Shaped Crystals of L-Lysine Monohydrochloride Dihydrate. *Pharm. Res.* **2002**, *19*, 491–496.

[62]. Williams-Seton, L.; Davey, R. J.; Lieberman, H. F.; Pritchard, R. G. Disorder and twinning in molecular crystals: impurity‐induced effects in adipic acid. *J. Pharm. Sci.* **2000**, *89*, 346–354.

[63]. Mir, S. H.; Takasaki, Y.; Engel, E. R.; Takamizawa, S. Ferroelasticity in an Organic Crystal: A Macroscopic and Molecular Level Study. *Angew. Chem. Int. Ed*. **2017**, *56*, 15882–15885.

[64]. Takamizawa, S.; Takasaki, Y.; Sasaki, T.; Ozaki, N. Superplasticity in an organic crystal. *Nat. Commun.* **2018**, *9*, 3984.

[65]. Sakamoto, S.; Sasaki, T.; Sato-Tomita, A.; Takamizawa, S. Shape rememorization of an organosuperelastic crystal through superelasticity-ferroelasticity interconversion. *Angew. Chem. Int. Ed.* **2019**, *58*, 13722–13726.

[66]. Sasaki, T.; Sakamoto, S.; Takamizawa, S. Twinning organosuperelasticity of a fluorinated cyclophane single crystal. *Cryst. Growth Des.* **2019**, *19*, 5491–5493.

[67]. Park, S. K.; Sun, H.; Chung, H.; Patel, B. B.; Zhang, F.; Davies, D. W.; Woods, T. J.; Zhao, K.;

Diao, Y. Super- and ferroelastic organic semiconductors for ultraflexible single-crystal electronics. *Angew. Chem. Int. Ed.* **2020**, *59*, 13004–13012.

[68]. Takamizawa, S.; Takasaki, Y. Versatile shape recoverability of odd-numbered saturated long-chain fatty acid crystals. *Cryst. Growth Des.* **2019**, *19*, 1912–1920.

[69]. Mutai, T.; Sasaki, T.; Sakamoto, S.; Yoshikawa, I.; Houjou, H.; Takamizawa, S, A superelastochromic crystal. *Nat. Commun.* **2020**, *11*, 1824.

[70]. Engel, E. R.; Takamizawa, S. Versatile ferroelastic deformability in an organic single crystal by twinning about a molecular zone axis. *Angew. Chem. Int. Ed.* **2018**, *57*, 11888–11892.

[71]. Engel, E. R.; Takasaki, Y.; Mir, S. H.; Takamizawa, S. Twinning ferroelasticity facilitated by the partial flipping of phenyl rings in single crystals of 4,4'-dicarboxydiphenyl ether. *R. Soc. Open Sci.* **2018**, *5*, 171146.

[72]. Ranjan, S.; Takamizawa, S. Characterization of Organoferroelasticity in a TEMPO Crystal. *Cryst. Growth Des.* **2022**, *22*, 585–589.

[73]. Ranjan, S.; Takamizawa, S. Two-Dimensional Organoferroelasticity in a Single Crystal of 4-Iodoaniline. *Cryst. Growth Des.* **2022**, *22*, 1831–1836.

[74]. Mutai, T.; Satou, H.; Araki, K. Reproducible on–off switching of solid-state luminescence by controlling molecular packing through heat-mode interconversion. Nat. Mater. **2005**, *4*, 685–687.

[75]. Bhattacharya, B.; Roy, D.; Dey, S.; Puthuvakkal, A.; Bhunia, S.; Mondal, S.; Chowdhury, R.; Bhattacharya, M.; Mandal, M.; Manoj, K.; Mandal, P. K.; Reddy, C. M. Mechanical-bending-Induced fluorescence enhancement in plastically flexible crystals of a GFP chromophore analogue. *Angew. Chem. Int. Ed.* **2020**, *59*, 19878–19883.

[76]. Zhang, X.; Chi, Z.; Zhang, Yi.; Liu, S.; Xu, J. Recent advances in mechanochromic luminescent metal complexes. *J. Mater. Chem. C.* **2013**, *1*, 3376–3390.

[77]. Sagara, Y.; Yamane, S.; Mitani, M.; Weder, C.; Kato, T. Mechanoresponsive Luminescent Molecular Assemblies: An Emerging Class of Materials. *Adv. Mater.* **2016**, *28*, 1073–1095.

[78]. Chi, Z.; Zhang, X.; Xu, B.; Zhou, X.; Ma, C.; Zhang, Y.; Liu, Siwei.; Xu, J. Recent advances in organic mechanofluorochromic materials. *Chem. Soc. Rev.* **2013**, *41*, 3878–3896.

[79]. Sagara, Y.; Mutai, T.; Yoshikawa, I.; Araki, K.; Material Design for Piezochromic Luminescence: Hydrogen-Bond-Directed Assemblies of a Pyrene Derivative. *J. Am. Chem. Soc.* **2007**, *129*, 1520–1521.

[80]. Sagara, Y.; Kato, T. Mechanically induced luminescence changes in molecular assemblies. *Nat. Chem.* **2009**, *1*, 605–610.

[81]. Sagara, Y.; Yamane, S.; Mutai, T.; Araki, K.; Kato. T. A Stimuli-Responsive, Photoluminescent, Anthracene-Based Liquid Crystal: Emission Color Determined by Thermal and Mechanical Processes. *Adv. Funct. Mater.* **2009**, *19*, 1869–1875.

[82]. Chen, X.; Wei, R.; Xiang, Y.; Zhou, Z.; Li, K.; Song, P.; Tong, A. Organic Crystalline Solids Response to Piezo/thermo Stimulus: Donor–Acceptor (D–A) Attached Salicylaldehyde Azine Derivatives. *J. Phys. Chem. C.* **2011**, *115*, 14353–14359.

[83]. Nagura, K.; Saito, S.; Yusa, H.; Yamazaki, H.; Fujihisa, H.; Sato, H.; Shimoikeda, Y.; Yamaguchi, S. Distinct Responses to Mechanical Grinding and Hydrostatic Pressure in Luminescent Chromism of Tetrathiazolylthiophene. *J. Am. Chem. Soc.* 2013, 135, 10322–10325.

[84]. Ito, H.; Saito, T.; Oshima, N.; Kitamura, N.; Ishizaka, S.; Hinatsu, Y.; Wakeshima, M.; Kato, M.; Tsuge, K.; Sawamura, M. Reversible Mechanochromic Luminescence of [(C6F5Au)2(μ-1,4-Diisocyanobenzene)]. *J. Am. Chem. Soc.* **2008**, *130*, 10044–10045.

[85]. Ito, H.; Muromoto, M.; Kurenuma, S.; Ishizaka, S.; Kitamura, N.; Sato, H.; Seki, T. Mechanical stimulation and solid seeding trigger single-crystal-to-single-crystal molecular domino transformations. *Nat. Commun.* **2013**, *4*, 2009.

[86]. Seki, T.; Kashiyama, K.; Ito, H. Luminescent mechanochromism of gold *N*-heterocyclic carbene complexes with hypso- and bathochromic spectral shifts. *Dalton Trans.* **2019**, *48*, 7105–7109.

[87]. Seki, T.; Feng, C.; Kashiyama, K.; Sakamoto, S.; Takasaki, Y.; Sasaki, T.; Takamizawa, S.; Ito, H. Photoluminescent Ferroelastic Molecular Crystals. *Angew. Chem. Int. Ed.* **2020**, *59*, 8839–8843.

[88]. Feng, C.; Seki, T.; Sakamoto, S.; Sasaki, T.; Takamizawa, S.; Ito, H. Mechanical deformation and multiple thermal restoration of organic crystals: reversible multi-stage shape-changing effect with luminescence-color changes. *Chem. Sci.* **2022**, *13*, 9544–9551.

II Photoluminescent Ferroelasticity in gold(I) complexes

2.1. Introduction

Ferroelasticity refers to a group of ferroic properties that are similar to ferromagnetism and ferroelectricity.[1] In contrast to other ferrite materials, ferroelastic materials alter their crystalline morphology and/or crystal structure and display attractive mechanical properties when exposed to mechanical stress. Ferroelastic crystals show plastic bending when loaded with shear stress to a particular crystal plane. Typically, the appearance of a daughter phase in the bending domain with a change in its relative atomic or molecular orientation, but without a transition to a different crystal structure, indicates twinning. The hysteresis stress-strain curve under the strain established spontaneously during crystal bending is another typical behavior of ferroelastic crystals. These phenomena are well substantiated for inorganic materials.[2,3] In contrast, for organic molecular crystals, only few examples of twinning deformation have been reported.[4] One advantage of the ferroelasticity of organic crystalline materials over conventional inorganic materials is the large bending angle and the small force required for the twinning deformation. In addition, it should be possible to achieve other functions such as photoluminescence along with ferroelasticity.

Recently, several organoferroelastic materials have been systematically developed by Takamizawa and co-workers, demonstrating organoferroelasticity under twinning and the spontaneous build-up of strain.[5–9] A common feature of these molecules is that they exhibit a relatively simple molecular structure,[5–12] and although mechanical twinning deformation of metallocenes[13] has been reported,[14] these do not exhibit organometallic ferroelastic behavior.

To generate ferroelastic molecular crystals which show photoluminescent properties, I have focused on gold complexes. Among various organometallic compounds, gold complexes have many attractive features, such as a relatively uncommon linear coordination geometry, high chemical stability in air, a high tendency to form polymorphs in the solid phase, and prominent solid-state phosphorescence properties.[14–17] It is also well known that gold complexes exhibit various responses to mechanical stresses, which parallel the color changes of photoluminescence, i.e., mechanochromic luminescence.[18–25] Ito group has intensively investigated crystalline materials of gold complexes that include isocyanide, phosphine, and *N*-heterocyclic (NHC) ligands, which often exhibit good crystallinity, photoluminescence and other novel stimulus-response properties. [19,21–27] Recently, I have shifted the focus to NHC gold complexes [28–31] in order to design structurally simple molecular scaffolds commonly found in previously reported ferroelastic compounds.[5–12] In order to achieve

ferroelasticity in organometallic gold complexes, I prepared various structurally simple NHC gold complexes (**1i**–**4i**) and investigated their mechanical properties. I found that NHC gold complexes **1i** and **3i** exhibit ferroelastic properties and spontaneously built-up strain, i.e., **1i** and **3i** constitute the first examples of organometallic ferroelastic luminescent crystals.

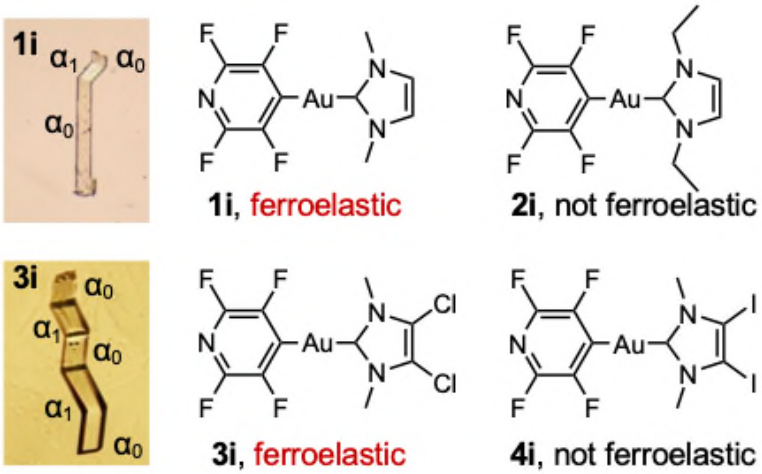

Figure 1. Chemical structures of **1i**–**4i** and photographs of bent crystals of **1i** and **3i**.

Herein, I report the first examples of luminscent ferroelasticity of organometallic NHC gold(I) complexes. Among the structurally similar NHC gold complexes **1i**–**4i**, crystals of **1i** and **3i** show ferroelastic behavior when stress is applied to specific crystal planes, while the crystals of **2i** and **4i** do not. The origin of the presence/absence of ferroelasticity of **1i**-**4i** will be discussed based on single crystal X-ray diffraction (XRD) measurements. Complexes **1i** and **3i** are the first ferroelastic crystal that also show persisting photoluminescence when the crystals are bent.

2.2. Results and Discussion

The mechanical properties of the crystals of these NHC complexes were investigated. In the Supporting Information, the synthesis of **1i**–**4i** are described in detail.[32] Single crystals of **1i**–**4i** were recrystallized from CH_2Cl_2/MeOH. When stress was applied to single crystals **1i** and **3i**, both crystals showed mechanical bending (Figure 2A). The shape of the bend is maintained after the stress is released, which confirms plastic deformation. Repeated experiments confirmed that the bending angle of the crystals of **1i** is reproducibly 45° (Figures 2A and S1). Scanning electron microscopy (SEM) measurements on bent crystals of **1i** confirmed a continuous clear surface at the boundaries between the bent and unbent moieties (Figures 2A and S2). The SEM images even showed a 45° bending for the local domain (~5 μm) of the bent crystal edge of **1i** that appeared upon shear stress (Figure 2A), which suggests a high tendency for bending at this angle. For crystals of **3i**, similar properties were observed with respect to crystal bending and twinning (Figures 2C and S1). The bending angle of **3i** is reproducibly ~33°, which was confirmed by optical microscopy and SEM (Figure 2C). On the other hand, crystals of **2i** and **4i** are brittle, i.e., they are not susceptible to bending and easily collapse upon loading with mechanical stress (Figure 2B and D and Figure S4).

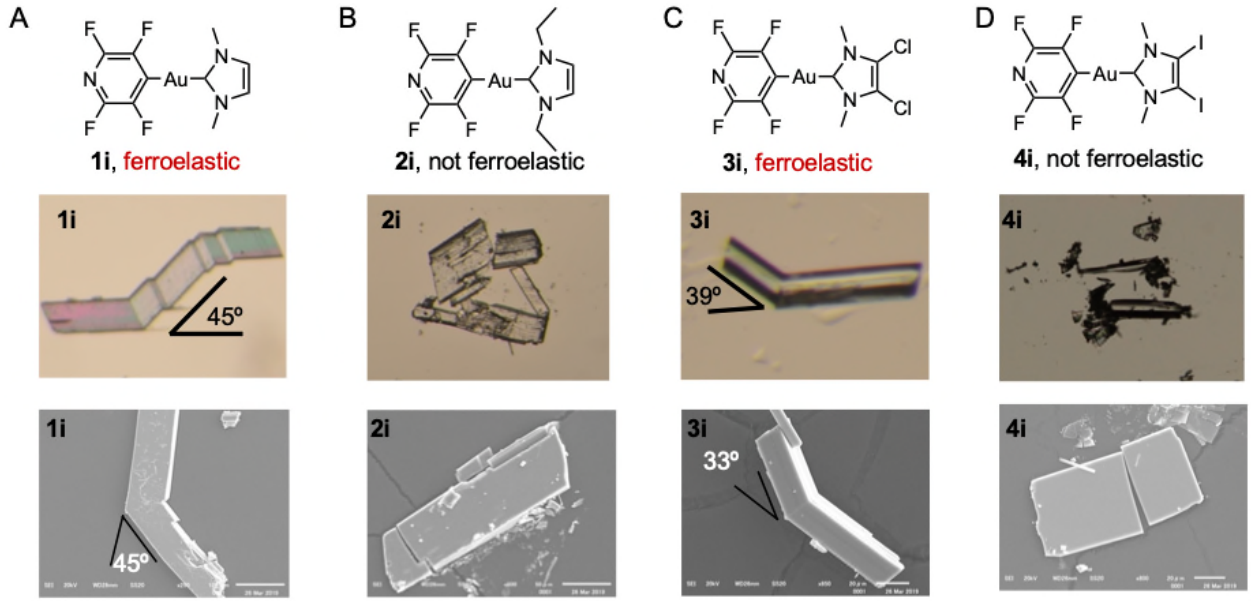

Figure 2. Chemical structures of **1i**–**4i**. And photographs and SEM of mechanical deformed crystals of **1i**–**4i**.

Single-crystal XRD analyses of bent crystals of **1i** indicate that the deformation is due to mechanical twinning.[33] Complex **1i** crystallizes in the triclinic *P*-1 space group with only one independent crystalline molecule in the unit cell (Figure S5 and Table S1).[34] The two aromatic rings of **1i** include a dihedral angle (θ) of 4.7(3)°. This flat conformation of **1i** allows a head-to-tail stacking arrangement along the *a* axis with a π-stacking distance of 3.415 Å (Figure S6). XRD analyses of **1i**

with face indexing indicated that the twinning deformation occurs upon bending via formation of daughter phase α_1 from mother phase α_0 when applying shear stress along the [0-10] plane (Figure 3). The twinning interface was specified at $(100)_{\alpha0}$//$(\text{-}100)_{\alpha1}$, i.e., perpendicular to the stacked column. This indicates that the daughter phase α_1 lattice is formed by rotating 180° along the [100] direction (rotation axis is show in grey arrows in Figure 3). Based on these crystallographic results, a bending angle between α_0 and α_1 of 42.9° can be predicted, which agrees well with the bending angle (45°) observed by optical microscopy and SEM (Figure 2A). In order to achieve the aforementioned continuous boundaries between the α_0 phases and α_1 phase when bending the crystals, such molecular rotations (~19°) can be expected to occur under a concomitant displacement (movement) of the constituent molecules along the bending direction. In the present case, it is assumed that slippage between π-shaped stacked columns is also feasible while retaining the overall column structure.

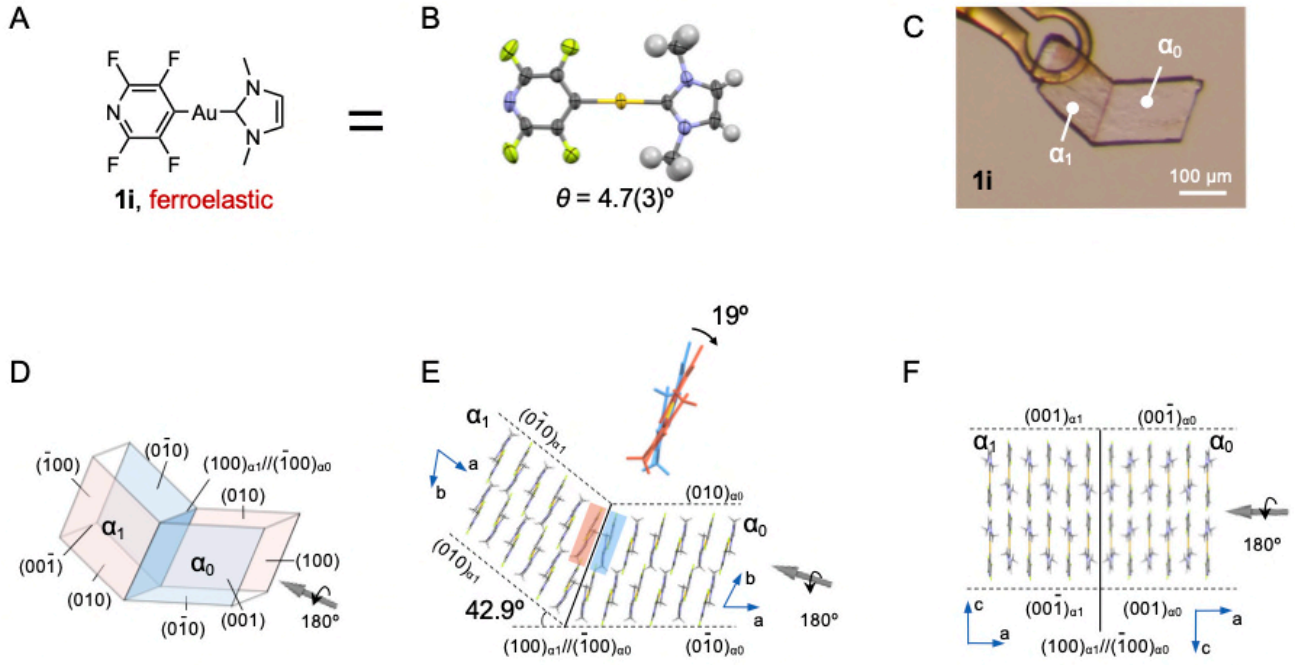

Figure 3. Chemical structures of **1i**. And Photographic image of the twinning deformation of **1i** as well as its crystal face indices and packing arrangements. E) Gray arrows indicate the rotation axis.

The single-crystal structure analyses of the mechanically bent crystals of **3i** also indicate that a twinning deformation occurs upon loading mechanical shear stress similar to **1i**. The overall crystal structure of **3i** at 20 °C[34,35] is similar in part to that of **1i**: the space group is $P2_1/n$; the molecules adopt a flat molecular conformation (θ = 2.2(5)°) and form π-stacked columns in a head-to-tail arrangement (Figures 4 and S7 as well as Table S1). Mechanical twinning was clearly confirmed by face-index experiments upon applying shear stress along the [001] plane. The interface of **3i** between the α_0 and α_1 domains is $(10\text{-}1)_{\alpha0}$//$(10\text{-}1)_{\alpha1}$ and found that rotational axis is oriented along [001] direction (grey

arrows and dot in Figure 4). The bending angle of the crystal at the interface calculated from the crystallographic data is 40.4° (Figure 4), which is roughly consistent with the results obtained from optical microscopy and SEM (Figure 2C).

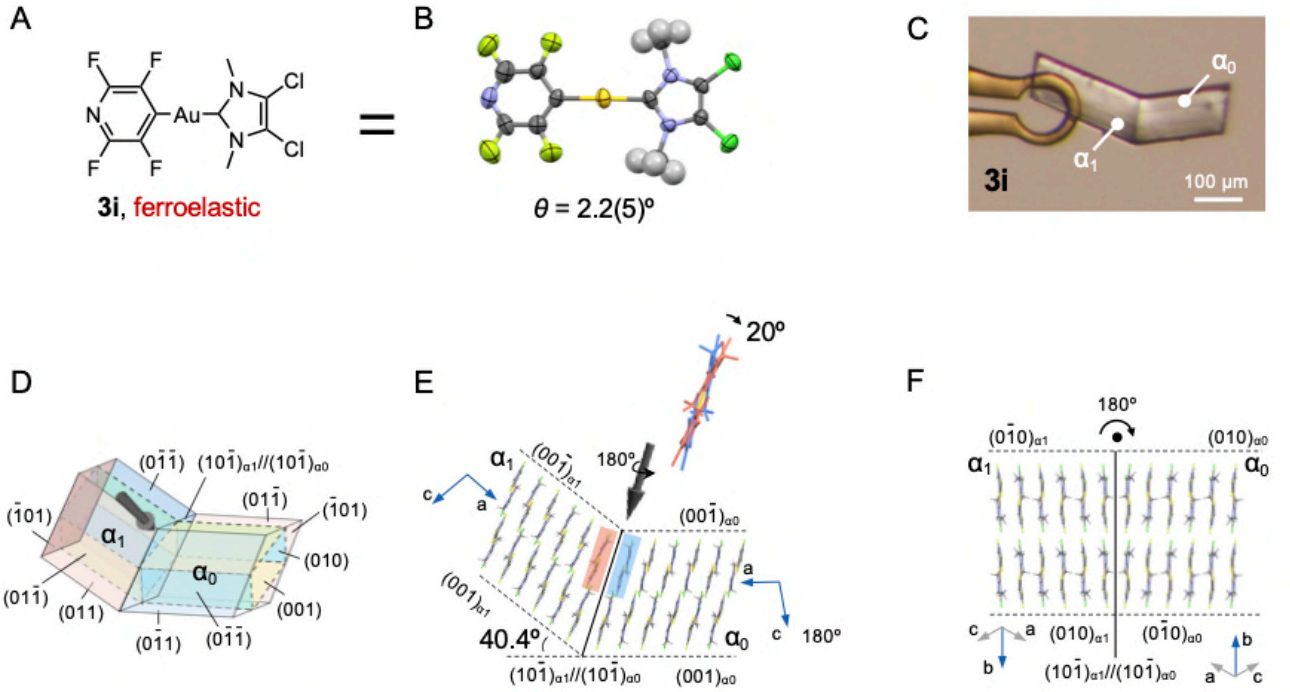

Figure 4. Chemical structures of **3i**. And Photographic image of the twinning deformation of **3i** as well as its crystal face indices and packing arrangements. E) Gray arrows indicate the rotation axis.

Subsequently, the stress-strain relationship in crystals of **1i** and **3i** were investigated. For that purpose, experimental setups from previous studies were used:[4–9] one end of the crystal was immobilized with epoxy glue, and the shear force was loaded by a jig to the specific crystal face of the other end of the crystal. Crystals of **1i** start to detect the stress almost immediately when the jig reaches the crystal surface (Figure 5A, i). For **1i**, the α_1 domain started to grow at an applied stress of 0.61 MPa (Figure 5A, ii). Similar to previously reported ferroelastic crystals, the shear stress is relatively constant upon further applying the force during the expansion of the daughter phase α_1. After unloading the stress, spontaneous build-up strain was observed (Figure 5A,C). Upon subsequent loading of force from the opposite direction, the reverse deformation was induced to recover the original phase α_0 (Figure 5A, iii, iv). Throughout this process, a critical stress of 0.49 MPa was estimated. Such hysteresis behavior and the build-up of spontaneous strain clearly indicate typical ferroelastic behavior for **1i**. As expected, similar ferroelastic hysteresis loops for the formation of daughter phase α_1 were observed for single crystals of **3i** with a forward and reverse critical stress of 0.21 and 0.13 MPa, respectively (Figure 5B,D.[36] These critical stress values are relatively weak compared to those of other

previously reported ferroelastic crystals.

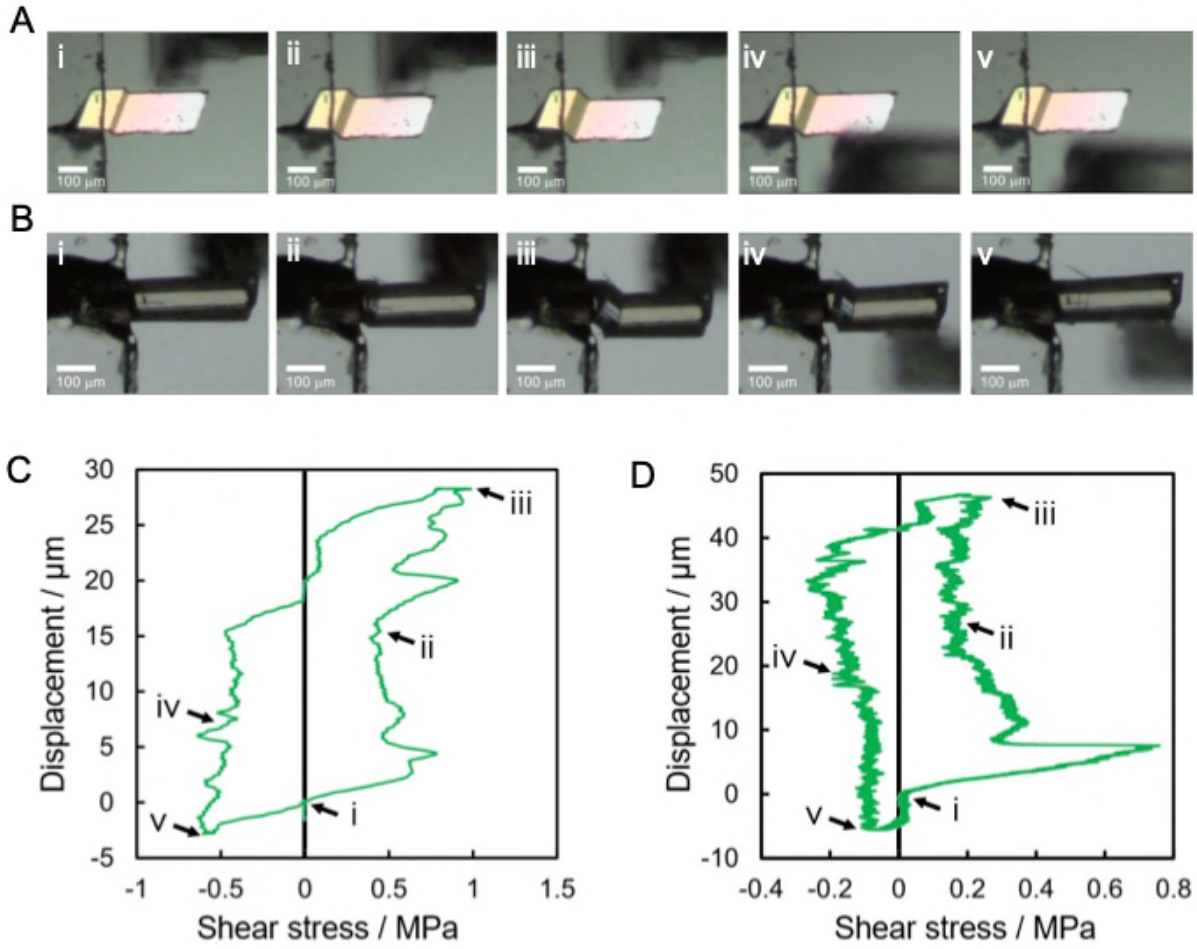

Figure 5. Photographic images and stress-strain hysteresis loops for the ferroelastic bending of crystals of A, C) **1i** and B,D) **3i**. Displacement rates: 10 μm/s (**1i**) and 1 μm/s (**3i**).

In comparing the crystal structures of **1i**-**4i**, it was provided insight into the structural factors that determine the ferroelasticity of **1i** and **3i**.The single-crystal structure analyses of non-ferroelastic **2i** and **4i** revealed that their overall structures are similar to those of **1i** and **3i**, which includes a flat molecular conformation, the formation of π-stacked columns, and weak column-to-column interactions (Figures S12 and S13 as well as Table S2). Nevertheless, only **1i** and **3i** show ferroelasticity (vide supra). To allow major molecular rotations (1: ~19°; 3: ~20°) in the dense solid environment upon ferroelastic bending, sufficient space is required between the molecules. For **2i**, the ethyl groups should prevent the molecular rotation due to the steric repulsion between the ethyl groups within the neighboring molecular columns (highlighted in blue in Figures 6B). Such steric repulsion between columns is not observed in **1i**, **3i**, or **4i** (Figures 6A and S14). Molecular packing that is resistant to mechanical stress would be another factor required to prevent a simple collapse of the crystals upon bending. This feature would be facilitated by effective overlapping of molecular stacks

via a combination of dipole-dipole and π-π stacking interactions. However, molecules of **4i** in the columnar arrangement show a rotational displacement by ~30° (Figure 6D), which should decrease the structural resistance of the crystals of **4i** toward mechanical force compared to those of the other compounds. Different from molecular columns of **4i**, those of **1i**, **2i**, and **3i** do not show significant rotational displacements (< 5°; Figures 6D and S15). These insights into the structure-property relationship derived from a series of NHC gold complexes may be helpful to develop principles for the design of advanced ferroelastic organic crystal materials.

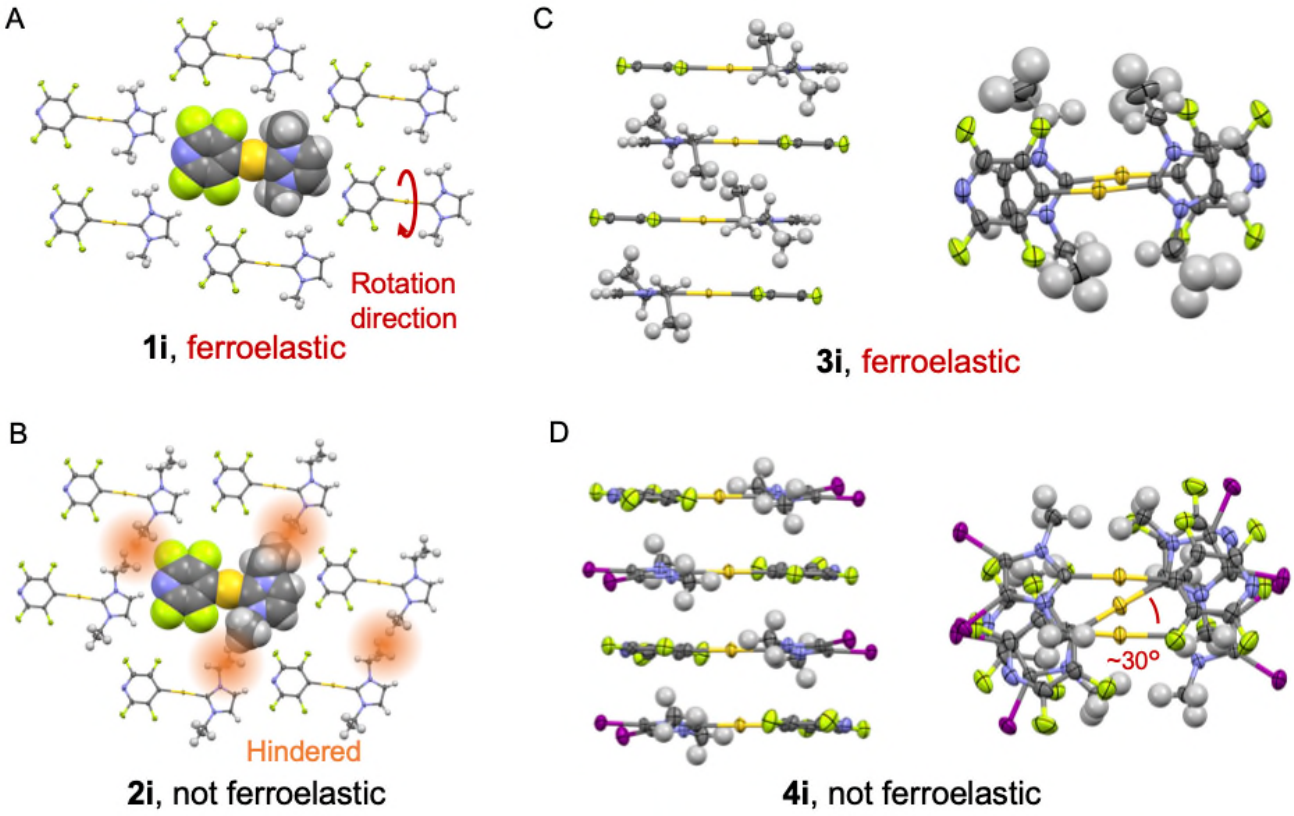

Figure 6. Single-crystal structures of A) **1i**, B) **2i**, C) **3i**, and D) **4i**.

Moreover, crystals of **1i** and **3i** exhibit blue photoluminescence. Under exposure to UV light, crystals of **1i** show a featureless emission spectrum with a maximum at 431 nm, a large absolute emission quantum yield (Φ_{em} = 0.65), and phosphorescence character (average emission lifetime, τ_{av} = 0.43 μs; Figures 7 and S16 as well as Table S3). A similar emission spectrum was observed for crystals of **3i** ($\lambda_{em,max}$ = 452 nm; Φ_{em} = 0.42; τ_{av} = 0.31 μs) (Figure S17).[37] I next investigated the effect of bending on the photoluminescence properties. The bent moiety (α_1) of **1i** shows an emission spectrum similar to that of the unbent (α_0) moiety (Figure 7). Similarly, the bent moiety of crystals of **3i** provided an unchanged emission spectrum (Figure S17). These results confirm that the

photoluminescence properties of the crystals of **1i** and **3i** are stable toward mechanical deformation. This seems reasonable given that the impact of the mechanical force does not induce deterioration of the packing arrangements and the crystal structures of the twinned α_0 and α_1 phases, which differ only with respect to their relative orientation.[38]

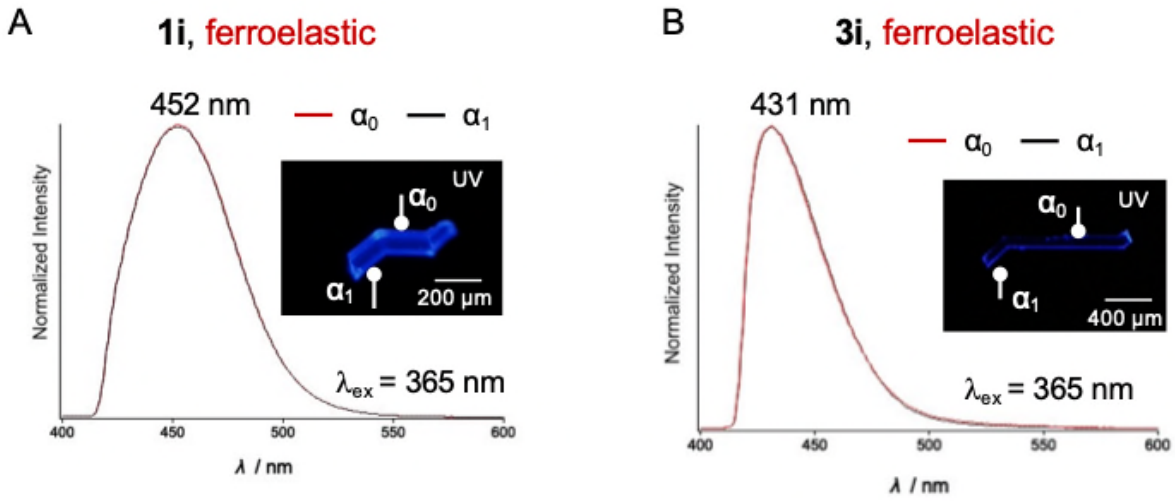

Figure 7. Emission spectra of the unbent (α0) and bent moiety (α1) as well as photographic images of a crystal of **1i** (A) and **3i** (**3i**).

The effect of photoexcitation on the mechanical properties of crystals of **1i** and **3i** were also investigated. For that purpose, the stress-strain hysteresis loops of **1i** and **3i** were re-examined under illumination with UV light. The results indicate that excitation from UV light does not significantly affect the ferroelastic behavior: the hysteresis loops under exposure to UV light are virtually identical to those obtained under exposure to visible light (Figure S20 and S21).

2.3. Conclusions

In summary, the first examples of ferroelasticity in organometallic NHC complexes of Au(I) under spontaneous build-up of intrinsic strain was reported. Upon loading the stress, crystals of **1i** and **3i** show reproducible bending by 45° and 35°, respectively. X-ray diffraction analyses indicate that mechanical twinning occurs, i.e., that the molecular orientations are changed in the bent moieties. Stress-strain curves of crystals of **1i** and **3i** indicate typical ferroelastic properties, including the build-up of spontaneous strain and hysteresis loops. A comparison of the crystal structures of **1i**–**4i** suggested that an elaborate balance between the effective formation of π-stacked columns and appropriate intermolecular interactions between the columns are required to generate the ferroelastic behavior. Further exploration of NHC-ligated Au(I) complexes for the development of related functional molecular crystals with desirable mechanical properties are currently in progress.

2.4. Experimental details

2.4.1. General

All commercially available reagents and solvents are of reagent grade and were used without further purification unless otherwise noted. Solvents for the synthesis were purchased from commercial suppliers, degassed by three freeze-pump-thaw cycles and further dried over molecular sieves (4 Å). NMR spectra were recorded on a JEOL JNM-ECX400P or JNM-ECS400 spectrometer (1H: 400 MHz; 13C: 99.5 MHz) using tetramethylsilane and CDCl3 as internal standards, respectively. Emission spectra were measured by using an Olympus fluorescence microscope BX51 equipped with Hamamatsu photonics multichannel analyzer PM-12. The emission quantum yields of the solid samples were recorded on a Hamamatsu Quantaurus-QY spectrometer with an integrating sphere. Emission lifetime measurements were recorded on a Hamamatsu Quantaurus-Tau spectrometer. Elemental analyses and high-resolution mass spectra were recorded at Global Facility Center, Creative Research Institution, Hokkaido University. Photographs were obtained using Olympus BX51 or SZX7 microscopes with Olympus DP72, or Nikon D5100 digital cameras. Scanning electron microscopic images were acquired by using JEOL JSM-6510LV. Stress-strain tests were carried out on a universal testing machine (Tensilon RTG-1210, A&D Co. Ltd.).

X-ray diffraction analyses: Single crystal X-ray structural analyses were carried out on a Rigaku XtaLAB PRO MM007 diffractometer using graphite monochromated Mo-K radiation. The structure was solved by direct methods and expanded using Fourier techniques. Non-hydrogen atoms were refined anisotropically. Hydrogen atoms were refined using the riding model. All calculations were performed using the Olex2 crystallographic software package except for refinement, which was performed using SHELXL-2018.[39] Simulated powder patterns were generated with Mercury 4.1[40]from the structures determined by the single-crystal diffraction analyses.

2.4.2. Synthesis of 1i, 2i, 3i and 4i

Scheme for the synthesis of **1i**.

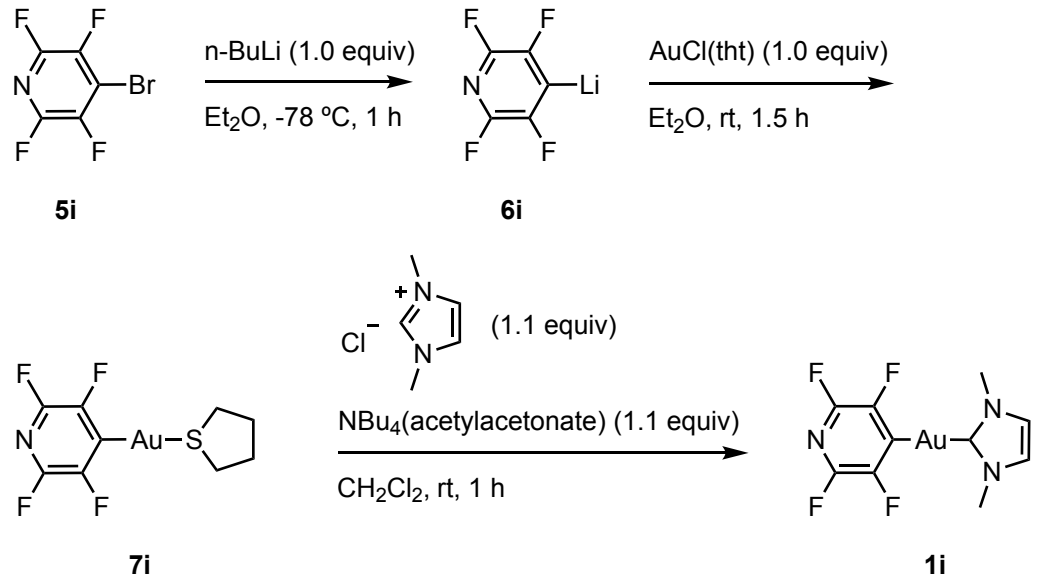

*Synthesis of tetrafluoropyrid-4-yl(1,3-dimethylimidazolin-2-ylidene)gold complex **1i**.*

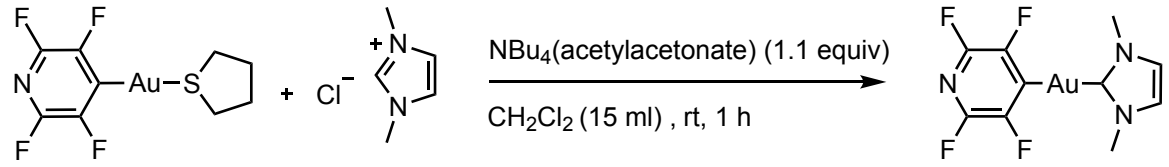

Compound **1i** was prepared by the modification of the literature method.[41] An oven-dried two-neck flask was connected to a vacuum/nitrogen manifold through a rubber tube. It was evacuated and then backfilled with nitrogen. This cycle was repeated three times. In this flask, a solution of 7[42] (226 mg, 0.5 mmol) and **8i** (73 mg, 0.55 mmol) in CH2Cl2 (15 ml) were prepared and stirred until a colorless solution formed (5 min). Then, NBu4(acetylacetonate) (188 mg, 0.55 mmol) was added and stirred for 1 h at room temperature. The reaction mixture was directly filtered through a plug of silica and the colorless filtrate evaporated to minimum volume. Hexane was added to the residue to form a white solid which was collected through the filtration and vacuum dried to give the analytically pure product **1i** (65 mg, 0.15 mmol, 29%). ^{1}H NMR (392 MHz, $CDCl_3$, δ): 3.92 (s, 6H), 6.96 (s, 2H). MS-ESI (*m*/*z*): $[M+H]^+$ calcd for $C_{10}H_9N_3AuF_4$, 444.03981; found, 444.03887. This compound exhibits poor solubility in common organic solvents; therefore, ^{13}C NMR spectroscopy can not be measured.

*Synthesis of tetrafluoropyrid-4-yl(1,3-diethylimidazolin-2-ylidene)gold complex **2i**.*

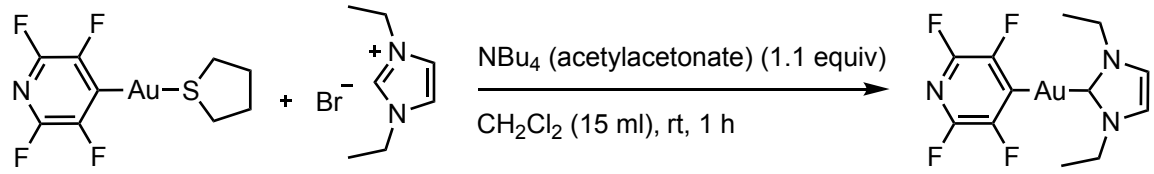

7i (0.5 mmol) **9i** (1.1 equiv) **2i**

Compound **2i** was prepared from **7i** (226 mg, 0.5 mmol) and **9** (112 mg, 0.55 mmol)[43] according to the procedure similar to that described for preparation of **2i**. Yield: 17% (40 mg, 0.08 mmol). ^{1}H NMR (392 MHz, $CDCl_3$, δ): 1.55 (t, J = 7.4 Hz, 6H), 4.29 (q, J = 7.4 Hz, 4H), 6.98 (s, 2H). MS-ESI (*m*/*z*): $[M+H]^+$ calcd for $C_{12}H_{13}N_3AuF_4$, 472.07111; found, 472.06880. This compound exhibits poor solubility in common organic solvents; therefore, ^{13}C NMR spectroscopy can not be measured.

*Synthesis of tetrafluoropyrid-4-yl(4,5-dichloro-1,3-dimethylimidazolin-2-ylidene)gold complex **3i**.*

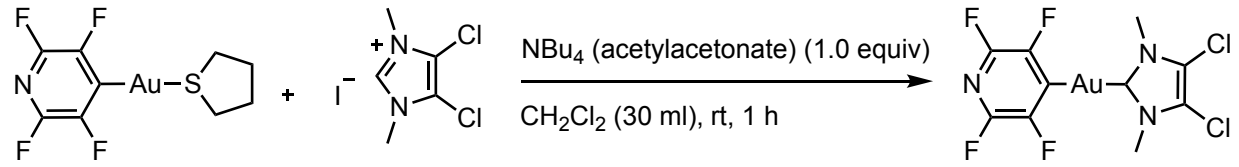

7i (0.5 mmol) **10i** (1.0 equiv) **3i**

Compound **3i** was prepared from **7i** (226 mg, 0.5 mmol) and **10** (147 mg, 0.5 mmol)[44] according to the procedure similar to that described for preparation of **3i**. Yield: 36% (91 mg, 0.18 mmol). ^{1}H NMR (396 MHz, $CDCl_3$, δ): 3.91 (s, 6H). MS-ESI (*m*/*z*): $[M+H]^+$ calcd for $C_{10}H_7N_3AuF_4Cl_2$, 511.96187; found, 511.95995. This compound exhibits poor solubility in common organic solvents; therefore, ^{13}C NMR spectroscopy can not be measured.

*Synthesis of tetrafluoropyrid-4-yl(4,5-diiodo-1,3-dimethylimidazolin-2-ylidene)gold complex **4i**.*

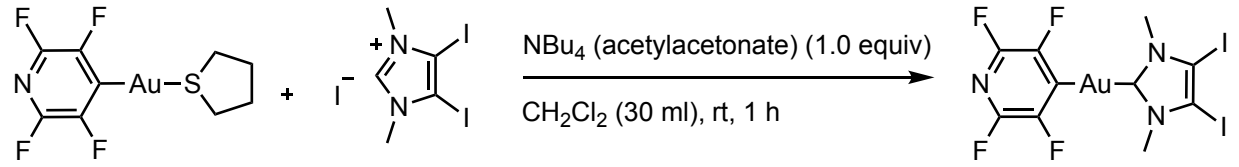

7i (0.5 mmol) **11i** (1.0 equiv) **4i**

Compound **4i** was prepared from **7i** (226 mg, 0.5 mmol) and **11i** (239 mg, 0.5 mmol)[45] according to the procedure similar to that described for preparation of **4i**. Yield: 9% (32 mg, 0.05 mmol). ^{1}H NMR (400 MHz, $CDCl_3$, δ): 4.04 (s, 6H). MS-ESI (*m*/*z*): $[M+H]^+$ calcd for $C_{10}H_7N_3AuF_4I_2$, 695.83310; found, 695.83120. This compound exhibits poor solubility in common organic solvents; therefore, ^{13}C NMR spectroscopy can not be measured.

2.4.3. Preparation and images of the single crystals of 1i, 2i, 3i and 4i

*Preparation of the single crystal of **1i***:
The single crystal of **1i** is obtained by liquid-liquid diffusion. Typically, **1i** (5 mg) is dissolved in 1.0 mL of CH_2Cl_2 in a vial and hexane (3.0 mL) was carefully layered. After standing for several days at 276 K, the colorless single crystals of **1i** are formed.

*Preparation of the single crystal of **2i***:
The single crystal of **2i** was prepared from **2i** (5 mg), CH_2Cl_2 (0.5 mL) and hexane (3.0 mL) according to the procedure similar to that described for preparation of crystal of **1i**.

*Preparation of the single crystal of **3i***:
The single crystal of **3i** was prepared from **3i** (5 mg), CH_2Cl_2 (1.5 mL) and hexane (4.5 mL) according to the procedure similar to that described for preparation of crystal of **1i**.

*Preparation of the single crystal of **4i***:
The single crystal of **4i** was prepared from **4i** (1 mg), CH_2Cl_2 (1.5 mL) and hexane (4.5 mL) according to the procedure similar to that described for preparation of crystal of **1i**.

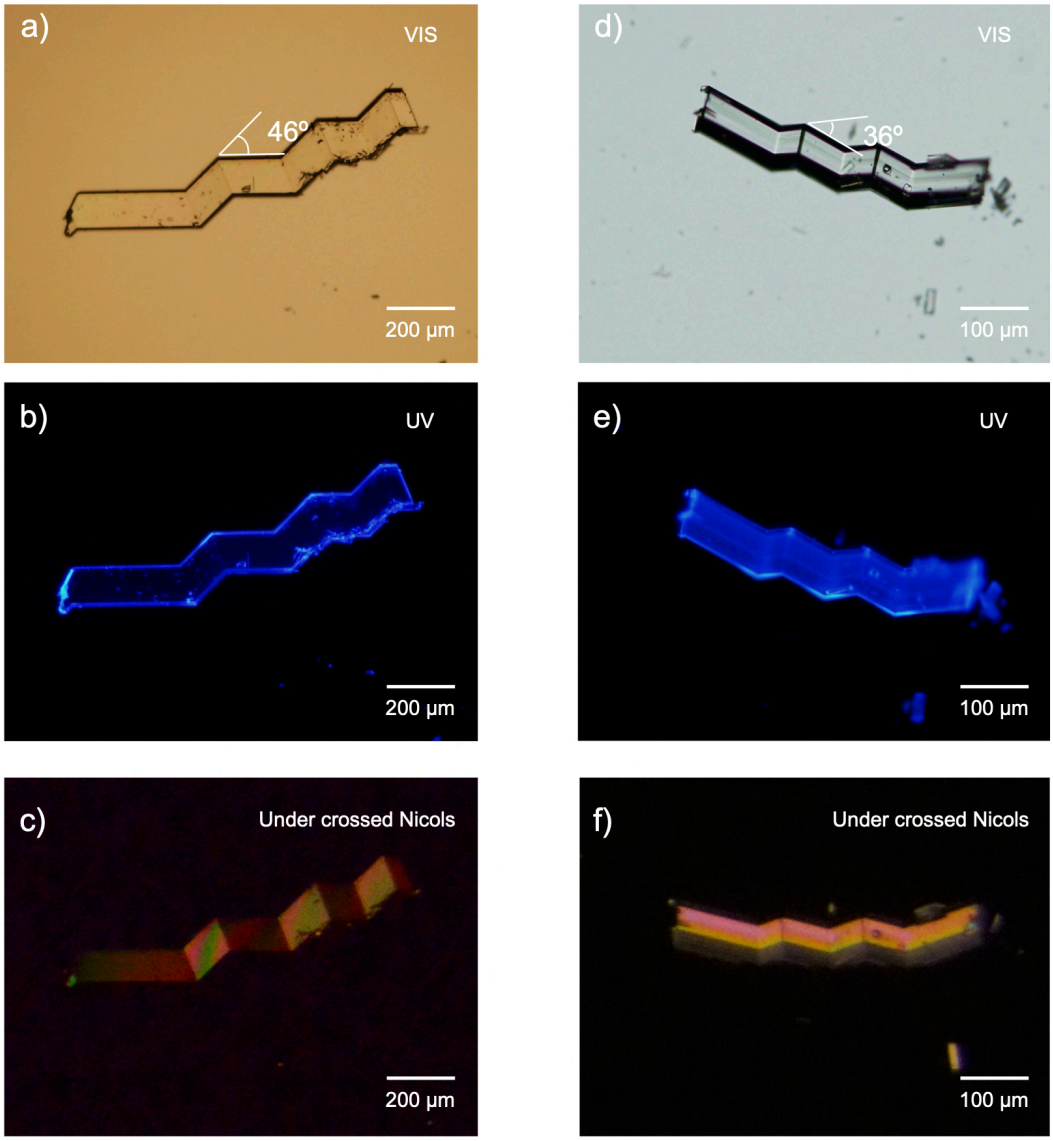

Figure S1. Photographs of mechanically bending crystals of **1i** observed under a) visible light, b) UV light, and c) crossed Nicols. Photographs of mechanically bending crystals of **3i** observed under a) visible light, b) UV light, and c) crossed Nicols.

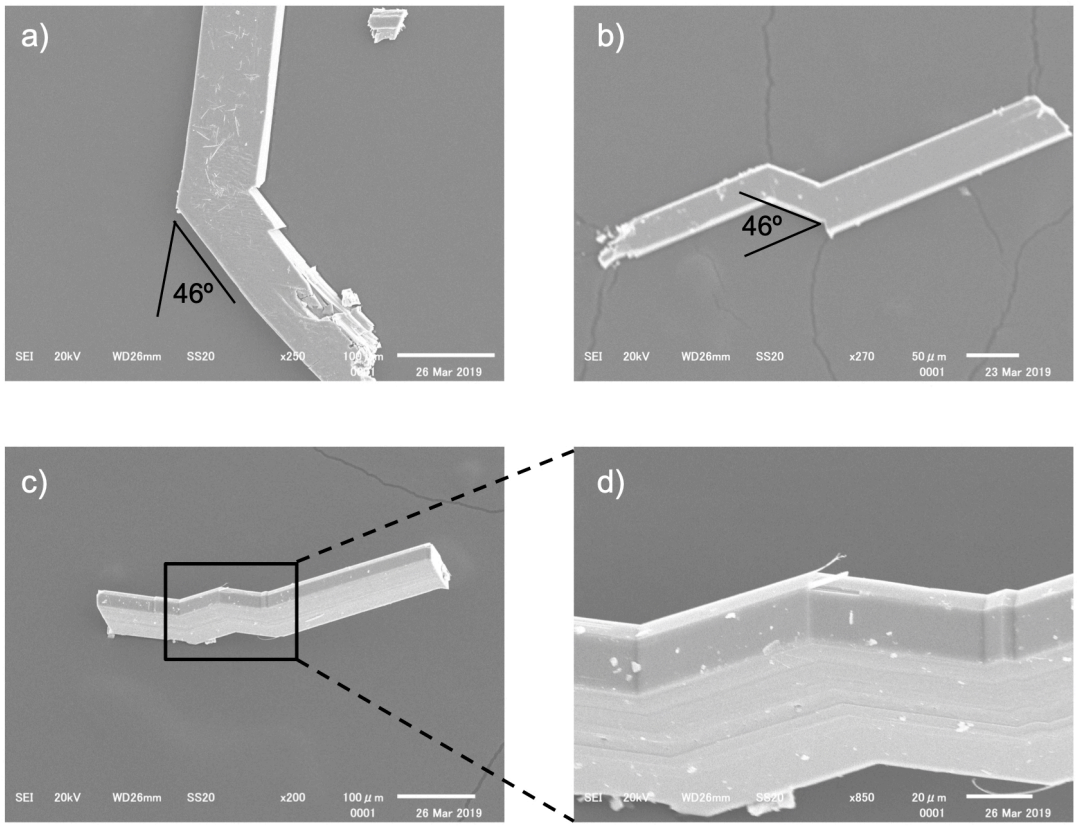

Figure S2. SEM images of the bending crystals of **1i**.

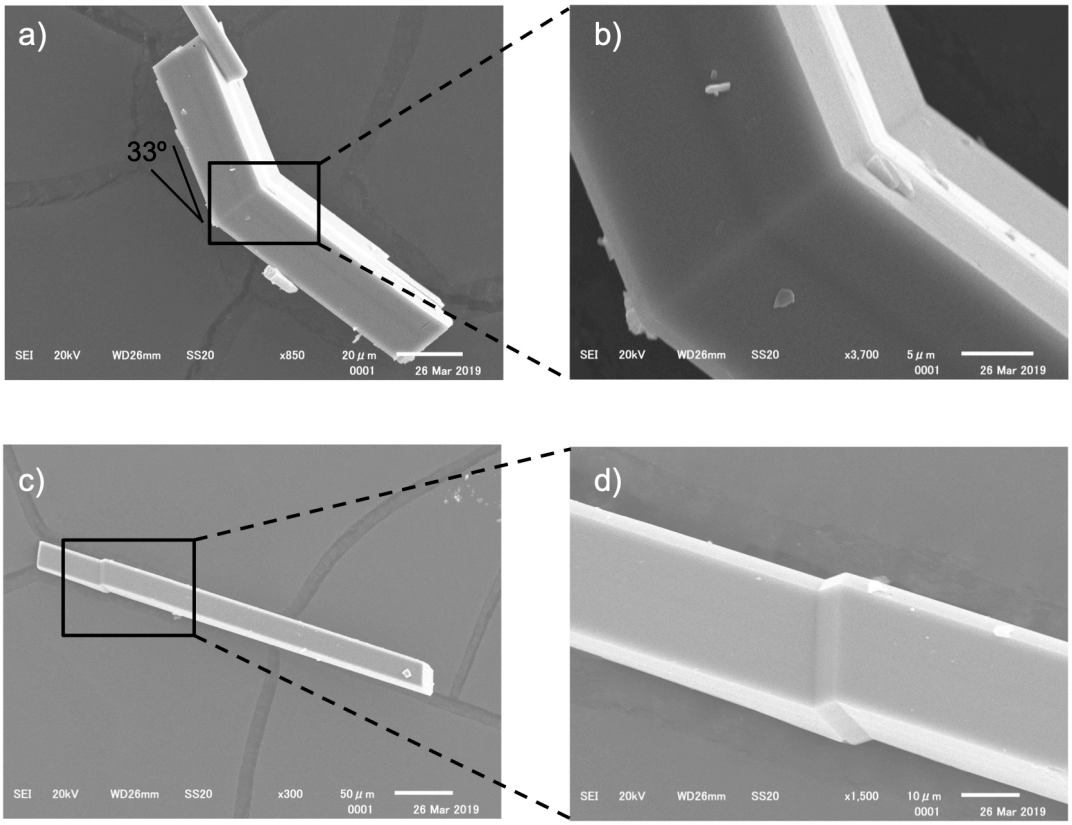

Figure S3. SEM images of the bending crystals of **3i**.

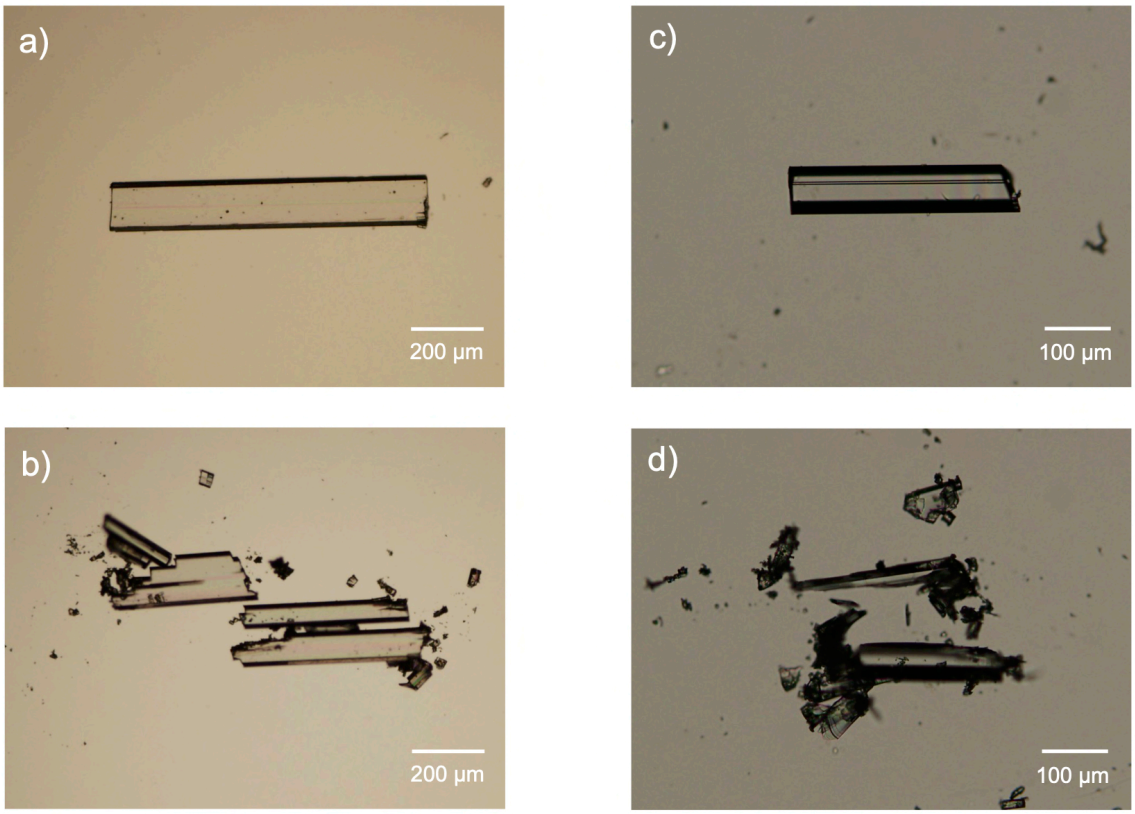

Figure S4. Photographs of the crystal of **2i** a) before and b) after loading the stress taken under ambient light. Photographs of the crystal of **4i** c) before and d) after loading the stress taken under ambient light.

2.4.4. Single-crystal XRD structure analyses of 1, 2, 3, and 4

Table S1. X-ray crystallographic data for **1** and **3**.

compound	**1-293 K**	**1-253 K**	**3-293 K**	**3-253 K**
CCDC Number				
Empirical Formula	$C_{10}H_8Au_1F_4N_3$	$C_{10}H_8Au_1F_4N_3$	$C_{10}H_6Au_1Cl_2F_4N_3$	$C_{10}H_6Au_1Cl_2F_4N_3$
Formula Weight	443.16	443.16	512.04	512.04
Crystal Size / mm	0.300×0.070×0.070	0.280×0.150×0.100	0.350×0.100×0.070	0.280×0.070×0.070
Crystal System	triclinic	triclinic	monoclinic	triclinic
a / Å	6.9126(4)	6.87740(10)	7.0323(3)	6.99930(10)
b / Å	8.1949(3)	8.1953(2)	11.7555(5)	11.7299(3)
c / Å	11.8939(3)	11.8868(3)	16.4056(8)	16.3918(4)
α / °	73.357(3)	73.452(2)	90	89.425(2)
β / °	84.135(4)	83.951(2)	93.533(4)	85.788(2)
γ / °	67.856(4)	66.516(2)	90	87.524(2)
V / Å^3	598.17(5)	593.40(2)	1353.64(11)	1340.86(5)
Space Group	P-1	P-1	$P2_1/n$	P-1
Z value	2	2	4	4
D_{calc} / g cm^{-3}	2.462	2.480	2.513	2.536
Temperature / K	293	253	293	253
$2\theta_{max}$ / °	58.802	58.656	58.792	58.744
μ / cm^{-1}	123.38 (Mo K$_\alpha$)	124.32 (Mo K$_\alpha$)	111.30 (Mo K$_\alpha$)	114.07 (Mo K$_\alpha$)
No. of Reflections	Total: 5494 Unique: N/A[a] (R_{int}: N/A[a])	Total: 10110 Unique: 2778 R_{int}: 0.0411	Total: 6373 Unique: N/A[a] (R_{int}: N/A[a])	Total: 28218 Unique: 6453 R_{int} = 0.0489
R_1[b]; wR_2[c]	0.0302; 0.0801	0.0360; 0.0884	0.0887; 0.2728	0.0352; 0.0869
GOF[d]	1.012	1.170	1.055	1.250
Max./Mini. peak I[d] / Å^3	0.78 e$^-$/−1.46 e$^-$	0.87 e$^-$/−3.86 e$^-$	2.14 e$^-$/−1.06 e$^-$	1.23 e$^-$/−1.67 e$^-$

[a]: Not available because of the twin analyses. [b]: For data with $I > 2.00\sigma(I)$. [c]: For all reflection data. [d]: Goodness of Fit.

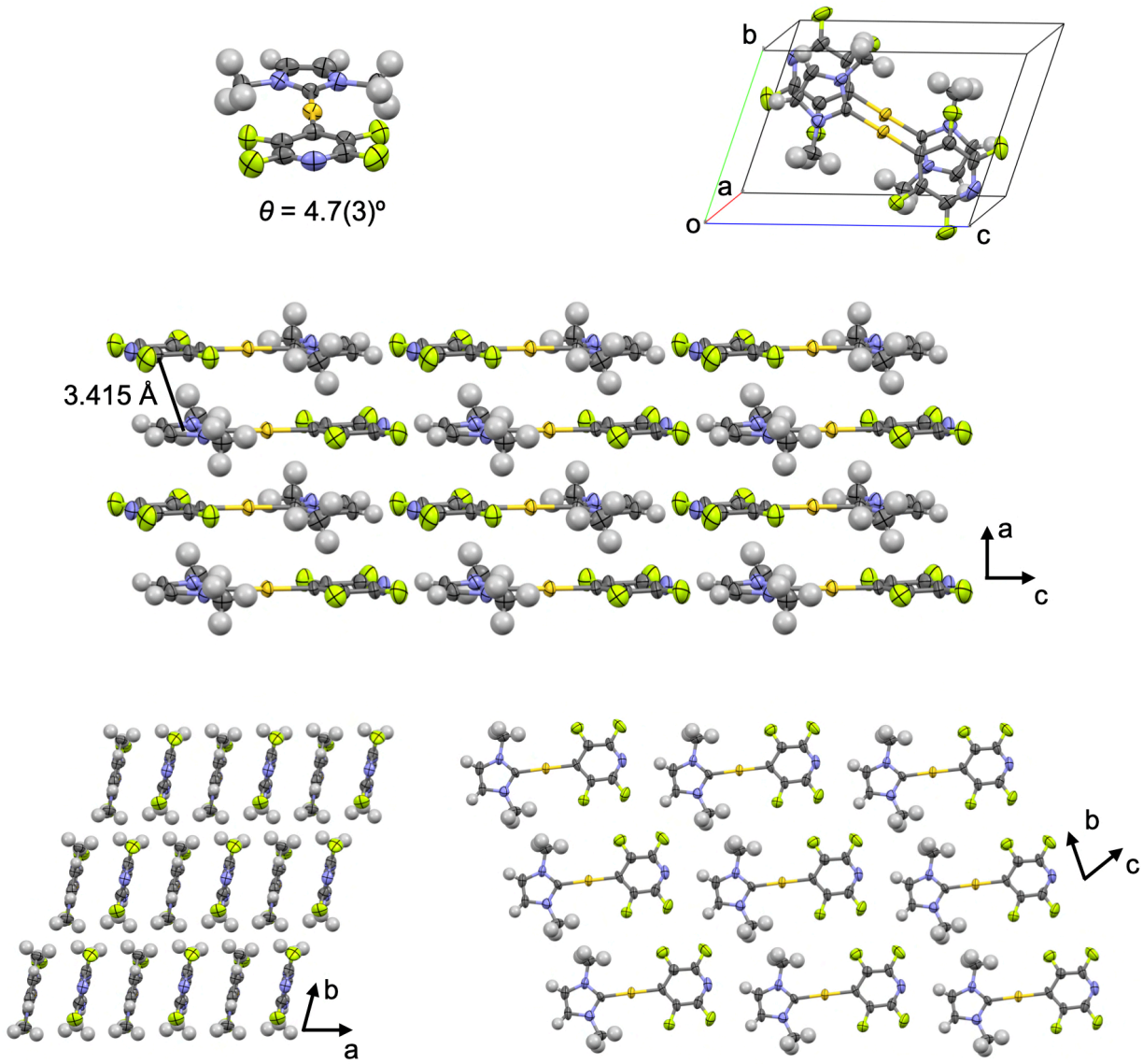

Figure S5. Single-crystal structure of **1i** at 20 ºC.

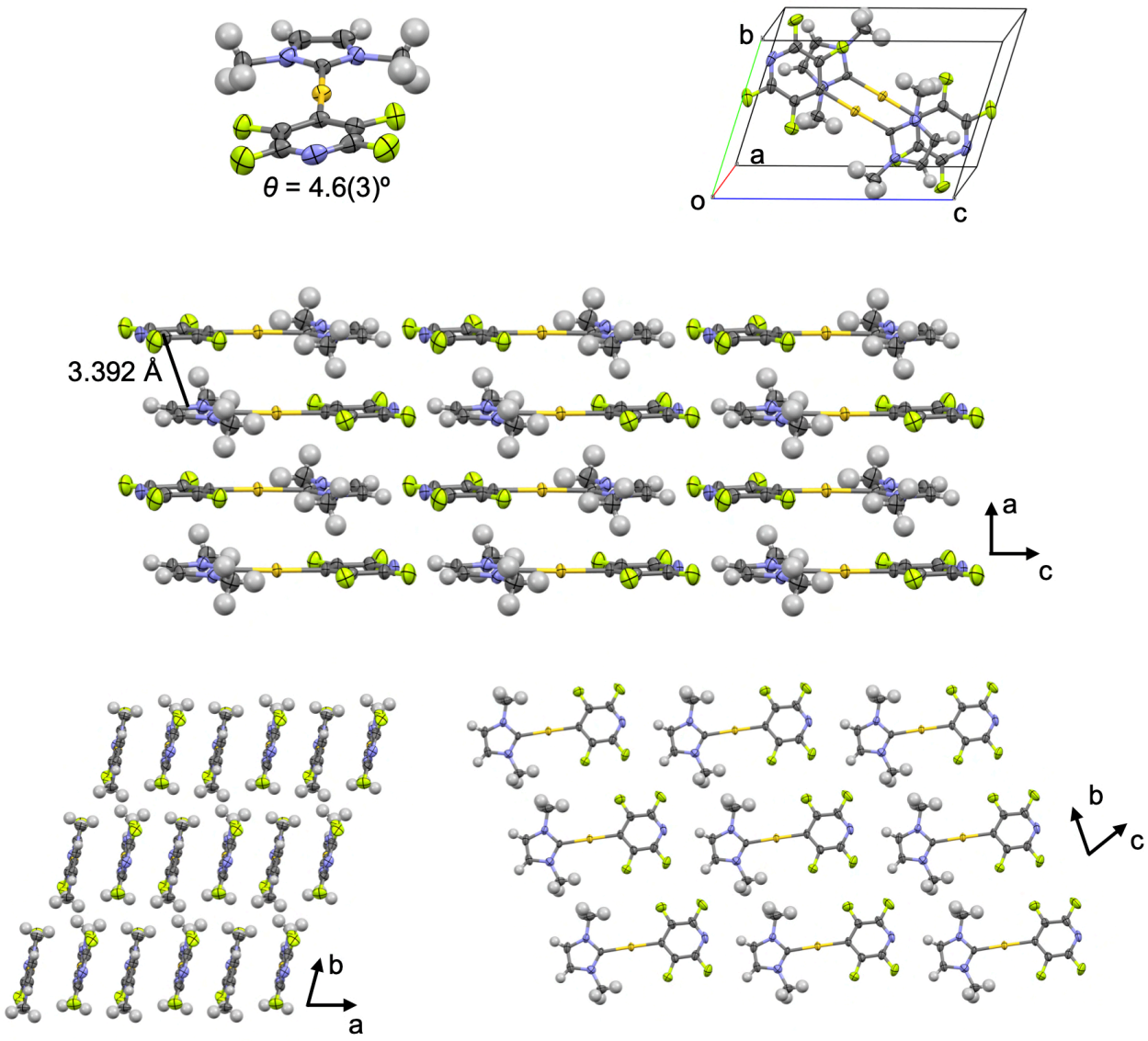

Figure S6. Single-crystal structure of **1i** at –20 ºC.

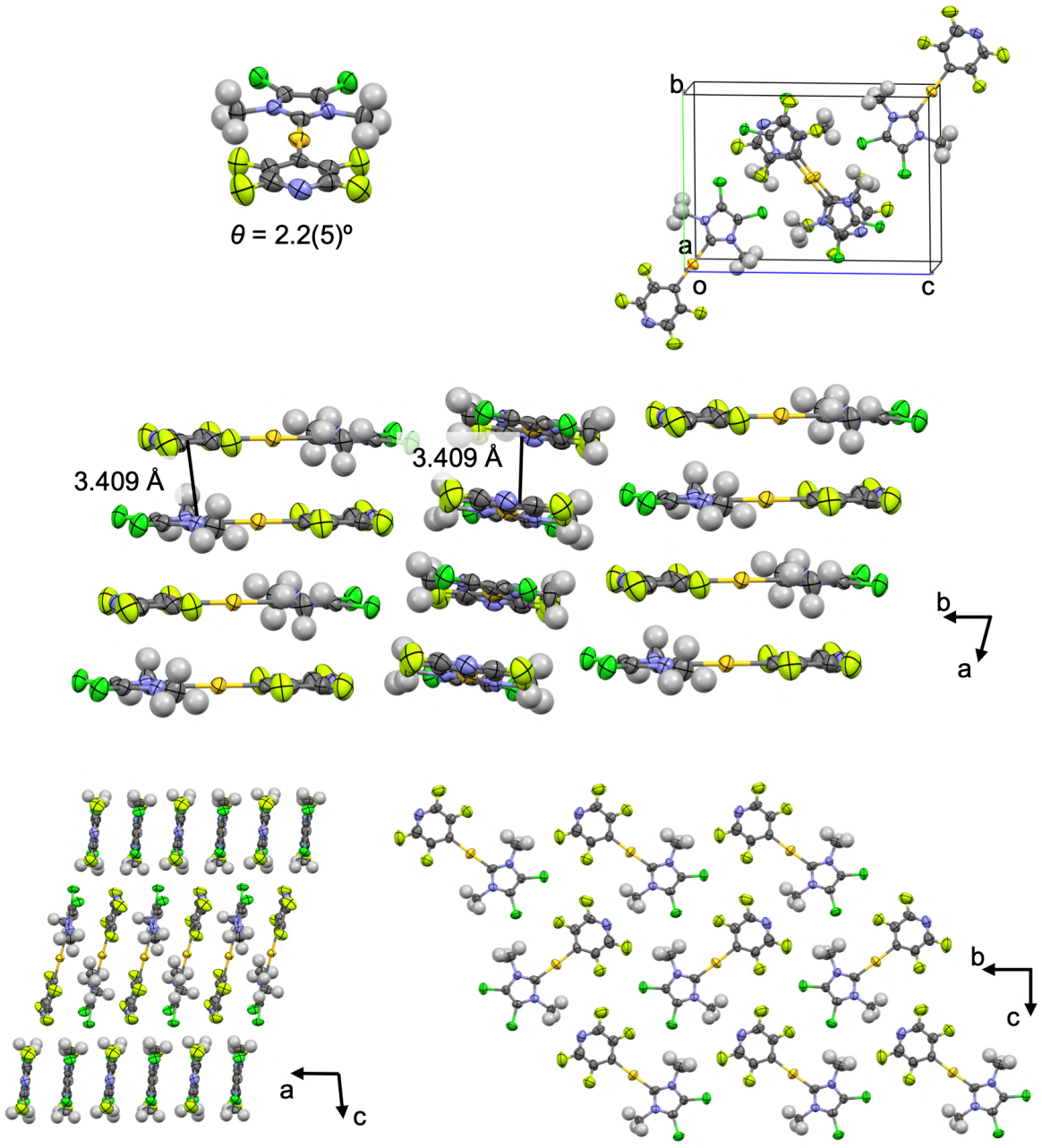

Figure S7. Single-crystal structure of **3i** at 20 ºC.

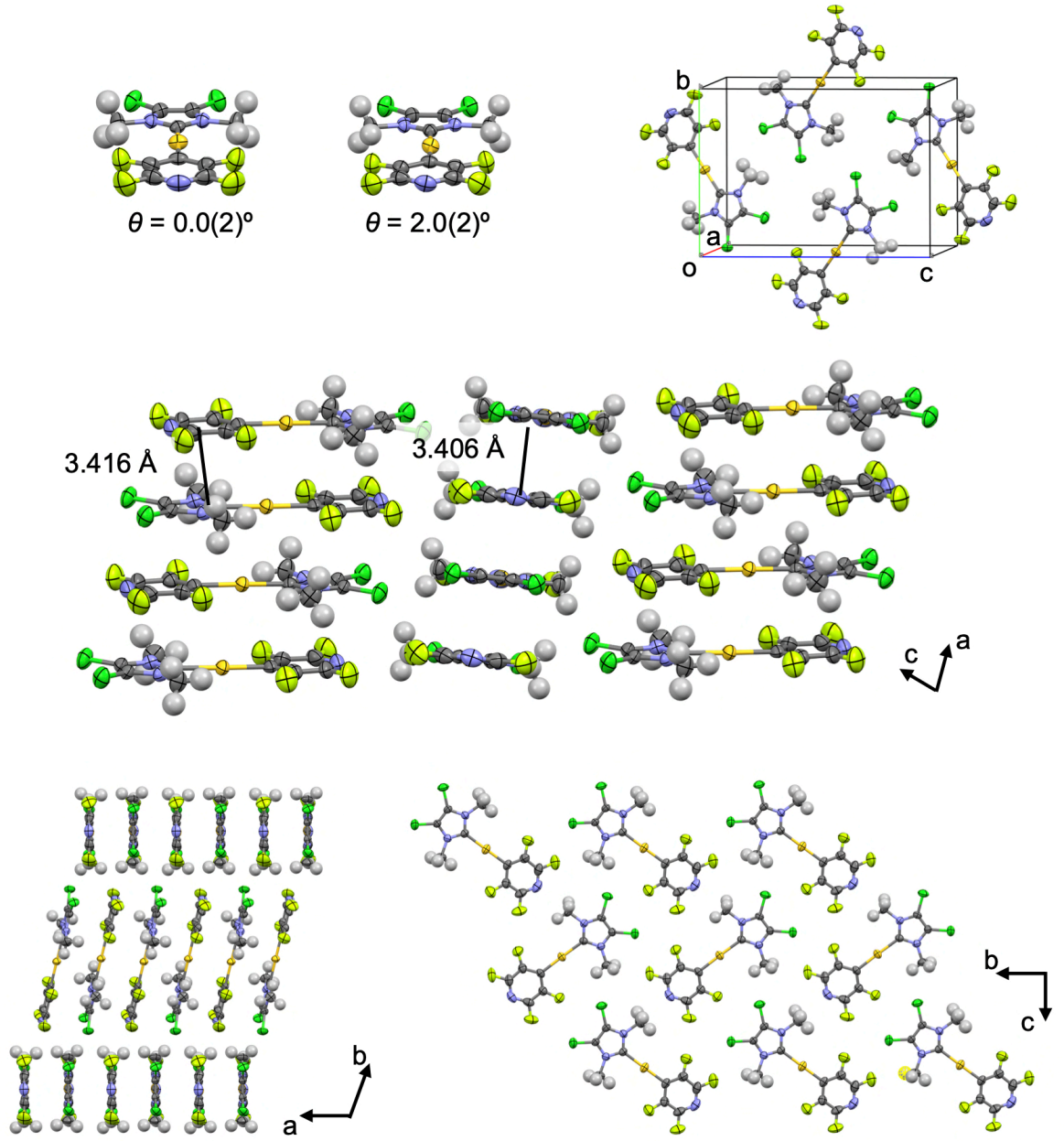

Figure S8. Single-crystal structure of **3i** at –20 ºC.

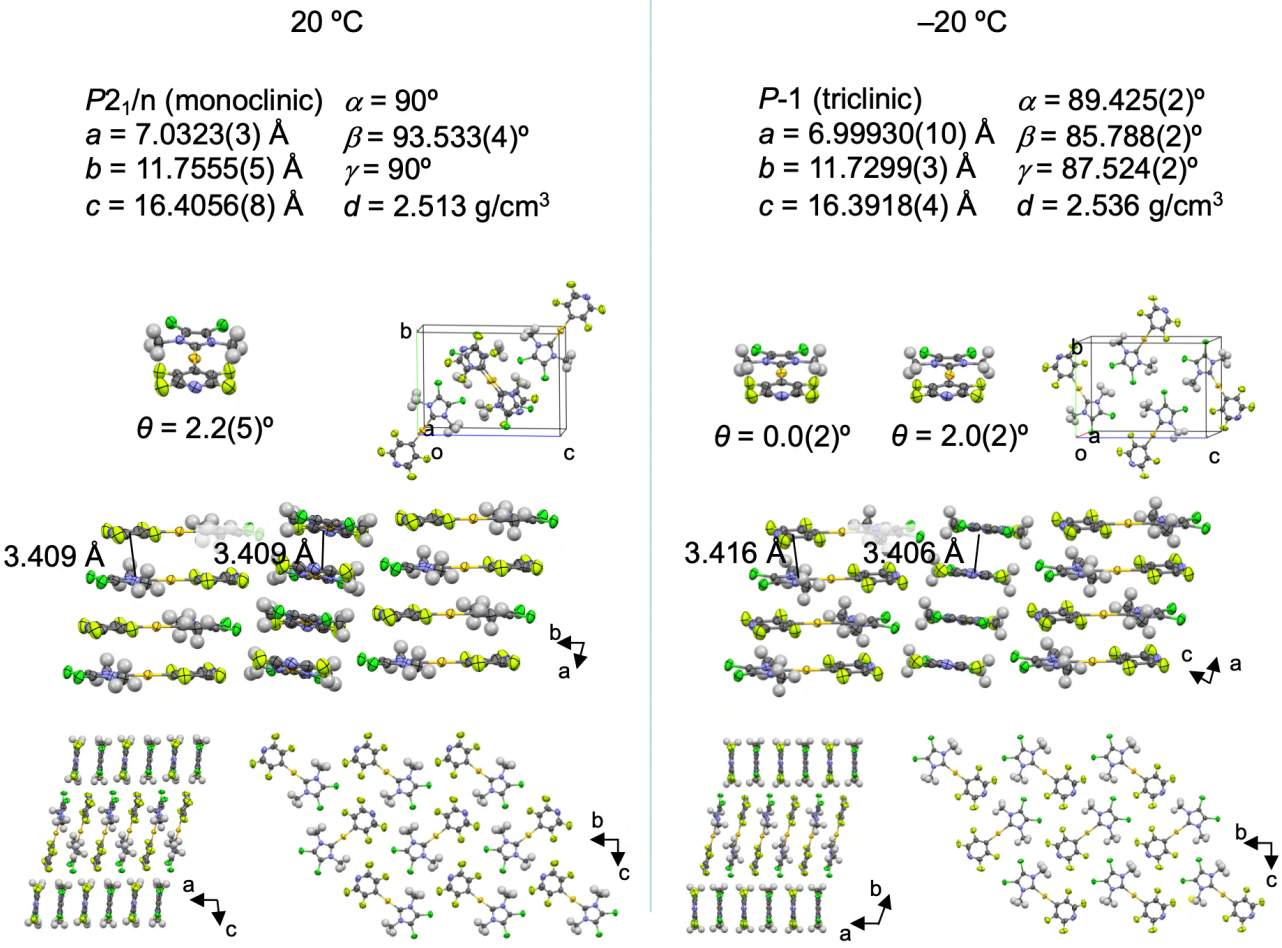

Figure S9. Comparison of the single-crystal structures of **3i** at 20 ºC and –20 ºC.

2.4.5. Mechanical properties of 3i at low temperature

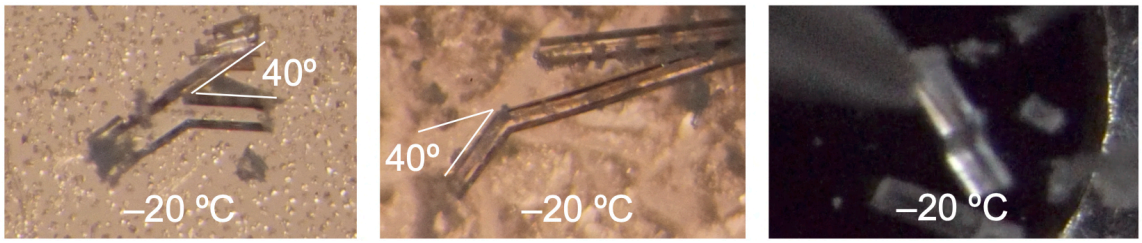

Figure S10. Photographs of mechanically bending crystals of **3i** at –20 ºC.

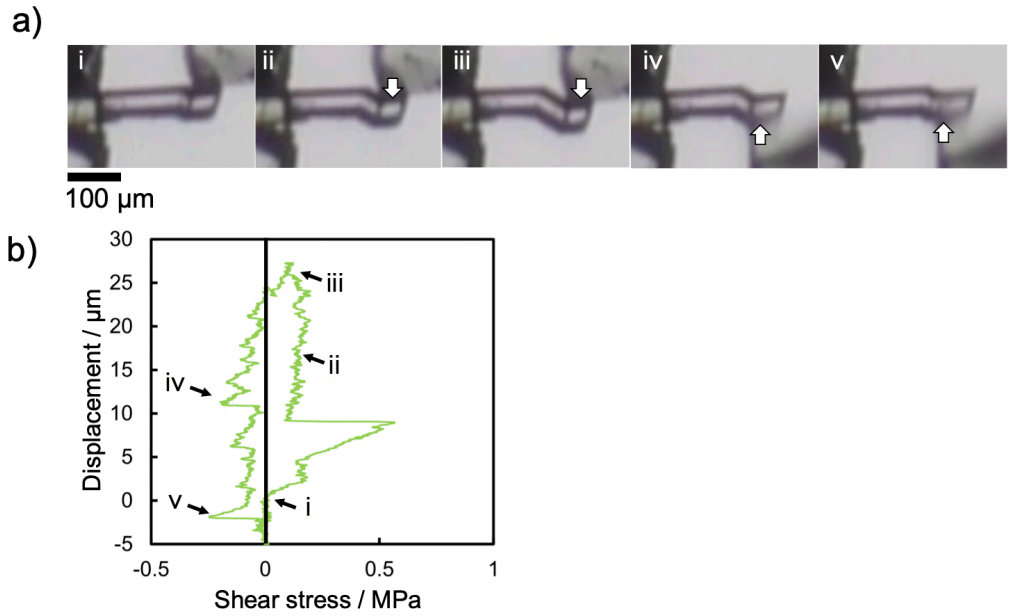

Figure S11. (a) Snapshots of ferroelastic twinning deformation of **3i** (574 × 49 × 50 μm^3) upon application of shear stress under visible (VIS) light at –1 ºC (–5~2 ºC): ii–iii) forward direction and iv–v) reverse direction. (b) Stress-displacement cycles of the crystal under VIS light.

2.4.6. Comparison of the crystal structures of 1i, 2i, 3i, and 4i.

Table 2 X-ray crystallographic data for **2i** and **4i**.

compound	**2-293 K**	**4-293 K**
CCDC Number		
Empirical Formula	$C_{12}H_{12}Au_1F_4N_3$	$C_{10}H_6Au_1F_4I_2N_3$
Formula Weight	471.21	694.94
Crystal Size / mm	0.300×0.200×0.030	0.300×0.030×0.030
Crystal System	triclinic	monoclinic
a / Å	7.3362(2)	13.3679(4)
b / Å	9.4009(4)	8.2284(2)
c / Å	11.7631(4)	27.1042(7)
α / °	70.421(3)	90
β / °	84.829(3)	94.460(2)
γ / °	67.750(3)	90
V / Å^3	706.82(5)	2972.34(14)
Space Group	*P*-1	*I2/a*
Z value	2	8
D_{calc} / g cm^{-3}	2.214	3.106
Temperature / K	293	293
$2\theta_{max}$ / °	58.712	58.456
μ / cm^{-1}	104.44 (Mo K_α)	140.88 (Mo K_α)
No. of Reflections	Total: 13191 Unique: 3398 R_{int}: 0.0448	Total: 11897 Unique: 3451 R_{int} = 0.0169
R_1[a]; wR_2[b]	0.0293; 0.0667	0.0202; 0.0467
GOF[c]	1.015	1.094
Max./Mini. peak *I*[d] / Å^3	1.04 e$^-$/−1.02 e$^-$	0.97 e$^-$/−0.72 e$^-$

[a]: For data with $I > 2.00\sigma(I)$. [b]: For all reflection data. [c]: Goodness of Fit.

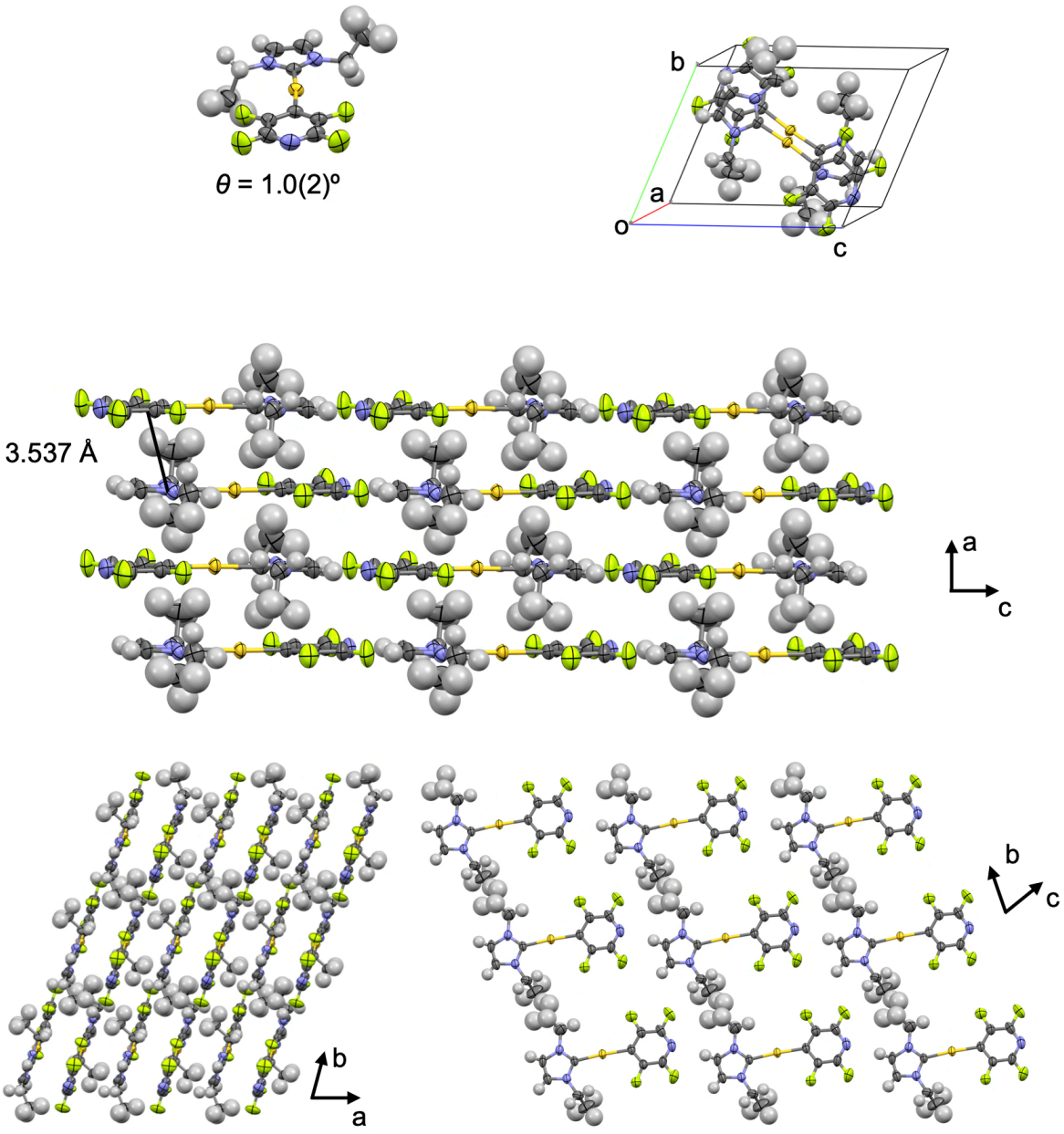

Figure S12. Single-crystal structure of **2i** at 20 ºC.

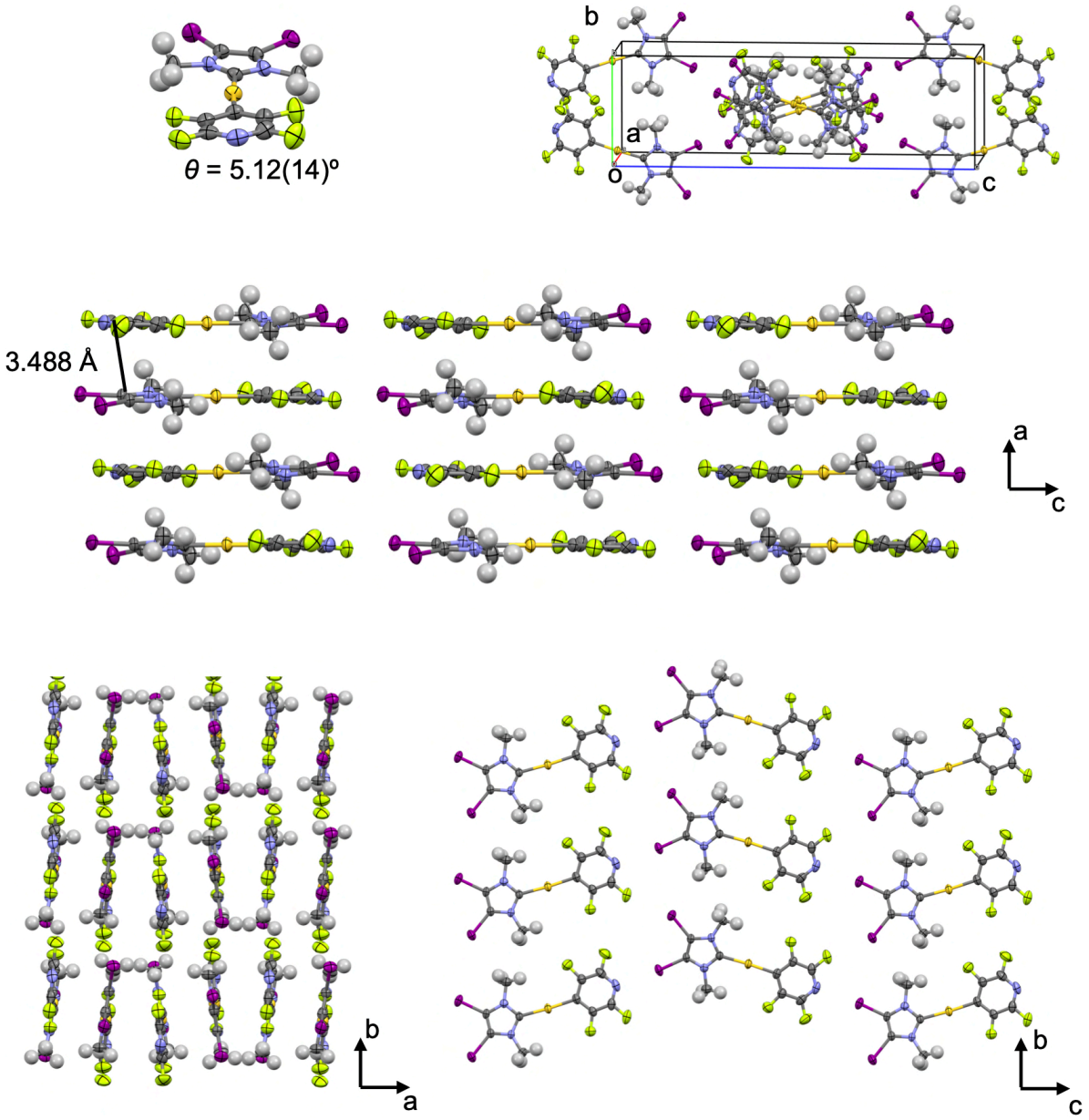

Figure S13. Single-crystal structure of **4i** at 20 ºC.

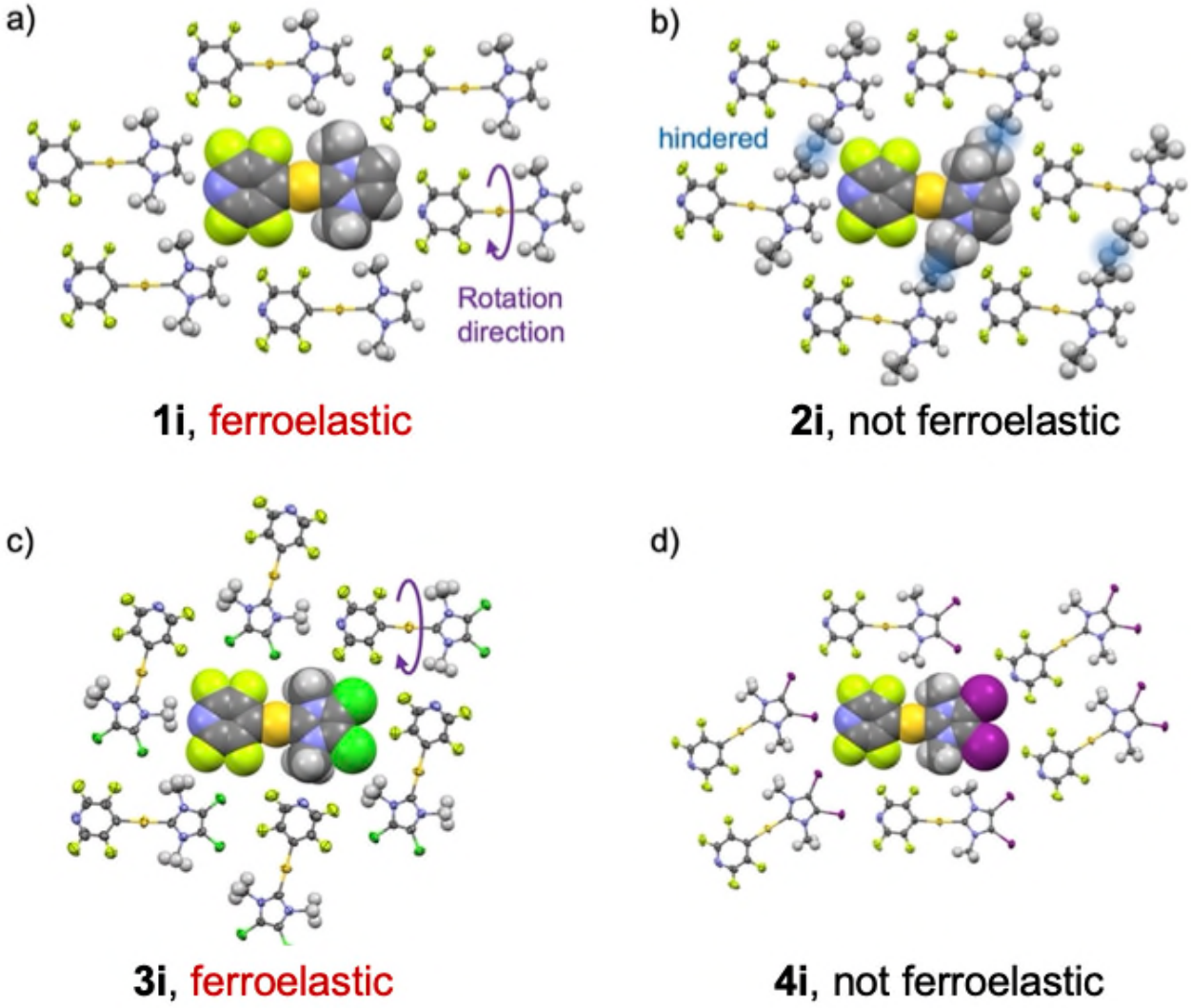

Figure S14. a) Single-crystal structure of a) **1i**, b) **2i**, c) **3i**, and d) **4i** at 20 ºC.

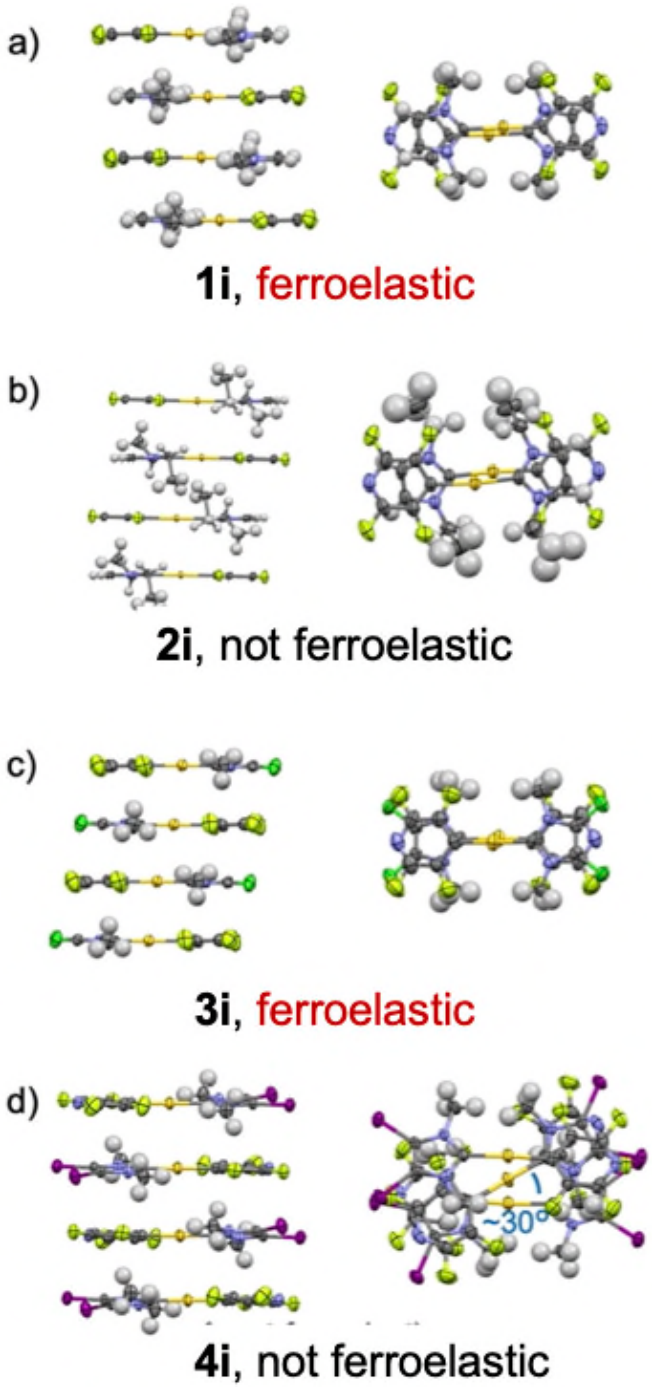

Figure S15. a) Single-crystal structure of a) **1i**, b) **2i**, c) **3i**, and d) **4i** at 20 ºC.

2.4.7. Optical properties of 1i, 2i, 3i and 4i

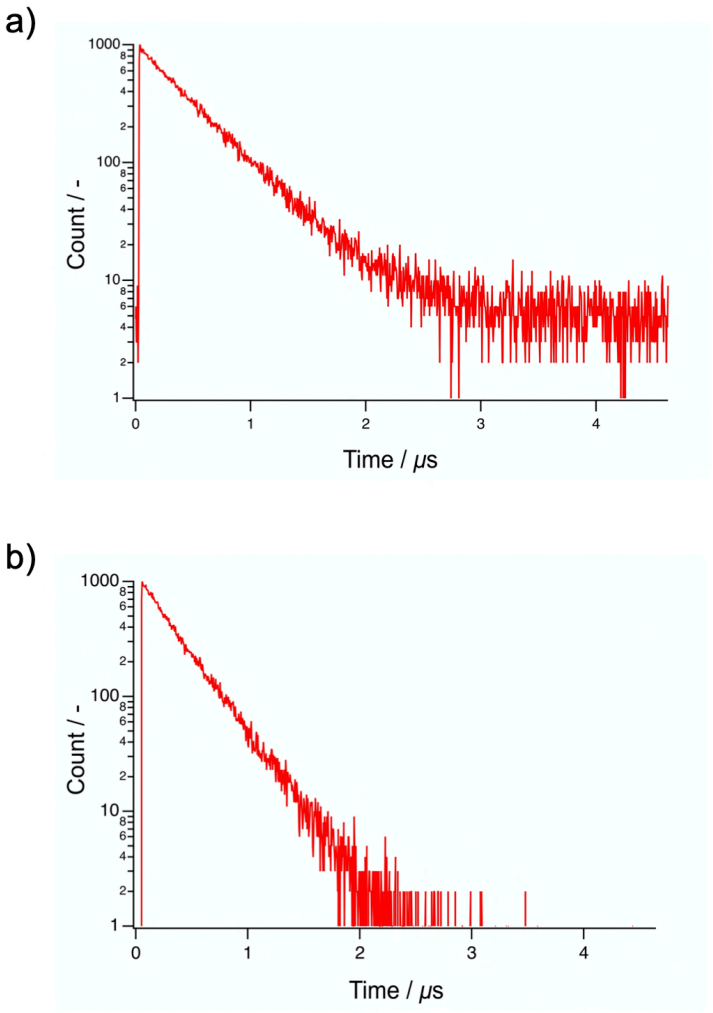

Figure S16. a) Emission decay profiles of **1i** (λ_{em} = 431 nm) and **3i** (λ_{em} = 452 nm) under excitation at 370 nm.

Table S3. Photophysical properties of the crystal samples of **1i** and **3i**.

	Φ_{em} / - (λ_{ex} / nm)	τ_{av} / μs[a,b] (λ_{em} / nm)	τ_1 / μs (A / -)	τ_2 / μs (A / -)
1i	0.65 (350)	0.43 (431)	0.14 (0.055)	0.44 (0.945)
3i	0.42 (369)	0.31 (452)	0.31 (1.000)	-

[a] λ_{ex} = 370 nm. [b] $\tau_{av} = \Sigma \tau_n A_n^2 / \Sigma \tau_n A_n$.

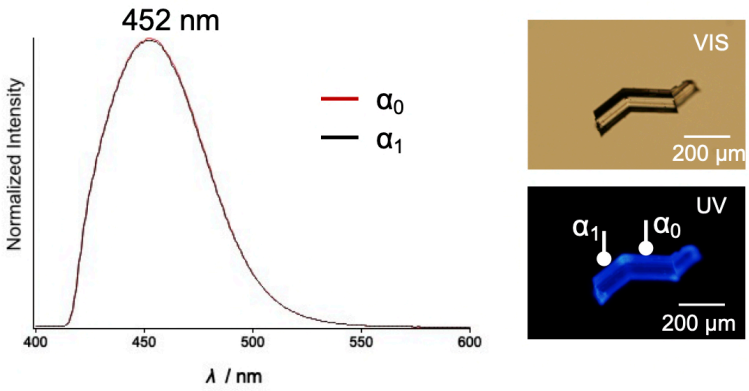

Figure S17. Microscopic photoluminescence spectra of the α_0 and α_1 domains of the crystal of **3i** (λ_{ex} = 365 nm) and its photographs taken under visible and UV light.

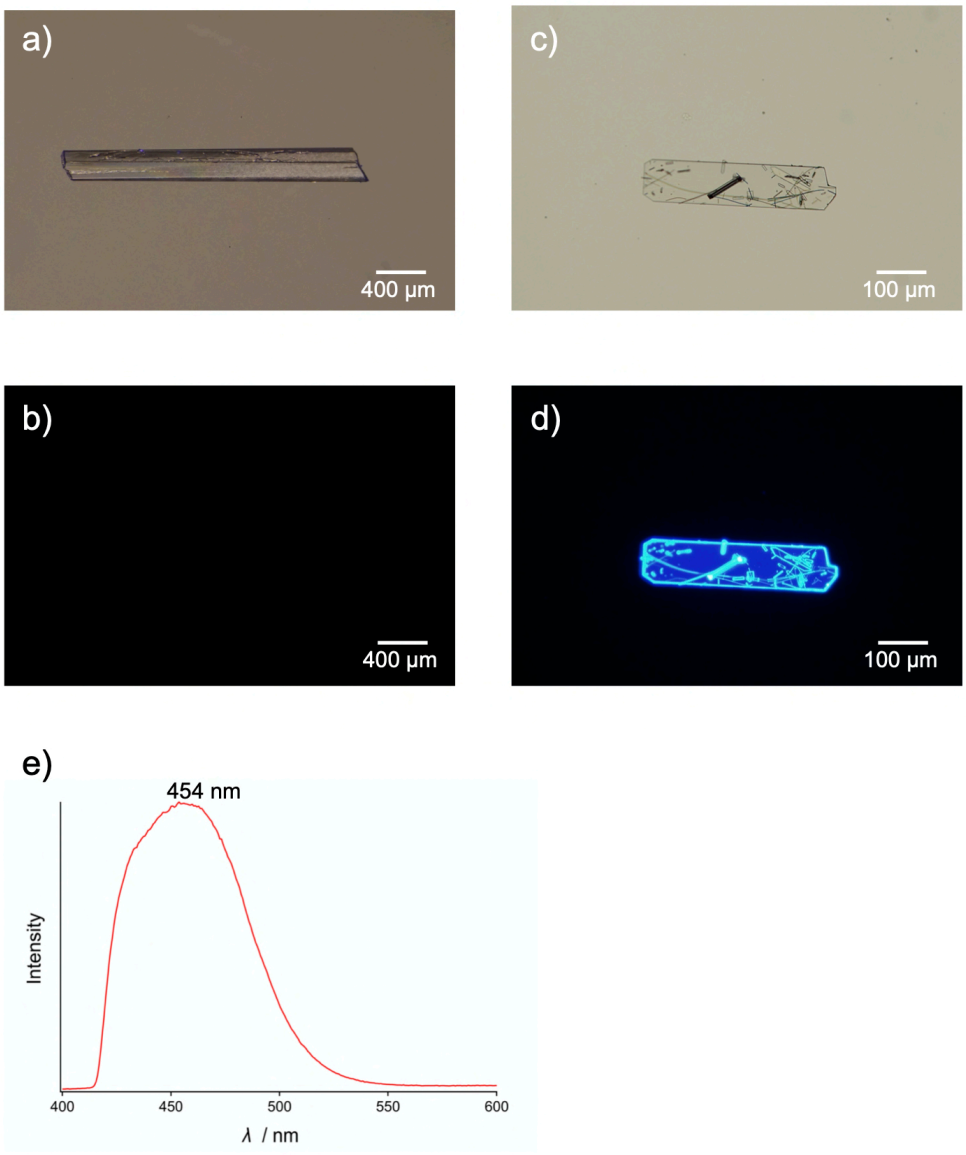

Figure S18. Photographs of crystals of **2i** observed under a) visible light, b) UV light. Photographs of crystals of **4i** observed under c) visible light, d) UV light. e) Microscopic photoluminescence spectra of the crystal of **4i** (λ_{ex} = 365 nm).

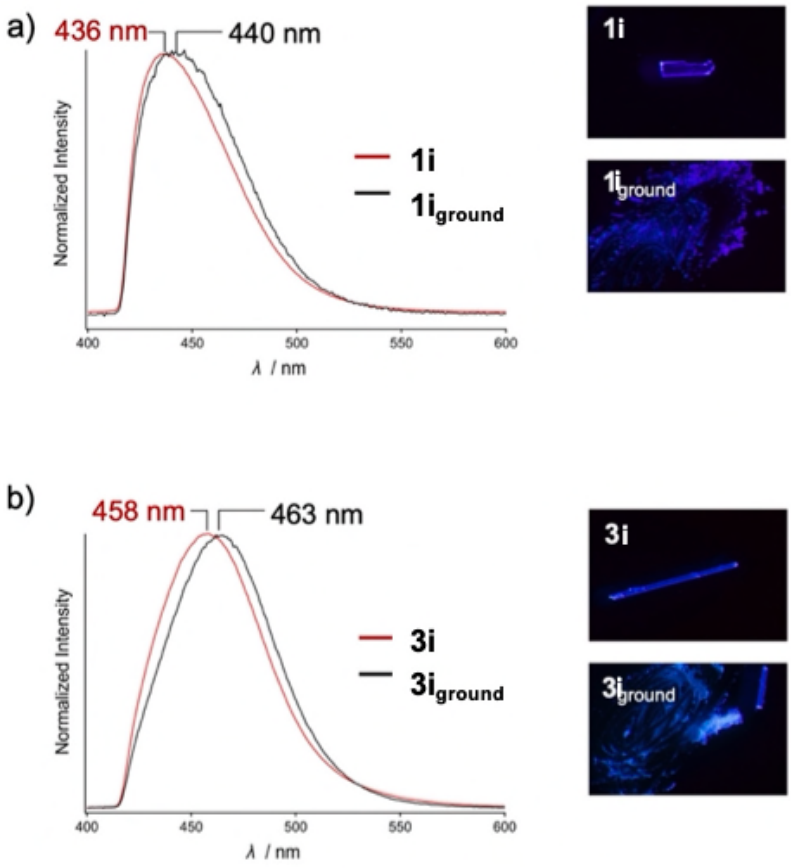

Figure S19. a) Emission spectra of the as-prepared (unground) crystal and its unground sample (**1i**$_{ground}$) of **1i** and the corresponding photographs taken under UV light (λ_{ex} = 365 nm). b) Emission spectra the as-prepared (unground) crystal and its unground sample (**3i**$_{ground}$) of **3i** and the corresponding photographs taken under UV light (λ_{ex} = 365 nm).

2.4.8. Stress-strain measurements of 1i and 3i

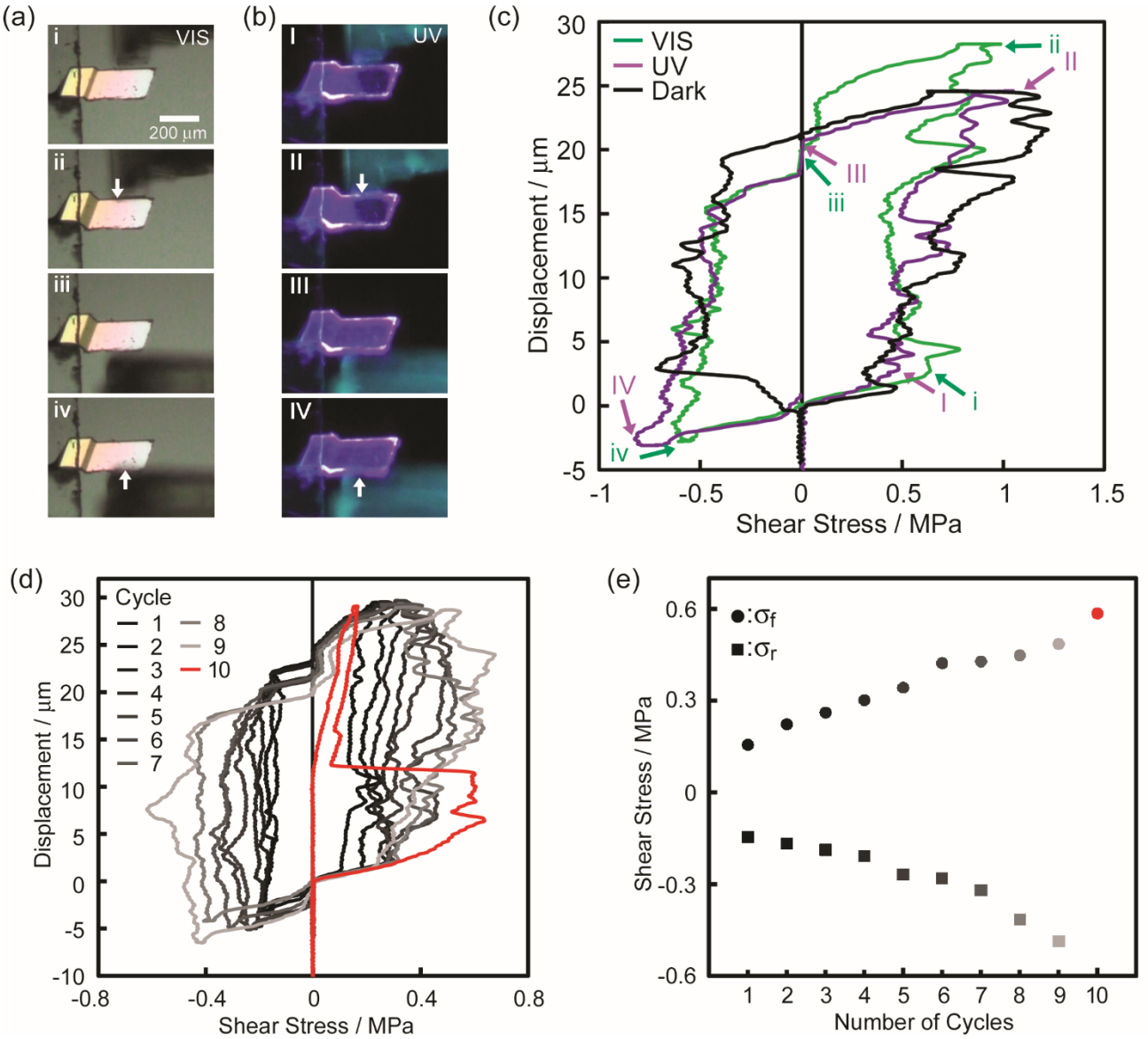

Figure S20. (a) Snapshots of ferroelastic twinning deformation of a complex **1i** crystal (403 x 147 x 35 µm^3) upon application of shear stress under visible light (VIS) and (b) under ultraviolet light (UV). (c) Stress-displacement curves of the ferroelastic deformation: under VIS (1st, green line), UV (2nd, purple line), and in the dark (Dark, 3rd, black line). The numbers i–iv and I–IV correspond with those in (a). (d) Stress-displacement curves of 10 ferroelastic deformation cycles in a complex **1i** crystal (1188 x 282 x 65 µm^3) under VIS. The crystal fractured in the 10th cycle represented in red line. (e) Stress for forward (σ_f) and reverse (σ_r) deformation in the cycles.

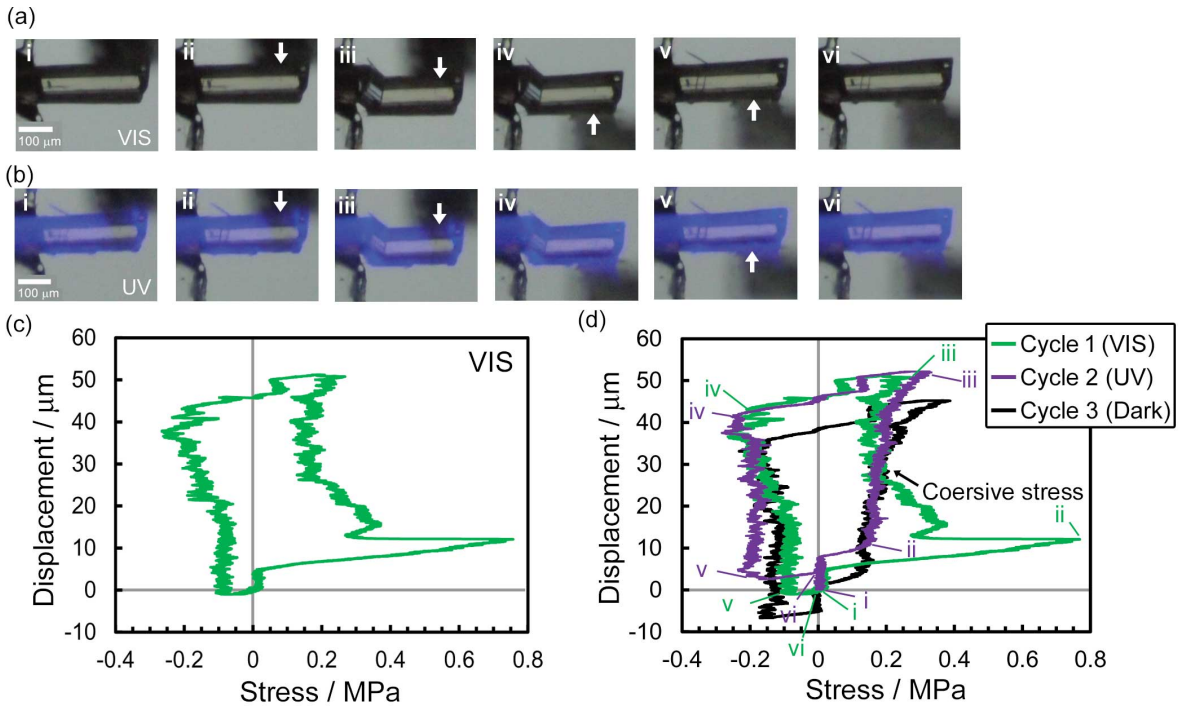

Figure S21. Snapshots of ferroelastic twinning deformation of **3i** (459 × 84 × 83 µm^3) upon application of shear stress under visible (VIS) light (a), under ultraviolet (UV) light (b): i–iii) forward direction and iv–vi) reverse direction. (c), (d) Stress-displacement cycles of the crystal under VIS light (green), under UV light (purple), and in the dark (black). The shear tests were carried out in the order of VIS, UV, and Dark in three cycles.

2.4.9. NMR spectra

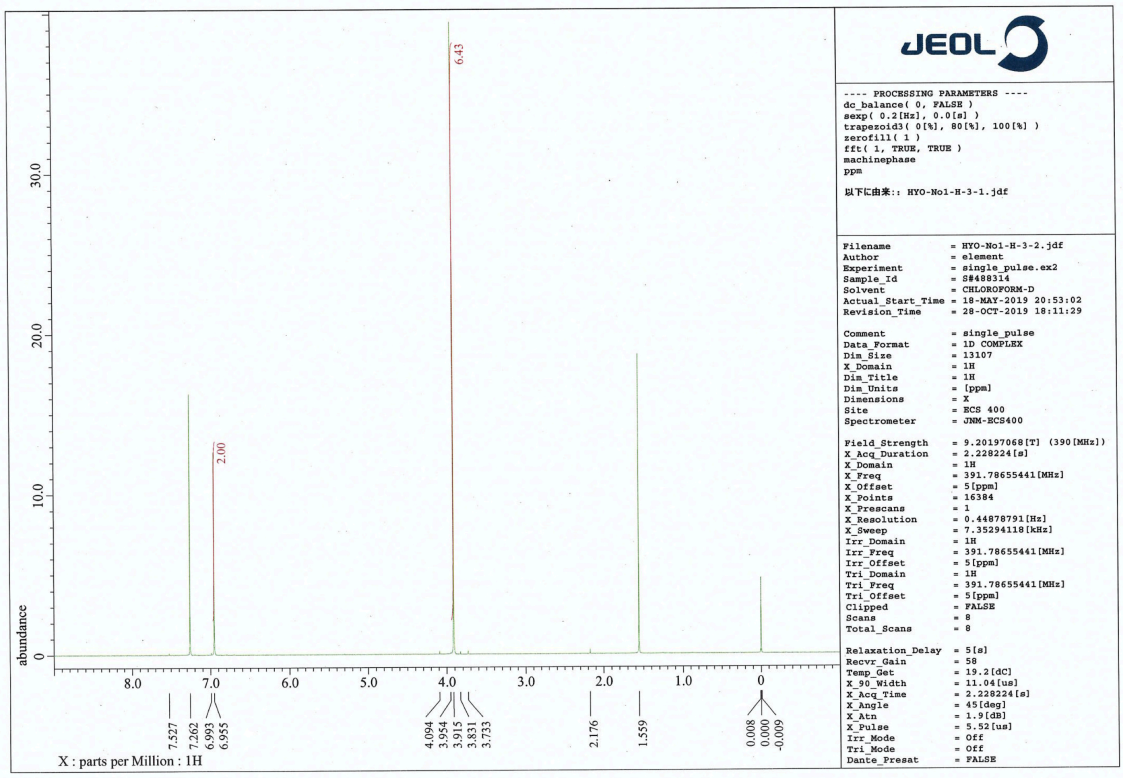

Fig. S22 NMR spectrum of **1i** in $CDCl_3$.

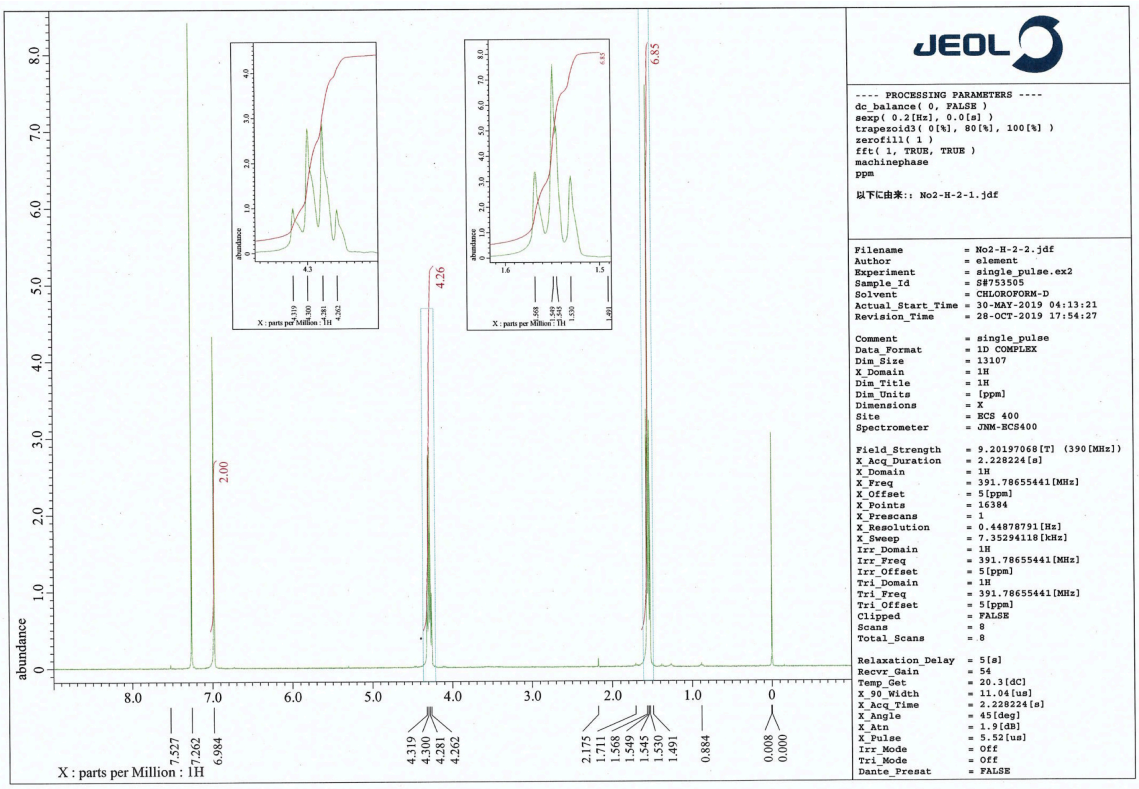

Fig. S23 NMR spectrum of **2i** in $CDCl_3$.

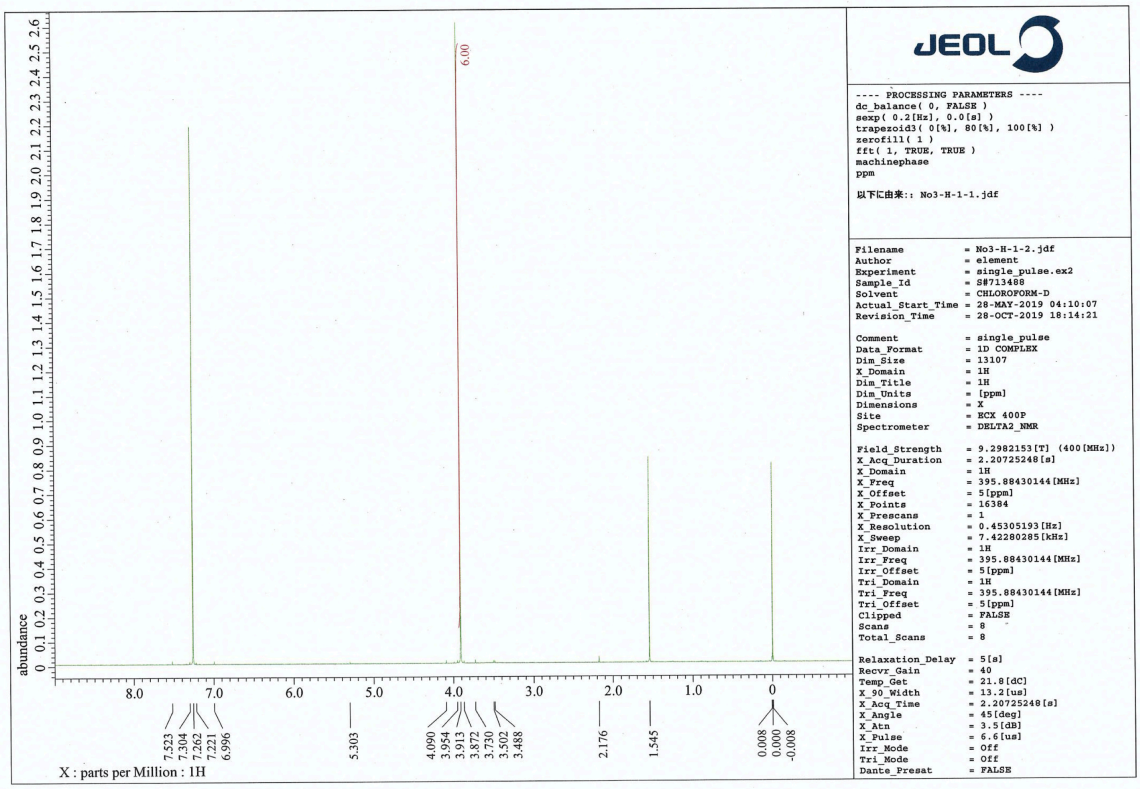

Fig. S24 NMR spectrum of **3i** in $CDCl_3$.

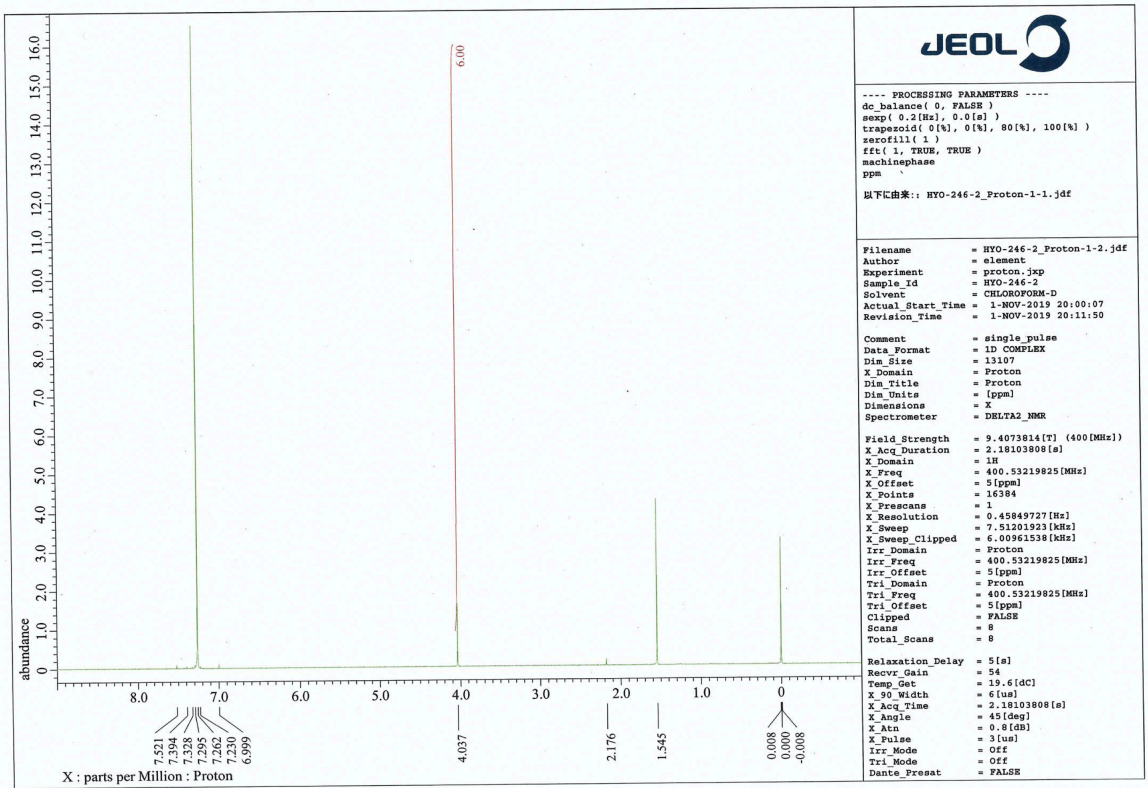

Fig. S25 NMR spectrum of **4i** in $CDCl_3$.

2.5 References

1. Fiebig, M.; Lottermoser, T.; Meier, D.; Trassin, M. The evolution of multiferroics. *Nat. Rev. Mater.* **2016**, *1*, 16046.
2. Wang, C.; Ke, X.; Wang, J.; Liang, R.; Luo, Z.; Tian, Y.; Yi, D.; Zhang, Q.; Wang, J.; Han, X. F.; Van Tendeloo, G.; Chen, L. Q.; Nan, C. W.; Ramesh, R.; Zhang, J. Ferroelastic switching in a layered-perovskite thin film. *Nat. Commun.* **2016**, *7*, 10636.
3. Strelcov, E.; Dong, Q.; Li, T.; Chae, J.; Shao, Y.; Deng, Y.; Gruverman, A.; Huang, A. Centrone, A. $CH_3NH_3PbI_3$ perovskites: Ferroelasticity revealed. *Sci. Adv.* **2017**, *3*, e1602165.
4. Suzuki, I.; Okada, K.; Direct observation of ferroelasticity in squaric acid $C_4H_2O_4$. *Solid State Commun.* **1979**, *29*, 759–762.
5. Mir, S. H.; Takasaki, Y.; Engel, E. R.; Takamizawa, S. Ferroelasticity in an Organic Crystal: A Macroscopic and Molecular Level Study. *Angew. Chem., Int. Ed.* **2017**, *56*, 15882–15885.
6. Mir, S. H. Takasaki, Y.; Takamizawa, S. An organoferroelasticity driven by molecular conformational change. *Phys. Chem. Chem. Phys.* **2018**, *20*, 4631–4635.
7. Engel, E. R.; Takasaki, Y.; Mir, S. H.; Takamizawa, S. Twinning ferroelasticity facilitated by the partial flipping of phenyl rings in single crystals of 4,4'-dicarboxydiphenyl ether. *R. Soc. Open Sci.* **2018**, *5*, 171146.
8. Mir, S. H.; Takasaki, Y.; Engel, E. R.; Takamizawa, S. Controllability of coercive stress in organoferroelasticity by the incorporation of a bulky flipping moiety in molecular crystals. *CrystEngComm* **2018**, *20*, 3807–3811.
9. Mir, S. H.; Takasaki, Y.; Engel, E. R.; Takamizawa, S. Enhancement of dissipated energy by large bending of an organic single crystal undergoing twinning deformation. *RSC Adv.* **2018**, *8*, 21933–21936.
10. Takamizawa, S.; Takasaki, Y. Shape-memory effect in an organosuperelastic crystal. *Chem. Sci.* **2016**, *7*, 1527–1534.
11. Takamizawa, S.; Takasaki, Y. Versatile Shape Recoverability of Odd-Numbered Saturated Long-Chain Fatty Acid Crystals. *Cryst. Growth Des.* **2019**, *19*, 1912–1920.
12. Sakamoto, S.; Sasaki, T.; Sato-Tomita, A.; Takamizawa, S. Shape Rememorization of an Organosuperelastic Crystal through Superelasticity–Ferroelasticity Interconversion. *Angew. Chem., Int. Ed.* **2019**, *58*, 13722–13726.
13. Miyamoto, Y.; Takamizawa, S. Deformation twinning of ferrocene crystals assisted by the rotational mobility of cyclopentadienyl rings. *Dalton Trans.* **2015**, *44*, 5688–5691.
14. In ref. [13]: Although mechanical deformation of the metallocene crystals due to twinning was

confirmed, the spontaneous build-up of strain required for ferroelasticity was not observed.

15. Pyykkö, P. Theoretical Chemistry of Gold. *Angew. Chem., Int. Ed.* **2004**, *43*, 4412–4456.
16. Yam, V. W.; Cheng, E. C. Highlights on the recent advances in gold chemistry—a photophysical perspective. *Chem. Soc. Rev.* **2008**, *37*, 1806–1813.
17. Schmidbaur, H.; Schier, A. A briefing on aurophilicity. *Chem. Soc. Rev.* **2008**, *37*, 1931–1951
18. Osawa, M.; Kawata, I.; Igawa, S.; Hoshino, M.; Fukunaga, T.; Hashizume, D. Vapochromic and Mechanochromic Tetrahedral Gold(I) Complexes Based on the 1,2-Bis(diphenylphosphino)benzene Ligand. *Chem. -Eur. J.* **2010**, *16*, 12114–12126.
19. Ito, H.; Muromoto, M.; Kurenuma, S.; Ishizaka, S.; Kitamura, N.; Sato, H.; Seki, T. Mechanical stimulation and solid seeding trigger single-crystal-to-single-crystal molecular domino transformations. *Nat. Commun.* **2013**, *4*, 2009.
20. Baranyai, P.; Marsi, G.; Jobbagy, C.; Domjan, A.; Olah, L.; Deak, A. Mechano-induced reversible colour and luminescence switching of a gold(i)–diphosphine complex. *Dalton Trans.* **2015**, *44*, 13455–13459.
21. Seki, T.; Takamatsu, Y.; Ito, H. A Screening Approach for the Discovery of Mechanochromic Gold(I) Isocyanide Complexes with Crystal-to-Crystal Phase Transitions. *J. Am. Chem. Soc.* **2016**, *138*, 6252–6260.
22. Jin, M.; Seki, T.; Ito, H. Mechano-Responsive Luminescence via Crystal-to-Crystal Phase Transitions between Chiral and Non-Chiral Space Groups. *J. Am. Chem. Soc.* **2017**, *139*, 7452–7455.
23. Seki, T.; Tokodai, N.; Omagari, S.; Nakanishi, T.; Hasegawa, Y.; Iwasa, T.; Taketsugu, T.; Ito, H. Luminescent Mechanochromic 9-Anthryl Gold(I) Isocyanide Complex with an Emission Maximum at 900 nm after Mechanical Stimulation. *J. Am. Chem. Soc.* **2017**, *139*, 6514–6517.
24. Jin, M.; Sumitani, T.; Sato, H.; Seki, T.; Ito, H. Mechanical-Stimulation-Triggered and Solvent-Vapor-Induced Reverse Single-Crystal-to-Single-Crystal Phase Transitions with Alterations of the Luminescence Color. *J. Am. Chem. Soc.* **2018**, *140*, 2875–2879.
25. Seki, T.; Mashimo, T.; Ito, H. Anisotropic strain release in a thermosalient crystal: correlation between the microscopic orientation of molecular rearrangements and the macroscopic mechanical motion. *Chem. Sci.* **2019**, *10*, 4185–4191.
26. Seki, T.; Kashiyama, K.; Ito, H. Luminescent mechanochromism of gold N-heterocyclic carbene complexes with hypso- and bathochromic spectral shifts. *Dalton Trans.* **2019**, *48*, 7105–7109.
27. Jin, M.; Chung, T. S.; Seki, T.; Ito, H.; Garcia-Garibay, M. A. Phosphorescence Control

Mediated by Molecular Rotation and Aurophilic Interactions in Amphidynamic Crystals of 1,4-Bis[tri-(p-fluorophenyl)phosphane-gold(I)-ethynyl]benzene. *J. Am. Chem. Soc.* **2017**, *139*, 18115–18121.

28. Chen, Y.; Cheng, G.; Li, K.; Shelar, D. P.; Lu, W.; Che, C.-M. Phosphorescent polymeric nanomaterials with metallophilic d10···d10 interactions self-assembled from $[Au(NHC)_2]^+$ and $[M(CN)_2]^-$ *Chem. Sci.* **2014**, *5*, 1348–1353.
29. Penney, A. A.; Sizov, V. V.; Grachova, E. V.; Krupenya, D. V.; Gurzhiy, V. V.; Starova, G. L.; Tunik, S. P. Aurophilicity in Action: Fine-Tuning the Gold(I)–Gold(I) Distance in the Excited State To Modulate the Emission in a Series of Dinuclear Homoleptic Gold(I)–NHC Complexes. *Inorg. Chem.* **2016**, *55*, 4720–4732.
30. Crudden, C. M.; Horton, J. H.; Ebralidze, I. I.; Zenkina, O. V.; McLean, A. B.; Drevniok, B.; She, Z.; Kraatz, H.-B.; Mosey, N. J.; Seki, T.; Keske, E. C.; Leake, J. D.; Rousina-Webb, A.; Wu, G. Ultra stable self-assembled monolayers of N-heterocyclic carbenes on gold. *Nat. Chem.* **2014**, *6*, 409–414.
31. Narouz, M. R.; Osten, K. M.; Unsworth, P. J.; Man, R. W. Y.; Salorinne, K.; Takano, S.; Tomihara, R.; Kaappa, S.; Malola, S.; Dinh, C. T.; Padmos, J. D.; Ayoo, K.; Garrett, P. J.; Nambo, M.; Horton, J. H.; Sargent, E. H.; Hakkinen, H.; Tsukuda, T.; Crudden, C. M. N-heterocyclic carbene-functionalized magic-number gold nanoclusters. *Nat. Chem.* **2019**, *11*, 419–425.
32. Johnson, A.; Gimeno, M. C. An efficient and sustainable synthesis of NHC gold complexes. *Chem. Commun.* **2016**, *52*, 9664–9667.
33. The single crystal structure analyses of as-prepared crystals of **1i** and **3i** do not show twinning, supporting the fact that the twinning of the bent crystals of these complexes takes place upon mechanical bending.
34. The single crystal structures analyses at lower temperature (i.e., at −20 °C) are shown in Figure S6 and S8 for **1i** and **3i**, respectively, and Table S1.
35. For **3i**, slight crystal structure change was obserbed upon cooling below 0°C (Figure S7, S8, and S9). Even under lower temperature (i.e., –20°C), mechanical crystal bending with bending angle of ~40° is possible without breakage of the crystals (Figure S10). We also confiemd that **3i** can show "superelastic" bahavior below −40 °C, which will be descrived in detail elsewhere. For "superelasticity", see Takamizawa, S.; Miyamoto, Y. *Angew. Chem. Int. Ed.* **2014**, *53*, 6970 – 6973.
36. A similar ferroelastic stress-strain response of **3i** can be confirmed at –18 ºC with coercive

forward and reverse stress of 0.14 and –0.08 MPa, respectively (Supporting Information, Figure S11).

37. The optical properties of **2i** and **4i** are shown in Figure S18 in the Supporting Information.
38. Even upon thorough grinding, **1i** and **3i** do not show luminescent mechanochromism (Supporting Information, Figure S19).
39. Sheldrick, G. M. SHTLXT - Integrated space-group and crystal-structure determination. *Acta Cryst.* **2015**, *A71*, 3–8.
40. https://www.ccdc.cam.ac.uk/support-and-resources/Downloads/
41. Johnson, A.; Gimeno, M. C. An efficient and sustainable synthesis of NHC gold complexes. *Chem. Commun*. **2016**, *52*, 9664–9667.
42. Seki, T.; Ozaki, T.; Okura, T.; Asakura, K.; Sakon, A.; Uekusa, H.; Ito, H. Interconvertible multiple photoluminescence color of a gold(i) isocyanide complex in the solid state: solvent-induced blue-shifted and mechano-responsive red-shifted photoluminescence. *Chem. Sci*. **2015**, *6*, 2187–2195.
43. Liu, W.; Bensdorf, K.; Proetto, M.; Abram, U.; Hagenbach, A.; Gust, R. NHC Gold Halide Complexes Derived from 4,5-Diarylimidazoles: Synthesis, Structural Analysis, and Pharmacological Investigations as Potential Antitumor Agents. *J. Med. Chem*. **2011**, *54*, 8605–8615.
44. Hindi, K. M.; Siciliano, T. J.; Durmus, S.; Panzner, M. J.; Medvetz, D. A.; Reddy, D. V.; Hogue, L. A.; Hovis, C. E.; Hilliard, J. K.; Mallet, R. J.; Tessier, C. A.; Cannon, C. L.; Youngs, W. J. Synthesis, Stability, and Antimicrobial Studies of Electronically Tuned Silver Acetate N-Heterocyclic Carbenes. *J. Med. Chem*. **2008**, *51*, 1577–1583.
45. He, C.; Hooper, J. P.; Shreeve, J. M. Iodine-Rich Imidazolium Iodate and Periodate Salts: En Route to Single-Based Biocidal Agents. *Inorg. Chem*. **2016**, *55*, 12844–12850.

III Mechanical Deformation and Multiple Thermal Restoration of Organic Crystals: Reversible Multi-Stage Shape-Changing Effect with Luminescence-Color Changes

3.1. Introduction

The shape memory effect is a phenomenon that a material that could be mechanically deformed and subsequently eliminate the deformation upon temperature change. After their first discovery in 1951, the shape memory effect attracted consider-able attention because of its great scientific and technological significance.[1,2] Until today, Ni-Ti metal alloys are the most commonly applied in various fields of science and engineering. Polymers as a relatively new class of shape recovery mate-rials are also attracting increasing attention after the 1980s.[3] Many shape-memory materials are already practically used in the fields of surgical treatment, mechanical engineering, and clothing, are expected to be applied in the fields of aerospace and robotics.[2,3,8–11] In the typical shape memory effect of metal alloys and polymers, the material can be deformed at a low temperature and returns to the pre-deformed shape at a high temperature. However, despite significant advances in shape-memory materials, it is still difficult to impart further functions to the known shape-memory materials, for example, multi-stage and anisotropic shape changes,[12–24] and changes in light absorbance and emission accompanying by shape changes. [25–28] This is because the shape memory properties of metal alloys and polymers are strongly depending on their components or chemical structures, and it is difficult to alter their atomic or molecular level structure with keeping the shape memory effect.

Dynamic molecular crystals that are responsive to external stimuli have drawn increasing attention in recent years. Upon applying external stimuli, these dynamic molecular crystals show macroscopic dynamic effects such as bending, jumping, crawling, or creeping.[29–33] In 2016, the groups of Naumov[34] and Takamizawa[35] almost simultaneously reported the first examples of organic molecular crystals with shape-memory phenomena (Figure 1) These crystals can be bent mechanically, resulting in a stress-induced martensitic transformation. Upon heating, the deformed crystals regain its straight shape. The mechanism of the shape-memory phenomena can be expected to be different from those reported for metal alloys and polymers, and I observed similar "shape-deformation and -restoration (shape-memory)" behavior. The findings suggest that variations in shape-memory materials, previously limited to metal alloys and polymers, can broaden significantly. In addition, the possibility that unprecedented functionality, which conventional shape-memory materials do not have, can be discovered into shape-memory materials by considering characteristics of organic crystals, such as anisotropic and multiple shape change[12–24], optical preparties alternations.[25–28,36–51]

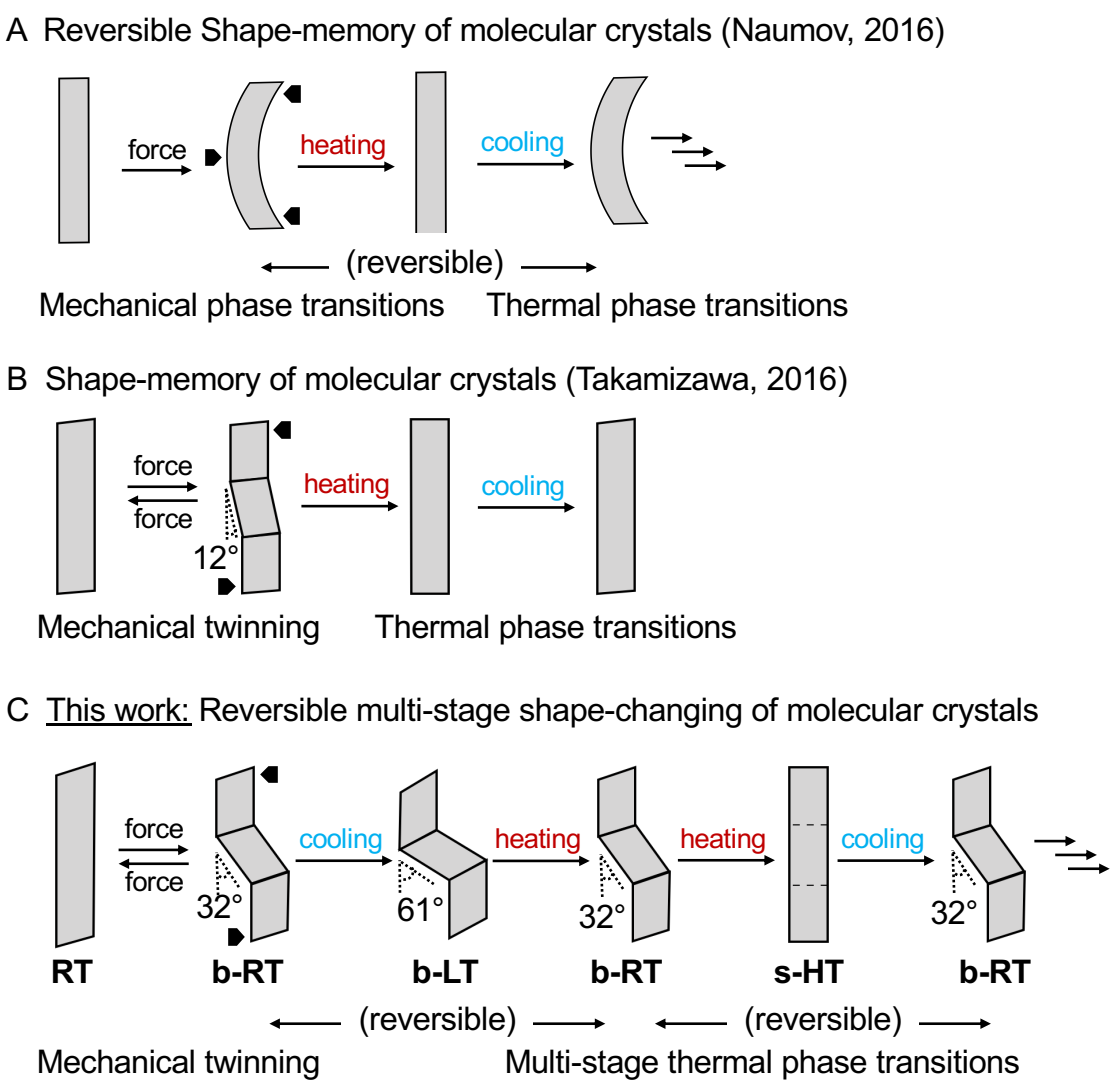

Figure 1. Schematic illustration of the shape-changing effect of molecular crystals after mechanical deformation. A) Reversible shape changing through a combination of mechanical and thermal phase transitions. B) Shape changing through a combination of mechanical twinning and thermal phase transitions. C) Reversible shape-changing through a combination of mechanical twinning and multi-step thermal phase transitions.

I previously reported gold(I) complexes with ferroelastic properties where its crystal shape could be deformed by force accompanied by twinning deformation.[46] The gold(I) crystals show luminescent properties under UV light illumination. The previous crystals have no response against temperature change, but we expected that we would develop a crystalline compound that exhibits both temperature-dependent reversible crystal phase change and ferroelasticity with alternations of the crystal shape and luminescence. Here, I report molecular crystals of an arylgold(I)(*N*-heterocyclic carbene) (NHC) complex with a reversible shape-changing effect. The materials remember three different shapes and cycled fairly reproducibly among different shapes upon changing the temperature even after regaining its straight shape.

The reversible shape-changing effect was achieved by a combined process twinning deformation and multi-step thermal phase transitions., i.e., a low temperature (**LT**), room temperature (**RT**), and high temperature (**HT**) phase. Moreover, Ferroelastic behavior,[29,46–59] i.e., mechanical-stress-induced twinning deformation with spontaneous straining, was found in the **RT** crystal (Figure 1). The **RT** crystal shows mechanical bending with zigzag morphology. The bent **RT** (*b*-RT) further transforms into bent **LT** (*b*-LT) with enhanced zigzag morphology upon cooling (Figure 1). Intriguingly, this shape change is reversible, the zigzag morphology of ***b*-RT** is recovered upon heating ***b*-LT**, which confirms reversible shape-changing effect. (Figure 1). However, when ***b*-RT** is heated to give straight **HT** (***s*-HT**), the zigzag morphology is lost, and the bent crystal regain its straight shape (Figure 1). Surprisingly, once memorized crystals can change their shape upon temperature change reversibly even after disappearance of the bent shape at ***s*-HT** phase**.** The zigzag-shaped ***b*-RT** and ***b*-LT** could be reproduced upon cooling straight ***s*-HT** (Figure 1). This full reversibility is able to vary among distinct shapes without external force by simply changing in temperature. Interestingly, the transformations among the three shapes are accompanied by changes of the luminescence color. To the best of our knowledge, such reversible shape-changing materials with luminescence-color changes have not yet been reported. Based on XRD, spectroscopic, and thermal analyses, as well as mechanical-property measurements, I will discuss the origin of this unique stimulus-responsivity.

3.2. Results and Discussion

Complex **1j** was prepared according to our previously reported procedure.[46] Under crystallization conditions, the pristine crystal of **1f** can be obtained as a colorless parallelogram plate with corner angles of 74°, which is hereafter referred to as **RT** (Figure 2 and Figure S1). Under exposure to UV light, the **RT** crystal shows weak yellow photoluminescence.

I found that the crystal of **1f** exhibits simultaneous luminescent and morphological changes in response to temperature changes. Upon cooling **RT**, the emission intensity gradually enhanced up to ~193 K (Figure 2D, ii). Further cooling to ~173 K, the crystal shape started to change and several ordered crystalline domains with pale yellow-green emission appeared within the original yellow-emitting **RT** domain (Figure 2D, iii). Upon further cooling to ~93 K, this pale yellow-green-emitting crystal domain gradually expanded, accompanied by prominent morphological change (Figure 2D, iv). Eventually, a more oblique parallelogram crystal with corner angles of 60° was obtained. The resulting crystal with yellow-green emission will be referred to as **LT**. Both emission color and shape change are reversible between the **LT** and **RT** crystals by temperature change: upon heating **LT**, **RT** was recovered at ~273 K (Figure 2D, vi). When further heating **RT**, gradual macroscopic morphological changes were again started at ~360 K. After further heating to ~373 K, a rectangular crystal was obtained, which is hereafter called **HT** (Figure 2D, viii). The conversion of **RT** to **HT** also leads to the emission color change: **HT** shows weak green photoluminescence. The intensity of photoluminescence was enhanced upon cooling to ~303 K (Figure 2D, ix). Upon further cooling, the recovery of the emission color and shape was confirmed at ~293 K because of the phase transition from **HT** to **RT** (Figure S1 and S2). The reversible shape deformation of the **LT**, **RT**, and **HT** has performed at least 16 heating/cooling cycles without visible cracking of the crystals (Figure S3). A differential scanning calorimetry (DSC) analysis confirmed the reversibility of the transitions among the three phases (**RT** to **LT**: 191 K; **LT** to **RT**: 237 K; **RT** to **HT**: 324 K; **HT** to **RT**: 296 K; Figure 2D and Figure S4). Differential scanning calorimetry (DSC) analyses of **1f** clearly demonstrated the reversible phase transitions among three phases. DSC analysis of **1** starts with cooling **RT** from 303 K, which found one exothermic peak at 191 K (Figure S4). This exothermic peak can be attributed to the phase transition from **RT** to **LT**. Upon heating **LT** from 123 K, the thermogram exhibits two endothermic peaks at 238 K and 324 K. They are corresponding to the sequential phase transitions from **LT** to **RT** and then to **HT**. When cooling **HT** from 393 K, one exothermic peak appeared around at 296 K assignable to the recovery phase transition into **RT**. The similar DSC thermograms were confirmed over three times (Figure S4), which confirms the reversible phase transitions of **1f** among three phases. These observations confirmed that the crystal of **1f** shows a reversible emission color and macroscopic morphological changes upon cooling/heating.

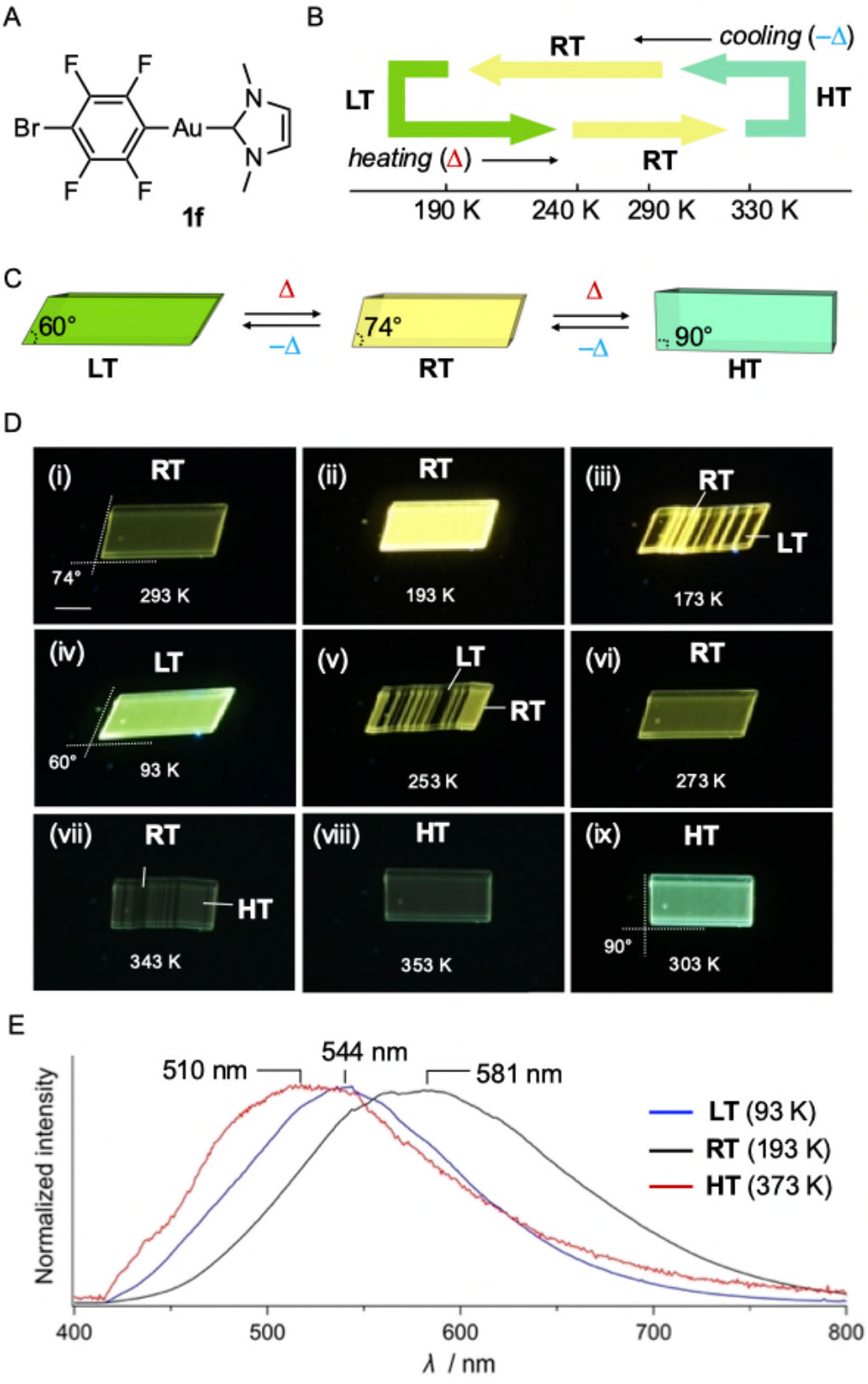

Figure 2. Simultaneous luminescence and morphology changes of a crystal of **1f** upon changing the temperature. A) Molecular structure of **1f**. B, C) Schematic illustration of the thermal transitions for the low temperature (**LT**, yellow-green), room temperature (**RT**, yellow), and high temperature (**HT**, green) phases of a crystal of **1f**. D) Photographs of a crystal of **1f** under UV light at cooling/heating

rates of 20 K min^{-1}. E) Photoluminescence spectra of **LT**, **RT**, and **HT** crystals of **1f** (λ_{ex} = 365 nm) (for further details, see Supporting Information, Figure S5–8 and Table S1); scale bars: 100 μm.

The photophysical properties of the **LT**, **RT**, and **HT** crystals were investigated. Because yellow photoluminescence of the **RT** is strong upon moderate cooling (Figure 2D, ii), the emission spectrum of **RT** was measured at 193 K. Under UV light irradiation, the **RT** crystal exhibited an emission spectrum with its maximum at 581 nm (Figure 2E and Supplementary Figure S5). Next, I measured an emission spectrum of **LT** at 93 K. **LT** showed an emission spectrum with a maximum at 544 nm. This indicates a blue-shifted emission band upon cooling (Figure 2E and Supplementary Figure S5). I also measured an emission spectrum of **HT** at 373 K. Similar to **RT**, **HT** exhibited a broad emission spectrum. However, the peak maximum of **HT** is observed at 510 nm, which is in the shortest emission maximum wavelength compared to **RT** and **LT** (Figure 2E and Supplementary Figure S5). I also confirmed that the **RT** crystal recovered from **LT** or **HT** also showed an emission spectrum similar to that of its original **RT** (Supplementary Figure S5), indicative of the reversibility of the photophysical properties.

Single-crystal structure analyses demonstrate that the **LT**, **RT**, and **HT** crystal structures are different from each other. The single-crystal analysis of **LT** was performed at 123 K, which indicates that **LT** crystallized in a monoclinic space group of $P2_1/c$ at 123 K (Supplementary Table S2). In **LT**, the molecule of **1f** has a flat conformation with a dihedral angle (θ) between an NHC ring and a halogenated benzene ring on Au is 2.5789(2)° (Figure 3B and Supplementary Figure S9). The flat conformation of molecule **1f** formed dimers with a head-to-tail arrangement through π-π stacking interactions between the NHC ring and the benzene ring (heterogeneous stack) with longitudinal offset (Supplementary Figure S9). The dimers interacted with adjacent dimers through π-π stacking interactions between the NHC rings (or benzene rings, homogeneous stack), allowing the formation of a zigzag stacking motif. To investigate the crystal structure of **RT**, XRD analyses of the same piece of the crystal was next performed at 293 K. **RT** exhibits a crystal structure different from **LT**. The space group of **RT** was monoclinic $P2_1/c$ (Supplementary Table S2). In **RT**, the molecules also adopt flat conformations with θ = 4.1(3)° or 0.2(3)° (Figure 3B and Supplementary Figure S10). These flat molecules formed π-π stacking interaction with a head-to-tailed arrangement. The stacked four molecules (tetramers units) contact with adjacent tetramers through homogeneous π-π stacking interactions between the NHC rings (or benzene rings) along the crystallographic *a*-axis. For the crystal structure analysis of **HT**, single-crystal XRD measurement of the same piece of the crystal was performed at 363 K. The **HT** crystal showed the symmetry change from monoclinic to orthorhombic systems. The space group of **HT** belongs to *Pnma* (Supplementary Table S2). The molecule with a flat conformation (θ = 0.0(8)°) formed heterogeneous π-π stacking in a head-to-tailed manner (Figure 3B and Supplementary Figure S11). No homogeneous π-π stacking interactions were observed in **HT**, indicative of the absence of the offset regarding the stacking motif. All these results indicate that **LT**, **RT**, and **HT** crystal structures formed molecular stacking through the flat conformation of the molecules. However, the motif of these molecular stacking is different from one to another, which

could be the origin of its stimuli-responsivity.

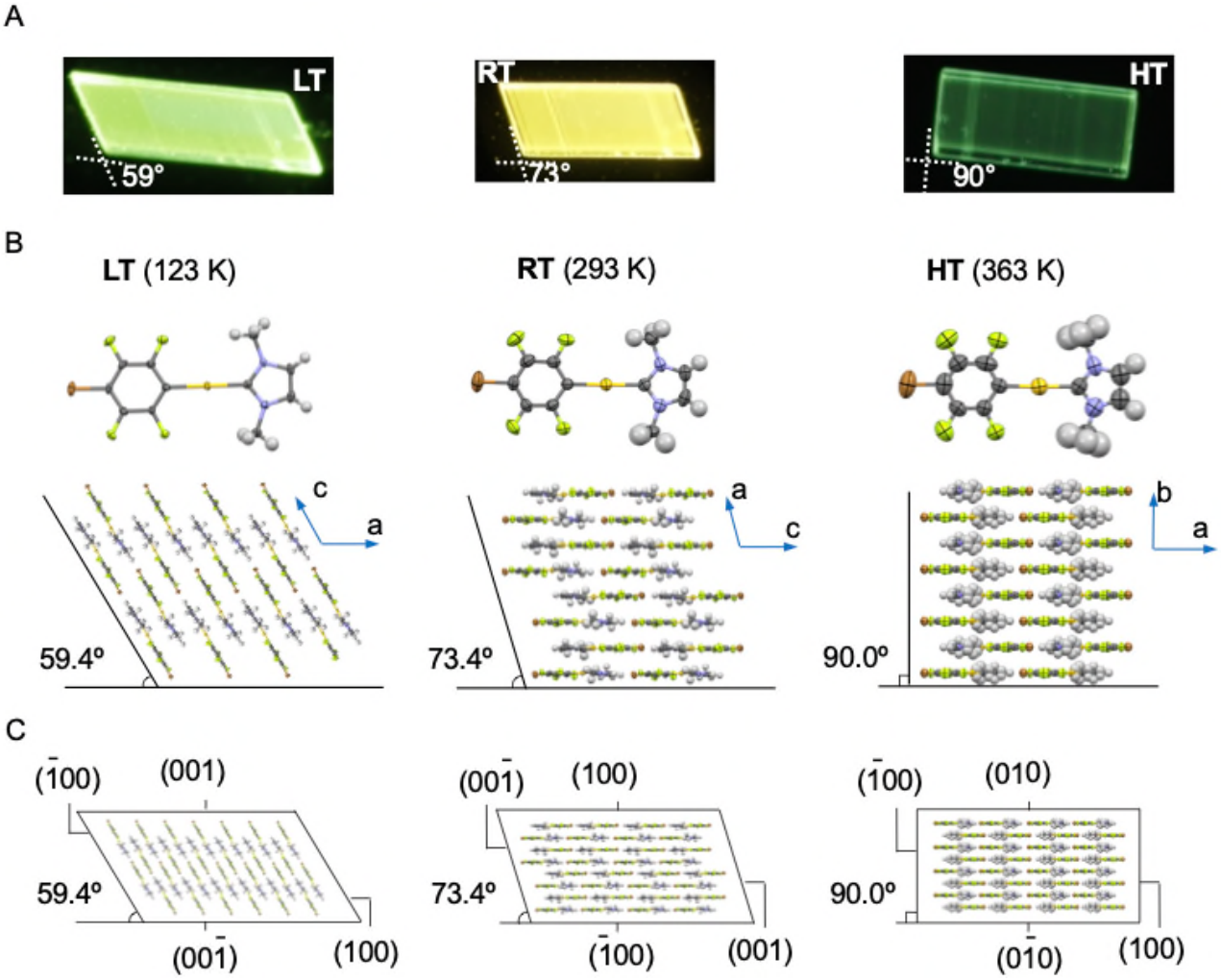

Figure 3. Microscopic structures and macroscopic morphologies among the three phases of crystal **1f.** A), Photographic image of **LT**, **RT**, and **HT** crystals under UV light. B), Molecular stacking of **LT**, **RT**, and **HT** crystal structures. C), Crystal packing with face indices.

Remarkably, the macroscopic corner angles of the crystals of **LT**, **RT**, and **HT** are associated with their microscopic offset angle of the molecular stacks. In the **LT** crystal structures, the molecules stack with a longitudinal displacement along molecular long axis (Figure. 3B). An overall offset angle of the molecular stacking of **LT** is 59.4°, which coincided with the corner angle of its macroscopic crystal of 59° (Figure 3 A, B). In **RT**, the overall offset angle of molecular stacking was also confirmed as 73.4°. The angle is in good agreement with its macroscopic corner angle of the crystal (73°) (Figure. 3 A,B). For **HT**, the molecules stack without longitudinal displacement along molecule long axis, producing the offset angle 90.0°, which is also coincided with the corner angle of its rectangular crystal (90º) (Figure 3 A,B). Moreover, the results of face indexing experiments again support the correspondence between their corner angles and offset angles (Figure 3C and Supplementary Figure S12). These detailed analyses of the crystal structures of **1f** clarified the origin of their macroscopic morphological alteration.

Mechanical properties of the **RT** crystal were investigated at room temperature. The **RT** crystal was mechanically bent upon applying shear stress to (100) face (Figure 4A, i,ii). The bent **RT** is referred to as ***b*-RT**. The bending angle of the ***b*-RT** is 32°, and the reproducibility of the bending angle was confirmed by repeated experiments (Supplementary Figure S13). Scanning electron microscopy (SEM) observation of the ***b*-RT** showed a clear bending interface at the boundaries between the bent and unbent moieties (Figure 4B and Supplementary Figure S14). Upon applying shear stress from the opposite direction, the bent moiety of **RT** was completely restored to its original parallelogram shape (Figure 4A, iii,iv). These reversible mechanical deformations are typical for ferroelastic molecular crystals we have reported previously for a structurally similar gold complex.[52]

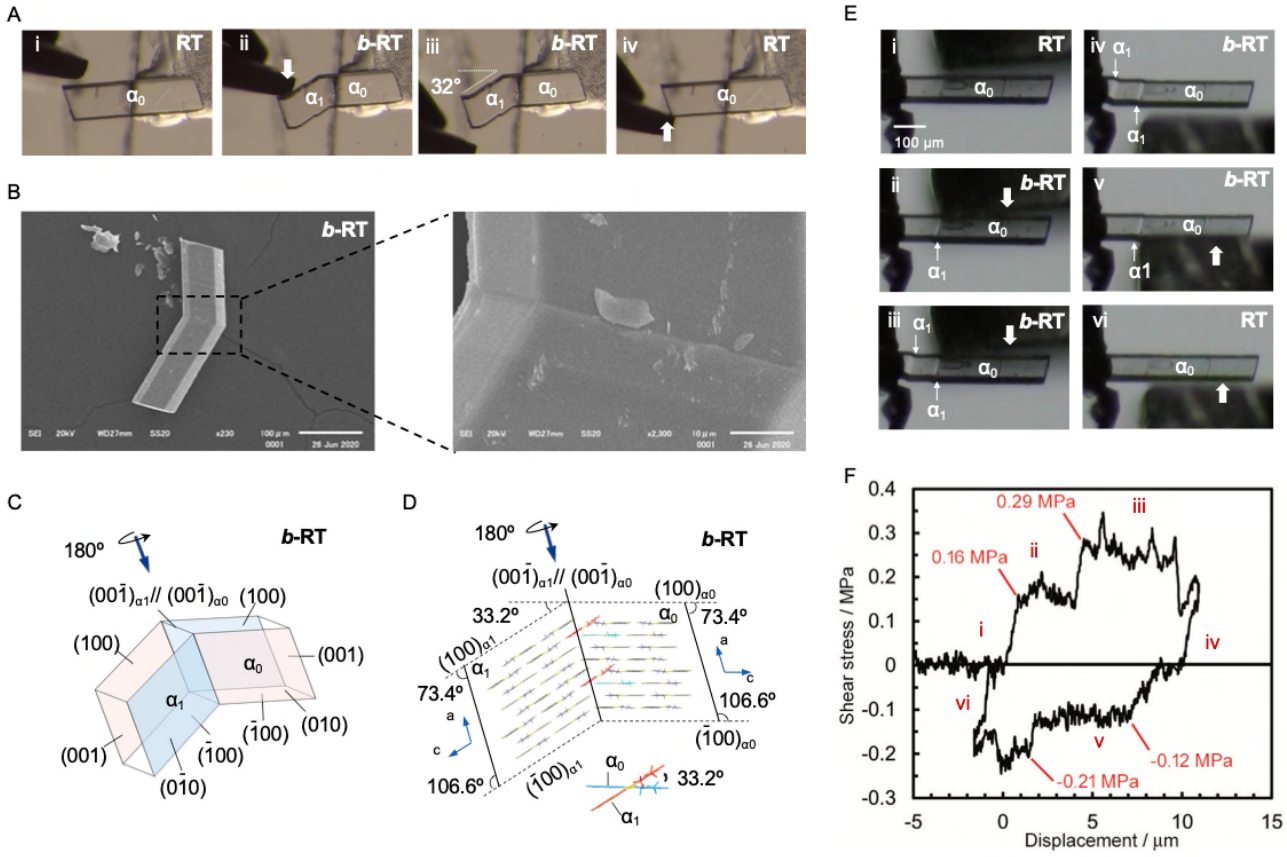

Figure 4. Mechanical-stress-induced twinning deformation of **RT**. A,B) Morphology visualized by optical microscopy (A) and SEM (B). A crystal **RT** was fixed on a base with epoxy glue. The **RT** bent manually by application of shear stress on the $(100)_{\alpha 0}$ face (A, i-ii) using tweezers. When shear stress is applied on the opposite face, the bent **RT** (***b*-RT**) was restored to its original shape (A, iii-iv). B) The SEM micrographs show the bending interface of ***b*-RT** that occurs during bending process. **c**, Crystal face indices of the ***b*-RT** determined by single-crystal X-ray diffraction. D) Crystal packing of ***b*-RT** viewed parallel to unbent domain $(010)_{\alpha 0}$ and bent domain $(0\text{–}10)_{\alpha 1}$. E) Snapshots of twinning deformation of **RT** crystal ($449 \times 63 \times 26\ \mu m^3$) upon application of shear stress: i–iii) forward direction and iv–vi) reverse direction. F) Ferroelastic hysteresis loops for twinning deformation of **RT**.

Single-crystal XRD analysis of the ***b*-RT** was performed at 293 K. For ***b*-RT**, the results demonstrate twinning deformation composed of the unbent domain (α_0) and the bent domain (α_1). This

indicates that the crystal structures of both α_0 and α_1 domains are the same but in different orientations. According to the crystal face indexing, the α_0 and α_1 domain were connected through the interface $(00–1)_{\alpha0}//(00–1)_{\alpha1}$ (Figure 4C). The lattices of the mother and daughter phase are related by a 180° rotation along the rotational axis (see the arrow in Figure 4C,D). The microscopic bending angle between α_0 and α_1 predicted from these twinning analyses is 33.2° (Figure 4D), which agreed well with the macroscopic bending angle (32°) confirmed by microscopic observation (Figure 4A). The packing diagram shows that a molecular rotation of 33.2° is required for retaining continuous boundaries during the deformation from α_0 to α_1 domain (Figure 4D). The XRD results demonstrate that macroscopic and microscopic changes occurred upon the twinning deformation from α_0 to α_1 domains.

The stress-strain relationship during ferroelastic deformation of the **RT** crystal was investigated at 303 K. Upon increasing the shear stress on the (100) plane of the **RT** crystal, the α_1 domain generated from the side of the jig at 0.16 MPa (Figure 4E,F, i-ii). Then, the α_1 domain started to grow upon further applying the shear stress, which remained relatively constant. The α_1 domain expands until another α_1 domain is generated with a shear stress of 0.29 MPa (iii). Then, the second α_1 domain started to expand upon almost constant stress. Moreover, upon applying shear stress from the opposite direction, a reversible deformation from α_1 to α_0 domain was proceeded (v,vi). The second α_1 domain began to contract after the stress increased to 0.12 MPa. After the second α_1 domain disappeared, the α_1 domain close to the jig started to contract at 0.21 MPa (v). Thereafter, the last α_1 domain disappeared and the bent shape of ***b*-RT** was restored to its original straight shape upon applying the reverse stress. The forward (0.16 MPa) and reverse (0.12 MPa) critical stress of **RT** are lower than those in our previous report (0.61 MPa and 0.49, respectively),[52] indicating that **RT** is superior in terms of absorbing weak mechanical shocks. The stress-strain measurement of the **RT** crystal demonstrates typical ferroelastic behavior including hysteresis behavior and the build-up of spontaneous strain.

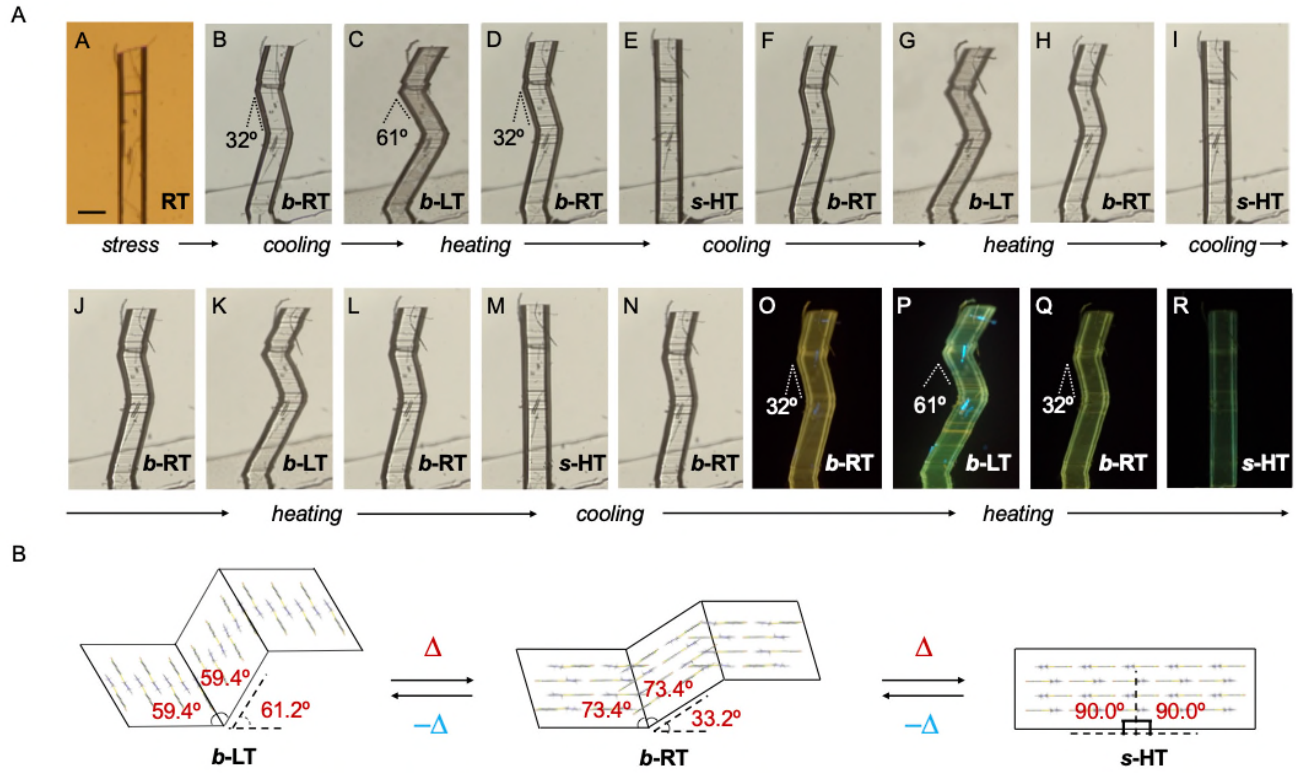

Figure 5. Multi-stage shape-changing effect and mechanism of crystal **1j**. A) Multi-stage shape-changing effect. A straight crystal of **RT** is mechanically bent (a–b). The bent **RT** (***b*-RT**) can be transformed into bent LT (***b*-LT**) and straight **HT** (***s*-HT**) upon cooling or heating, respectively (b–e). The bent shape of ***b*-LT**, ***b*-RT**, and ***s*-HT** were reproduced upon cooling/heating cycle, and the shape-changing effect was performed over four consecutive cooling/heating cycles (b–n under VIS light, o–r under UV light). **b**, Mechanism for shape-changing effect. Scale bar: 100 μm.

The multi-stage shape-changing effect of crystal **1j** was investigated. First, the bent shape was recorded in the pristine **RT** crystal by mechanical bending to make ***b*-RT** (Figure 5A). One end of the ***b*-RT** crystal was fixed on a base with epoxy glue for better observation. Upon cooling ***b*-RT** for the phase transition into **LT**, the bending angle starts to remarkably increase from 32° to 61° (photographs B–C in Figure 5A). The resulting bent **LT** is hereafter referred to as ***b*-LT**, showing a more enhanced zigzag shape of the crystal than ***b*-RT**. Upon reheating ***b*-LT** for the phase transition into ***b*-RT**, the bending angle is again changed from 61° to 32° at ~235 K (C–D). The observation indicates that the bent shape of ***b*-RT** was reproduced by heating. Upon further heating ***b*-RT** to ~330 K to obtain **HT**, we found the complete disappearance of the bent shape by the phase transition into the **HT** phase. The restored straight-shaped **HT** is called ***s*-HT** (E). Although **HT** (Figure 2) and ***s*-HT** (Figure 5) are almost the same in morphology and no obvious damage was found in ***s*-HT**, ***s*-HT** can reproduce the zig-zag shape. Remarkably, upon cooling ***s*-HT** to room temperature, the crystal bent again with an angle of 32° (F). This indicates that the recorded ***b*-RT** shape (F) recovered from ***s*-HT** (E) without applying additional mechanical stress. As mentioned above, **HT** can be obtained by heating pristine **RT** without bending shape (Figure 2). And the **HT** crystal did not lead to the crystal bending upon

cooling (Supplementary Figure S1 and S2). And the ***b*-LT** and ***s*-HT** shape also could be reproduced along with the temperature depending on phase transition. ***b*-LT** (G) and ***s*-HT** (I) shape were recovered upon cooling or heating, respectively. Of course, such morphology changes of bent crystals of **1f** upon cooling/heating accompanies with the emission color changes (O–R). And the reproducibility of the reversible multi-stage shape changing effect was confirmed (Figure S18 and S19). The results of the observation indicate that pristine crystal of **1f** could reproduce three different shapes: ***b*-LT**, ***b*-RT**, and ***s*-HT**. The three different shapes undergo a reversible multi-stage shape-changing effect upon cooling/heating cycle.

Detailed XRED analysis can explain the mechanism of the recording and shape reproduction of the shape-changing effect. Similar to ***b*-RT**, the observed bending angles of ***b*-LT** and **HT** can be reasonably understood by the results of XRD analyses. Then, XRD analyses of the ***b*-LT** were performed at 123 K. We found that the crystal structure of ***b*-LT** shows twinning (Supplementary Table 3). Both α_0 and α_1 domains have identical crystal structures with the **LT** crystal. The XRD analysis of ***b*-LT** with face indexing indicated that the interface between the α_0 and α_1 domain is $(10–1)_{\alpha0}$//$(10–1)_{\alpha1}$ (Supplementary Figure 20). The lattices of α_1 domain forms by a 180° rotation about the rotational axis, which is an arrow parallel to the twinning interface (–101). Based on the XRD analysis of ***b*-LT**, the microscopic bending angle is estimated to be 61.2°, which coincided with the macroscopic bending angle of 61° confirmed by microscopy observation (Figure 5 and Supplementary Figure 14). For the ***s*-HT**, the XRD results indicate that the twinning was not confirmed and can be modeled as the single component (Supplementary Table 3 and Supplementary Figure S21). Because the offset angle of the molecular stack of ***s*-HT** is 90.0°, the microscopic bending angle is estimated to be 0°. This makes the **s-HT** a straight and the zigzag shape by the twinning in ***b*-RT** and ***b*-LT** appeared to disappear. (Figure 5). As mentioned above, we observed that ***b*-RT** shows bending interfaces at the boundaries between the bent and unbent moieties by SEM (Figure 4B). The trace of the bending interfaces remained even after ***b*-RT** transformed into ***s*-HT** (Supplementary Figure S22). Although the interface seems to be disappeared in optical observation, the remaining post-bending interface in the ***s*-HT** would be important to the recovery of ***b*-RT** shape. In contrast, the **HT**, which transformed from an unbent **RT**, showed a clear surface, and the traces that were found on ***s*-HT** surface was not observed by SEM (Supplementary Figure S23). And upon cooling the **HT** to room temperature, the crystal does not bend (Supplementary Figure S2). The macroscopic bending angles of ***b*-LT**, ***b*-RT**, and ***s*-HT** can be reasonably understood when considering their crystal structures. The key to the present reversible multi-stage shape-changing effect in the crystal of complex **1f** is that **1f** shows both multiple temperature-dependent phase changes (**HT**, **RT**, and **LT**) and mechanical deformation with ferroelasticity (Figure 6). Moreover, crystals of **1f** show simultaneously changes in morphology and luminescence color in response to temperature changes. The crystal of **1f** can be mechanically bent by application of stress at room temperature (**RT**), and subsequently undergo a reversible multi-stage shape-changing effect upon cooling/heating (***s*-HT**, ***b*-RT**, and ***b*-LT**).

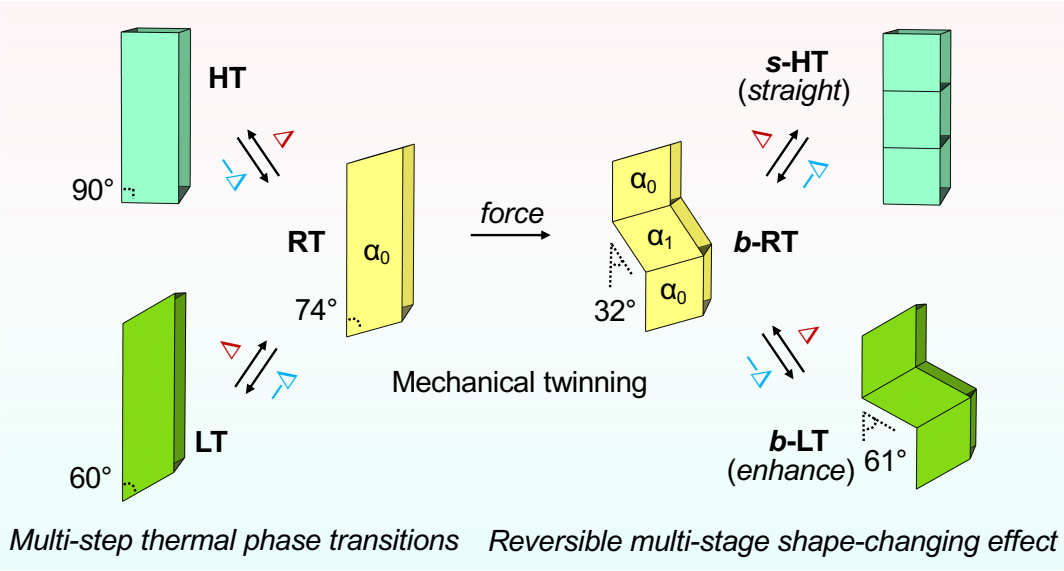

Figure 6. Schematic illustration of the reversible multi-stage shape-changing effect.

3.3. Conclusions

I have reported a reversible multi-stage shape-changing material based on an arylgold(I)(*N*-heterocyclic carbene) (NHC) complex (**1f**) that is characterized by the reproduction of three different shapes and luminescence-color changes (Figure 6). The reversible multi-stage shape-changing effect was achieved by a combined twinning deformation and multi-step thermal phase transitions. The twinning deformation causes the lattice rotation of the **RT** crystal, resulting in a zigzag shape (***b*-RT**) with different orientations of the crystal structures. By applying mechanical bending at the **RT**, the direction of the crystal structure can be memorized. Intriguingly, the conversion of three different shapes accompanied by luminescent color changes. I believe that the discovery of shape-changing material of crystal **1f** provides novel strategies for imparting further functions to the known shape memory materials.

3.4. Experimental details

3.4.1. General

All commercially available reagents and solvents are of reagent grade and were used without further purification unless otherwise noted. Solvents for the synthesis were purchased from commercial suppliers, degassed by three freeze-pump-thaw cycles and further dried over molecular sieves (4 Å). NMR spectra were recorded on a JEOL JNM-ECX400P or JNM-ECS400 spectrometer (^{1}H: 392 MHz; ^{13}C: 98.5 MHz) using tetramethylsilane and $CDCl_3$ as internal standards, respectively. Emission spectra were measured by using an Olympus fluorescence microscope BX51 equipped with Hamamatsu photonics multichannel analyzer PM-12. The absorption spectra of the solid samples were recorded on a JASCO V-660 UV-VIS spectrophotometer. The emission quantum yields of the solid samples were recorded on a Hamamatsu Quantaurus-QY spectrometer with an integrating sphere. Emission lifetime measurements were recorded on a Hamamatsu Quantaurus-Tau spectrometer. Elemental analyses and high-resolution mass spectra were recorded at Global Facility Center, Creative Research Institution, Hokkaido University. Photographs were obtained using Olympus BX51 or SZX7 microscopes with Olympus DP72, or Sony $\alpha7_{SII}$ digital cameras. Scanning electron microscopic images were acquired by using JEOL JSM-6510LV. Stress-strain tests were carried out on a universal testing machine (Tensilon RTG-1210, A&D Co. Ltd.). Differential Scanning Calorimetry (DSC) profiles were measured on DSC Q2000 V24.11.

X-ray diffraction analyses: Single crystal X-ray structural analyses were carried out on a Rigaku XtaLAB PRO MM007 diffractometer using graphite monochromated Mo-K_α radiation. The structure was solved by direct methods and expanded using Fourier techniques. Non-hydrogen atoms were refined anisotropically. Hydrogen atoms were refined using the riding model. All calculations were performed using the Olex2 crystallographic software package except for refinement, which was performed using SHELXT-2018.[67] The structures were solved by direct methods with (SHELXT)[67] and refined by full-matrix least-squares techniques against F2 (SHELXL-2018/3)[68] by using Olex2 software package.

3.4.2. Synthesis of 1j

Scheme for the synthesis of **1j.**

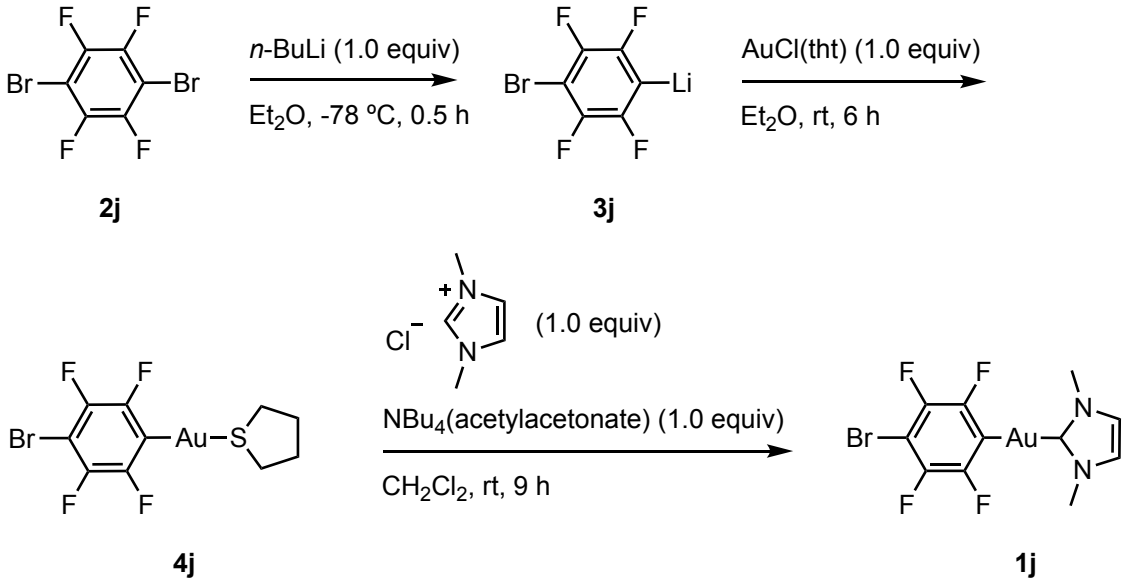

*Synthesis of 1-bromo-2,3,5,6-tetrafluorobenzenyl(1,3-dimethylimidazolin-2-ylidene)gold complex **1j.***

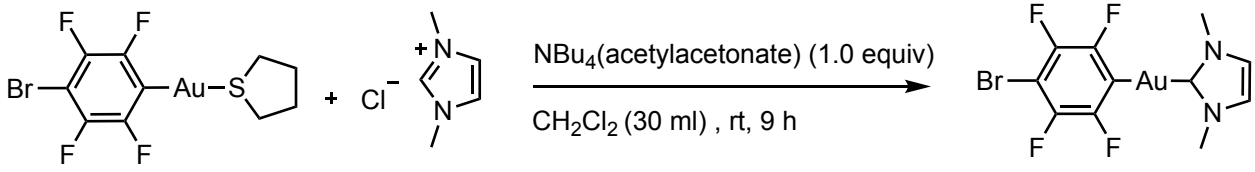

Compound **1j** was prepared by the modification of the literature method.[69] An oven-dried two-neck flask was connected to a vacuum/nitrogen manifold through a rubber tube. It was evacuated and then backfilled with nitrogen. This cycle was repeated three times. In this flask, **4j**[70] (297 mg, 0.58 mmol) and **5j** (77 mg, 0.58 mmol) were dissolved in CH_2Cl_2 (30 ml) and stirred until a colorless solution formed (5 min). Then, NBu_4(acetylacetonate)[69] (198 mg, 0.58 mmol) was added and stirred for 9 h at room temperature. The reaction mixture was directly filtered through a plug of silica and the colorless filtrate was evaporated to minimum volume. Hexane was added to the residue to form a white solid which was collected through the filtration and vacuum dried to give the analytically pure product **1j** (118 mg, 0.23 mmol, 40%). ^{1}H NMR (392 MHz, $CDCl_3$, δ): 3.91 (s, 6H, Me), 6.94 (s, 2*H*, imidazole). ^{13}C NMR (98.5 MHz, $CDCl_3$, δ): 37.75 (s, Me), 94.30–94.77 (m, Br-*C*), 121.71 (s, *C*H, imidazole), 140.51–141.69 (m, Au-*C*-C), 142.90–145.73 (m, F-*C*), 148.49–151.19 (m, F-*C*), 188.74 (s, N-*C*-N). ESI-MS (*m*/*z*): $[M+Na]^+$ calcd for $C_{11}H_8AuBrF_4N_2Na$, 542.93702; found, 542.93697.

3.4.3. Preparation and images of the single crystals of 1j

*Preparation of the single crystal of **1j***:

The single crystal of **1j** was obtained by liquid-liquid diffusion. Typically, **1j** (50 mg) is dissolved in 2 mL of CH_2Cl_2 in a vial and hexane (6 mL) was carefully layered. After standing for 1 days at room temperature, the colorless single crystals of **1j** were formed.

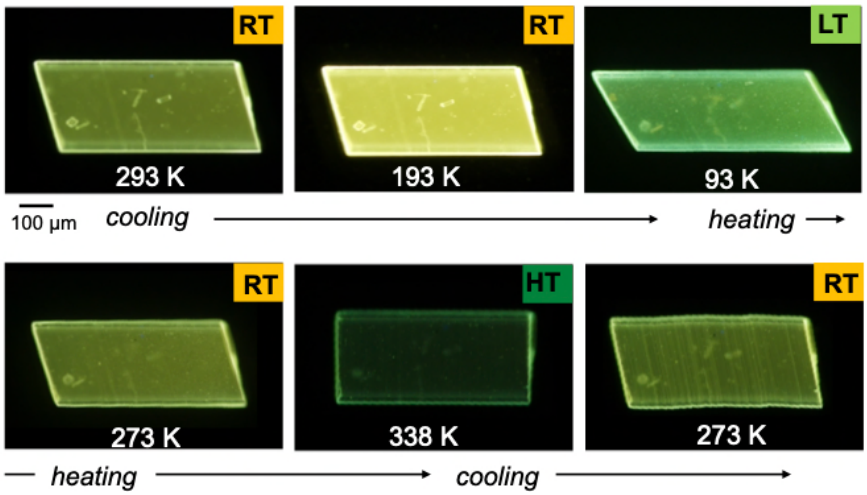

Figure S1. Photographs of a crystal of **1j** observed upon cooling/heating at 20 K min^{-1} under UV light.

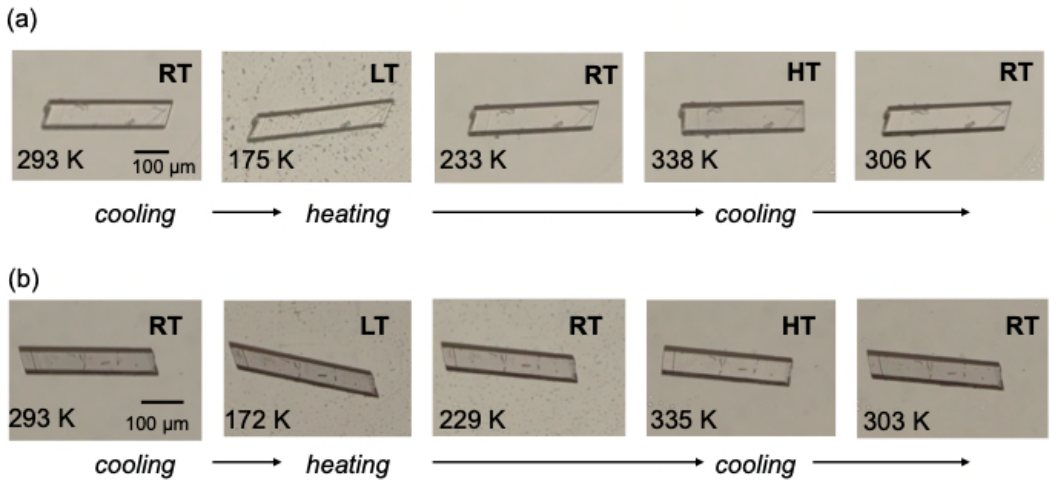

Figure S2. Photographs of a crystal of **1j** observed upon cooling/heating at 20 K min^{-1} under room light.

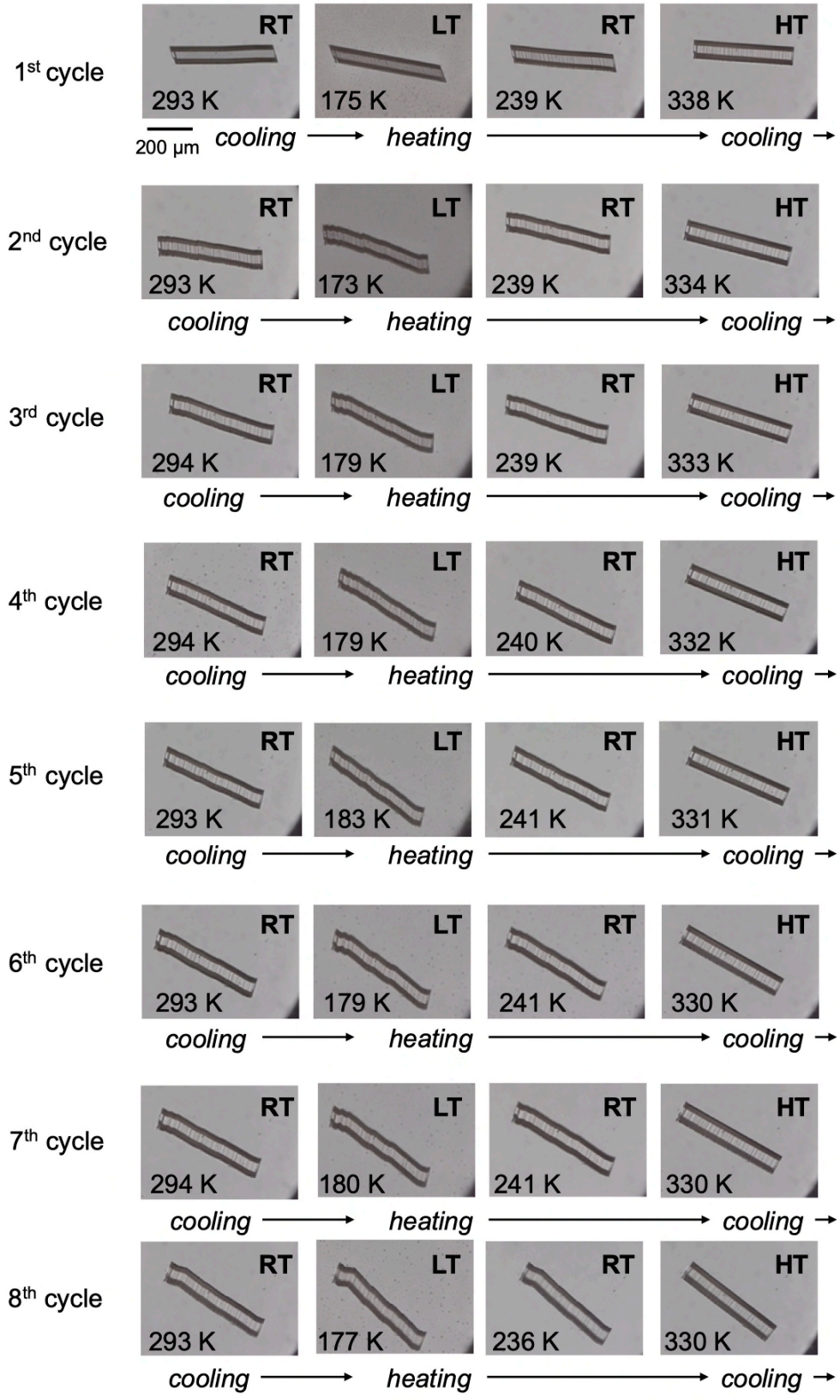
1st cycle
RT
293 K
LT
175 K
RT
239 K
HT
338 K
200 µm
cooling
heating
cooling
2nd cycle
RT
293 K
LT
173 K
RT
239 K
HT
334 K
cooling
heating
cooling
3rd cycle
RT
294 K
LT
179 K
RT
239 K
HT
333 K
cooling
heating
cooling
4th cycle
RT
294 K
LT
179 K
RT
240 K
HT
332 K
cooling
heating
cooling
5th cycle
RT
293 K
LT
183 K
RT
241 K
HT
331 K
cooling
heating
cooling
6th cycle
RT
293 K
LT
179 K
RT
241 K
HT
330 K
cooling
heating
cooling
7th cycle
RT
294 K
LT
180 K
RT
241 K
HT
330 K
cooling
heating
cooling
8th cycle
RT
293 K
LT
177 K
RT
236 K
HT
330 K
cooling
heating
cooling

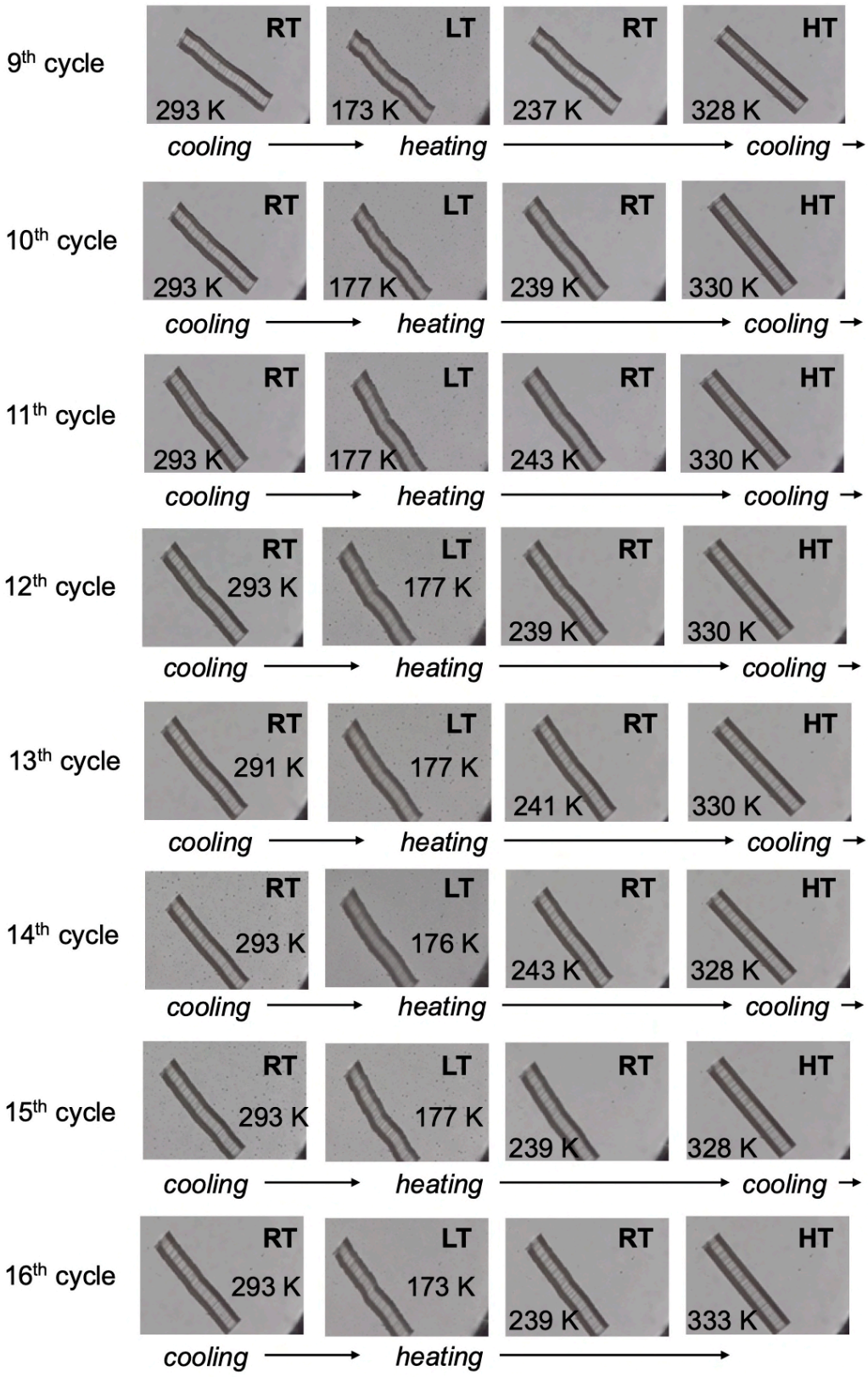

Figure S3. Photographs of crystal **1j** observed under room light upon heating/cooling at 20 K min^{-1}.

3.4.4. Differential scanning calorimetry profiles of 1j

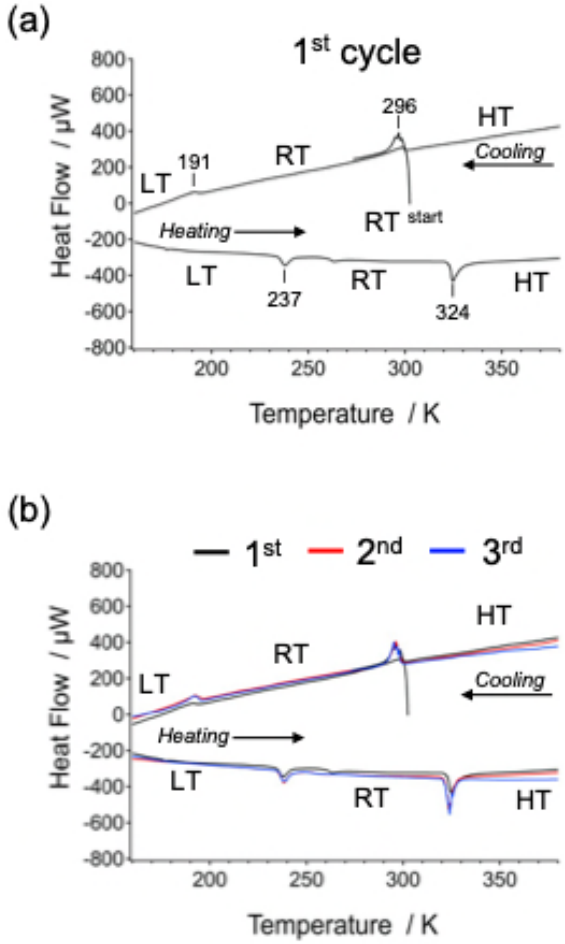

Fig. S4. (a) DSC profile recorded by heating and cooling of crystals **1j**. (b) Comparison of the DSC profiles for 1st, 2nd, and 3rd measurements using the same specimen of **1j**. The heating and cooling rates in all experiments were 5 K min^{-1}.

3.4.5. Optical properties of LT, RT, and HT

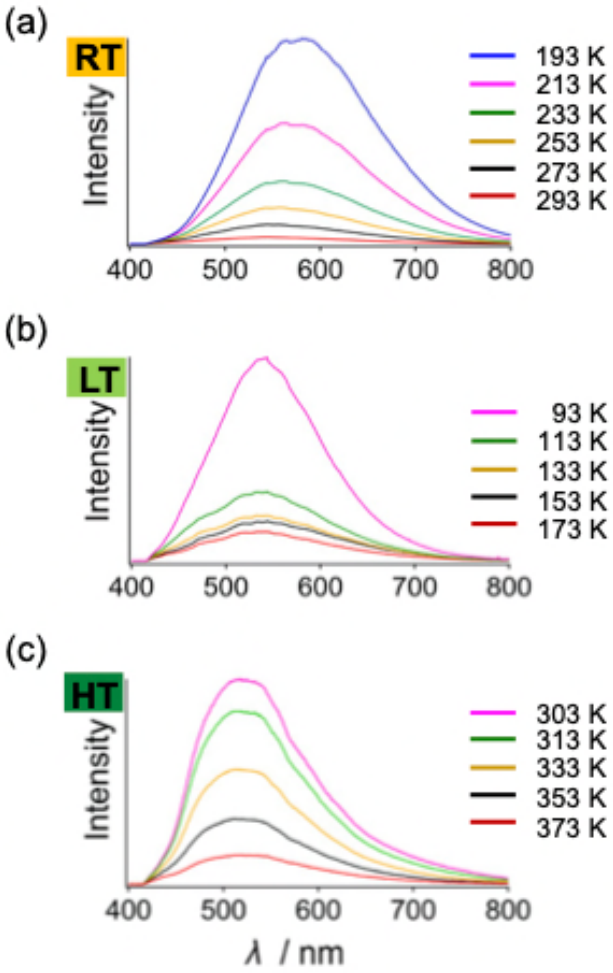

Figure S5. Temperature-dependent photoluminescence spectra of (a) **RT** crystal recorded from 193 to 293 K, (b) **LT** crystal recorded from 93 to 173 K, and (c) **HT** crystal recorded from 303 to 373 K.

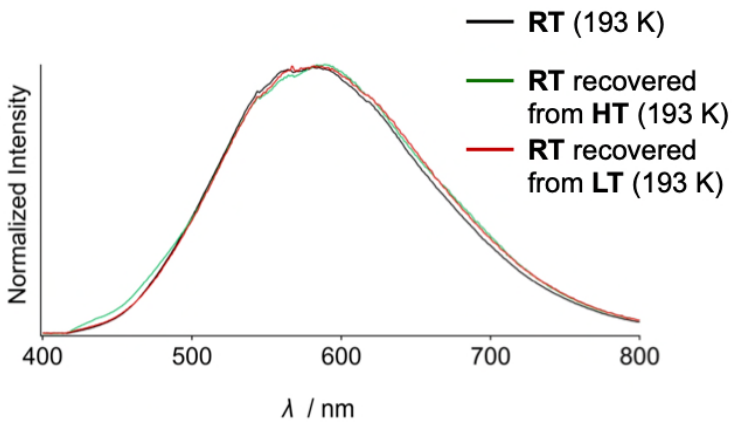

Figure S6. Photoluminescence spectra of **RT** crystal recovered from **HT** and **LT** crystal (λ_{ex} = 365 nm).

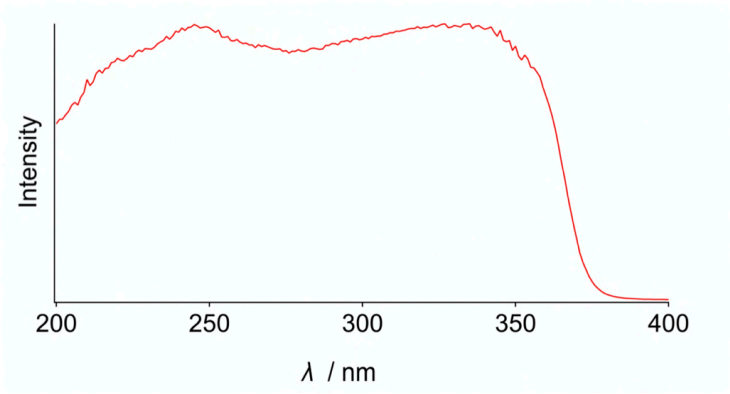

Figure S7. Absorption spectrum of **RT** crystals at room temperature.

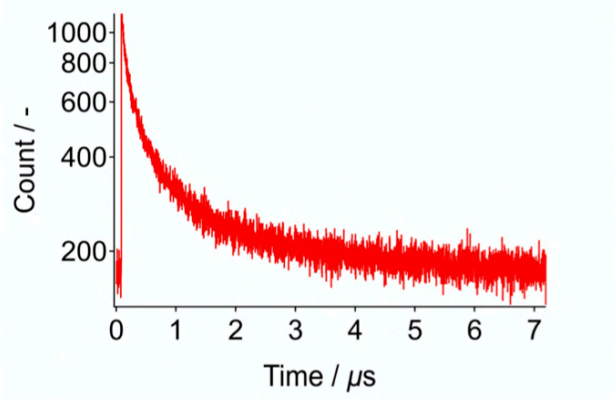

Figure S8. Emission decay profile of **RT** (λ_{em} = 575 nm) under excitation at 371 nm.

Table S1. Photophysical properties of **RT** at room temperature.

	Φ_{em} / - (λ_{ex} / nm)	τ_{av} / μs[a,b] (λ_{em} / nm)	τ_1 / μs (A / -)	τ_2 / μs (A / -)	τ_3 / μs (A / -)
RT	0.007 (358)	2.05 (575)	0.46 (0.16)	0.09 (0.03)	2.43 (0.81)

[a]λ_{ex} = 371 nm. [b]$\tau_{av} = \Sigma \tau_n A_n$.

3.4.6. Single-crystal XRD structure analyses of LT, RT, and HT

Table S2. X-ray crystallographic data for **LT**, **RT**, and **HT**

compound	**LT**	**RT**	**HT**
CCDC Number	2081347	2081348	2081349
Empirical Formula	$C_{11}H_8AuBrF_4N_2$	$C_{11}H_8AuBrF_4N_2$	$C_{11}H_8AuBrF_4N_2$
Formula Weight	521.07	521.07	512.07
Crystal Size / mm	0.27×0.19×0.04	0.27×0.19×0.04	0.27×0.19×0.04
Crystal System	monoclinic	monoclinic	orthorhombic
a / Å	7.6850(3)	14.0862(6)	12.9752(7)
b / Å	15.3186(4)	15.4831(7)	6.8244(4)
c / Å	12.9425(5)	12.9171(5)	15.5938(10)
α / °	90	90	90
β / °	120.622(5)	106.586(4)	90
γ / °	90	90	90
V / Å^3	1311.16(10)	2700.0(2)	1380.80(14)
Space Group	$P2_1/c$	$P2_1/c$	$Pnma$
Z value	4	8	4
D_{calc} / g cm^{-3}	2.640	2.564	2.507
Temperature / K	123	293	363
$2\theta_{max}$ / °	58.822	58.898	58.486
μ / cm^{-1}	143.01 (Mo K$_\alpha$)	138.90 (Mo K$_\alpha$)	135.80 (Mo K$_\alpha$)
No. of Reflections	Total: 12804 Unique: 3100 R_{int}: 0.0382	Total: 35621 Unique: 6648 R_{int}: 0.0309	Total: 12492 Unique: 1812 (R_{int}: 0.0509)
R_1[a]; wR_2[b]	0.0212; 0.0523	0.0422; 0.1190	0.0387; 0.1187
GOF[c]	1.030	1.061	1.058
Max./Min. peak I[d] / Å^3	1.48 e$^-$/−1.15 e$^-$	3.11 e$^-$/−1.61 e$^-$	1.71 e$^-$/−1.49 e$^-$

[a]: For data with $I > 2.00\sigma(I)$. [b]: For all reflection data. [c]: Goodness of Fit.

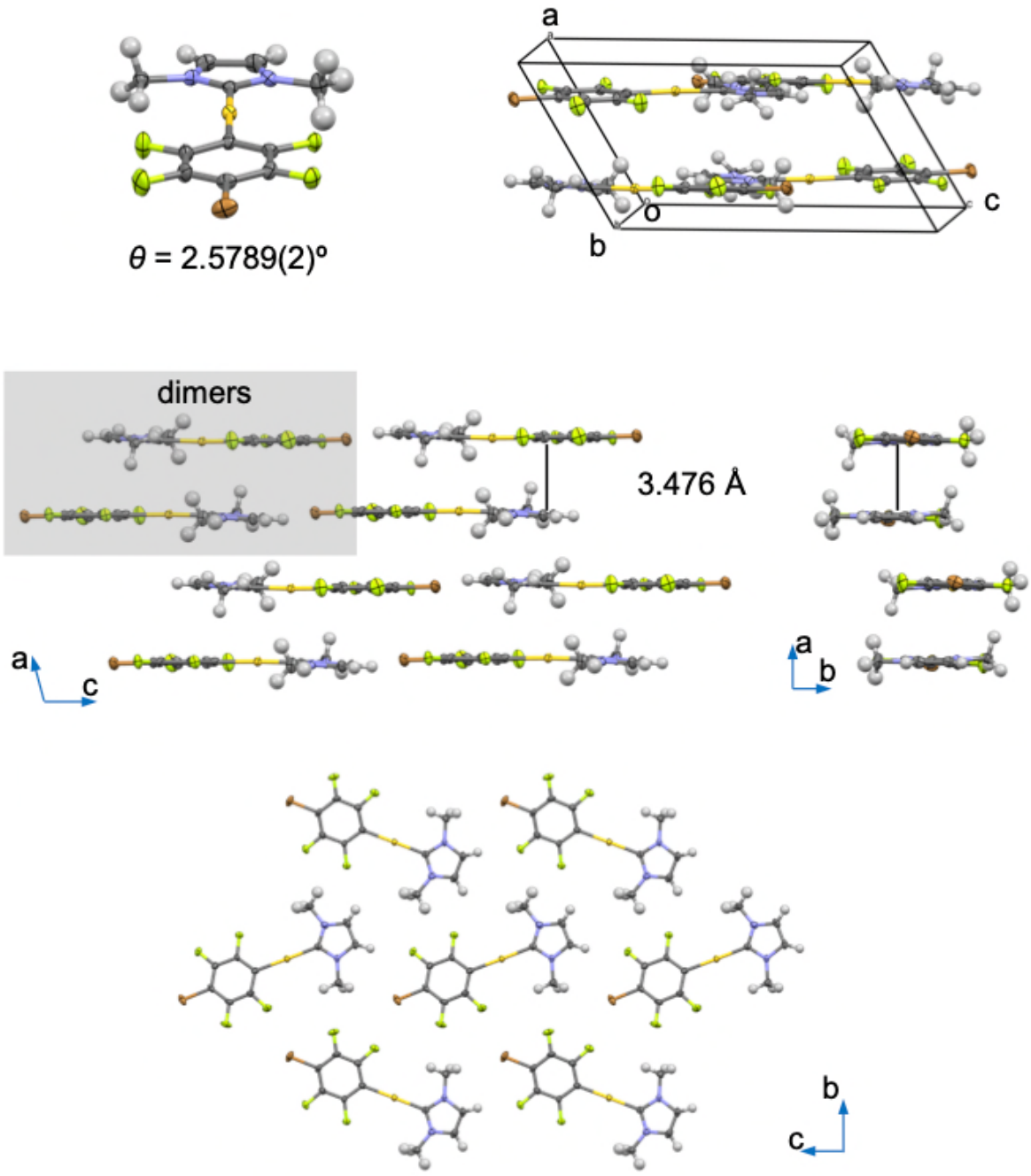

Figure. S9. Single-crystal structure of **LT** at 123 K.

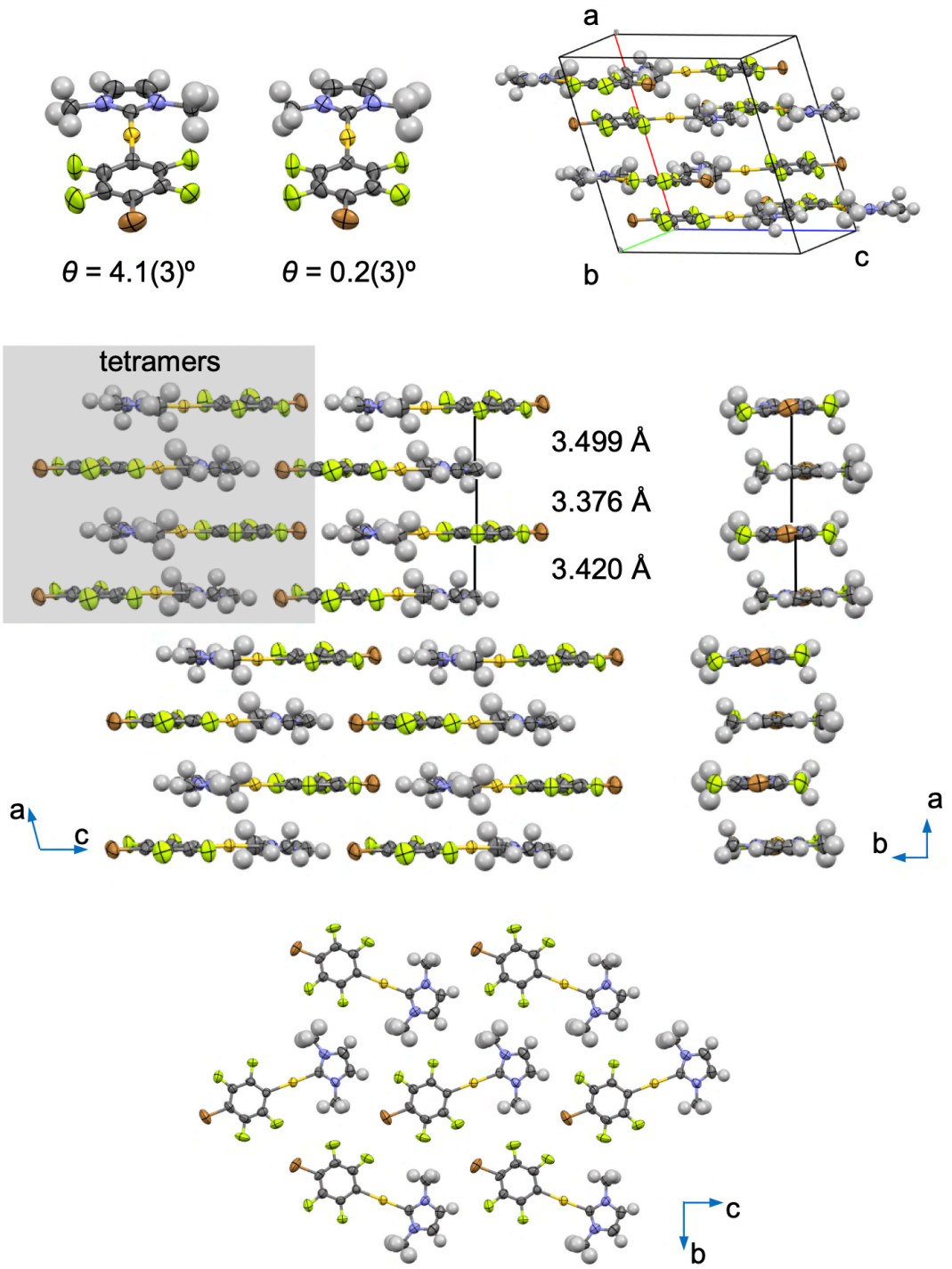

Figure S10. Single-crystal structure of **RT** at 293 K.

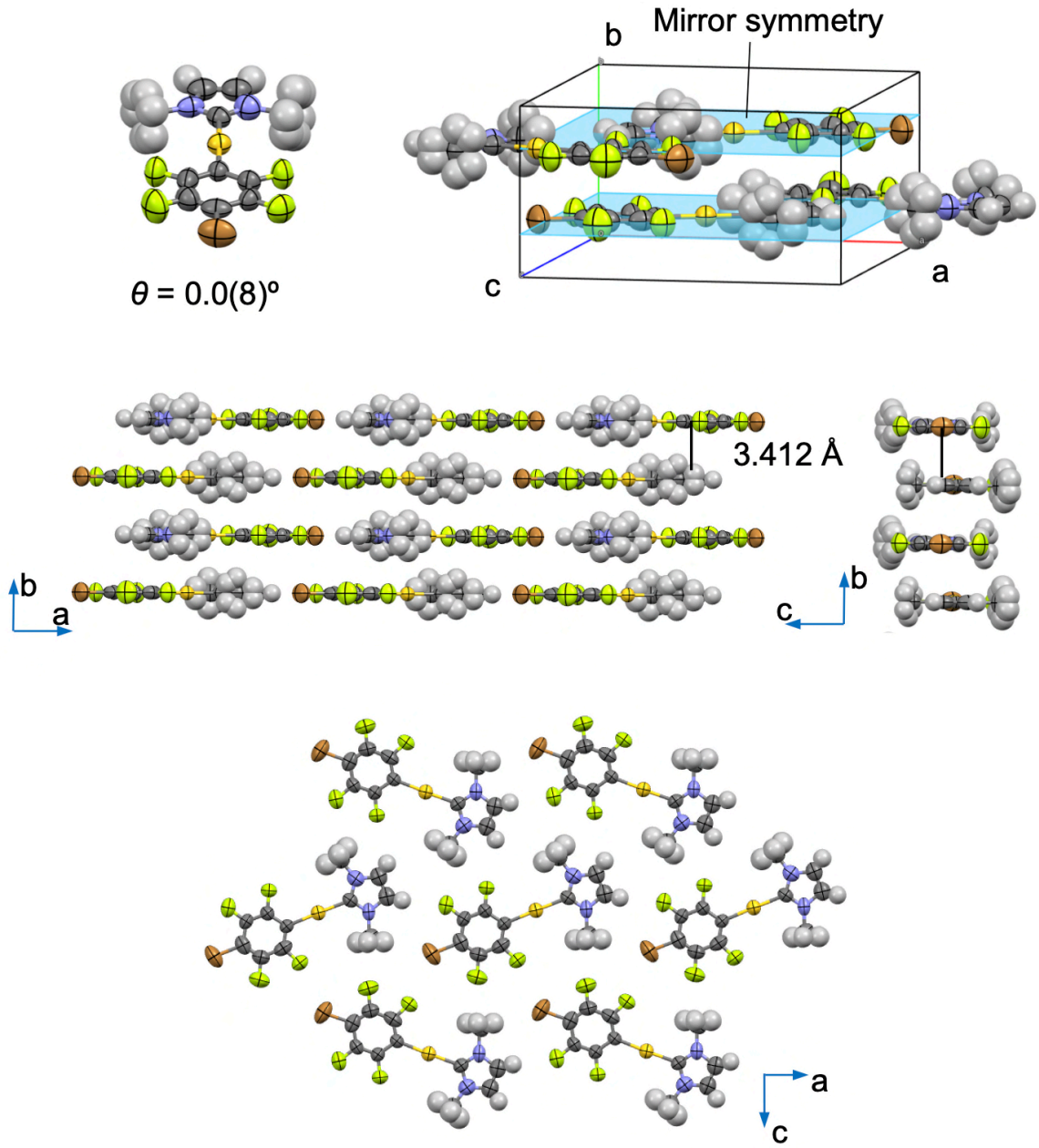

Figure S11. Single-crystal structure of **HT** at 363 K. The modeled structure of the hydrogen looks rather complicated because the center of the molecule of **1j** sits on the mirror plane.

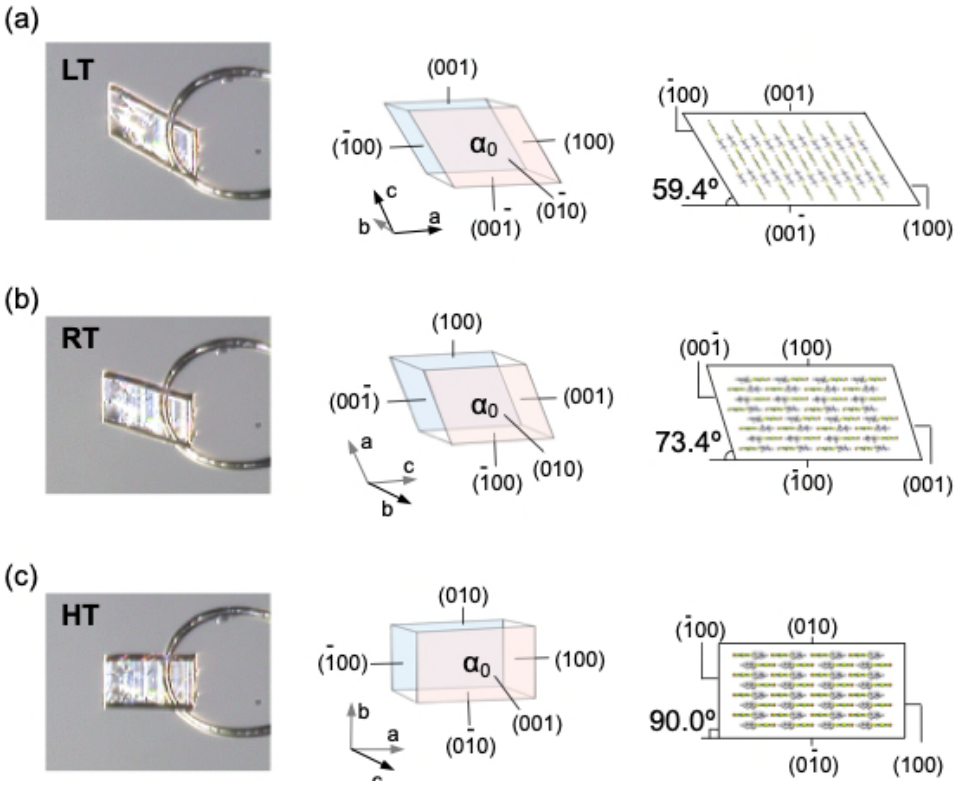

Figure S12. Optical image and crystal packing with face indices of (a) the **LT** crystal at 123 K, (b) the **RT** crystal at 293 K, and (c) the **HT** crystal at 363 K.

3.4.7. Images and single-crystal XRD structure analyses of *b*-LT, *b*-RT, and *s*-HT

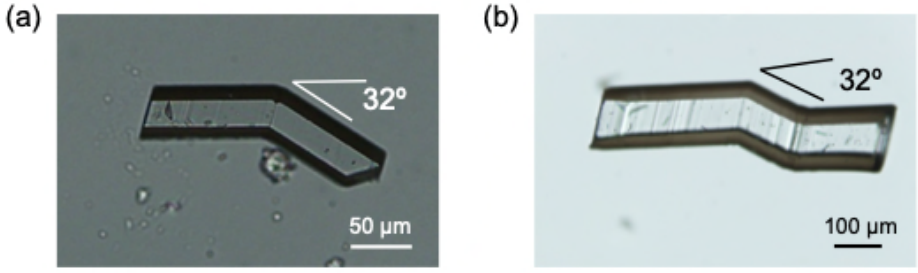

Figure S13. Photographic images of ***b*-RT**.

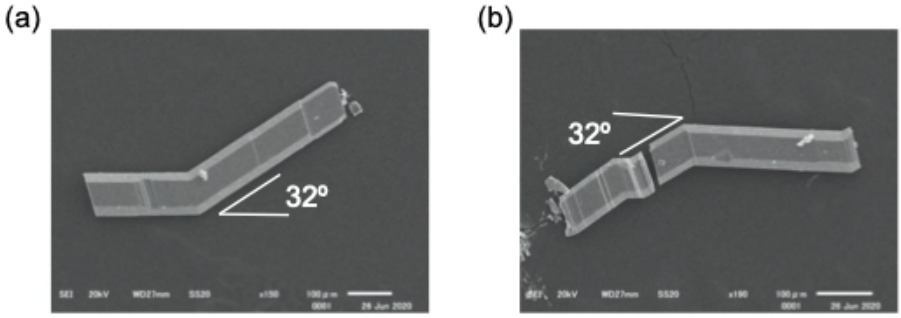

Figure S14. SEM images of ***b*-RT**.

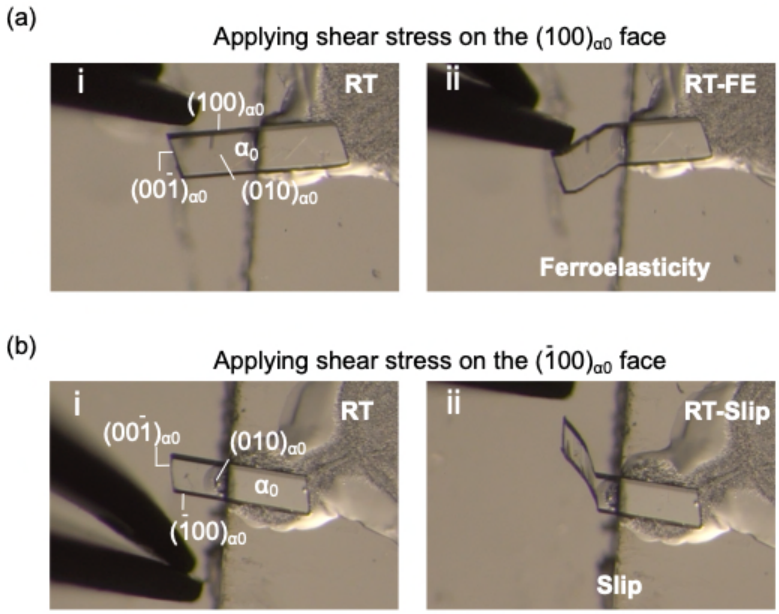

Figure S15. Photographic images of deformed **RT**. The mechanical properties of the **RT** crystal were investigated by applying shear stress at the $(100)_{\alpha 0}$ face and $(-100)_{\alpha 0}$ face, which showed (a) ferroelastic and (b) slip deformation, respectively.

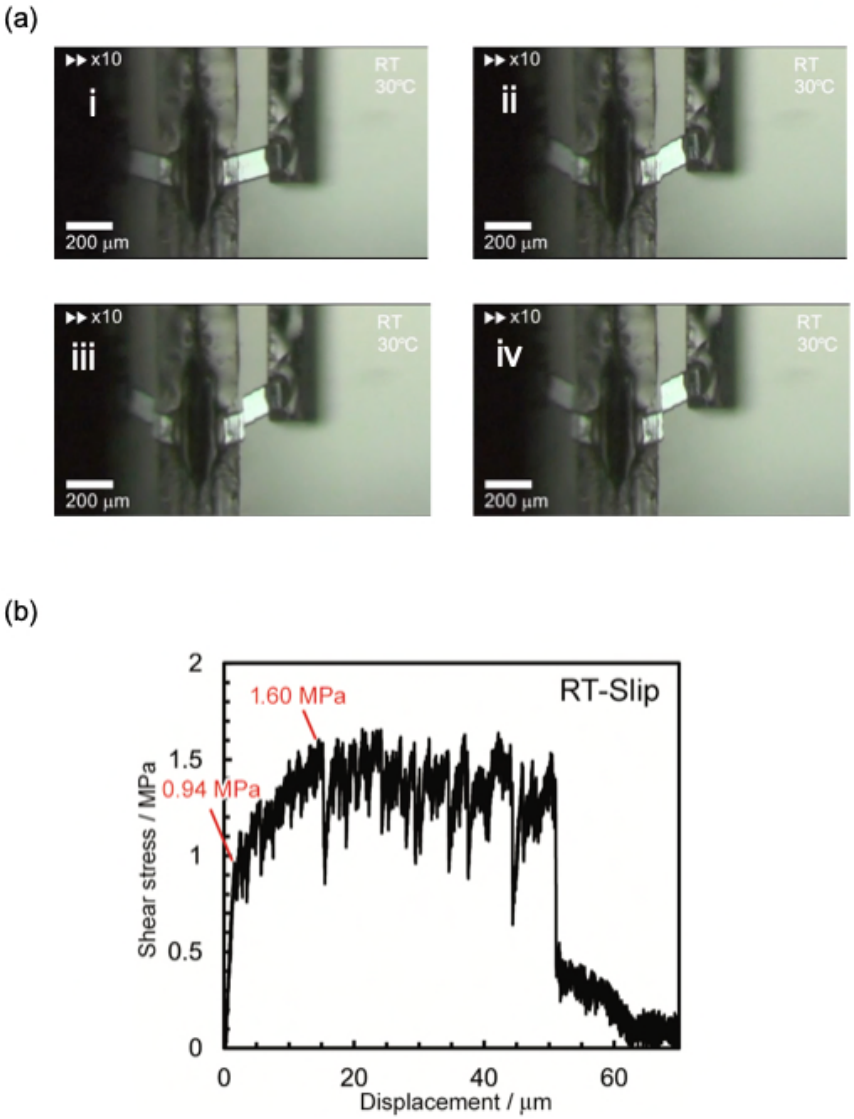

Figure S16. (a) Snapshots of slip deformation of **RT** upon application of shear stress under visible light at 30 ºC. (b) Stress-displacement result of the crystal under VIS light.

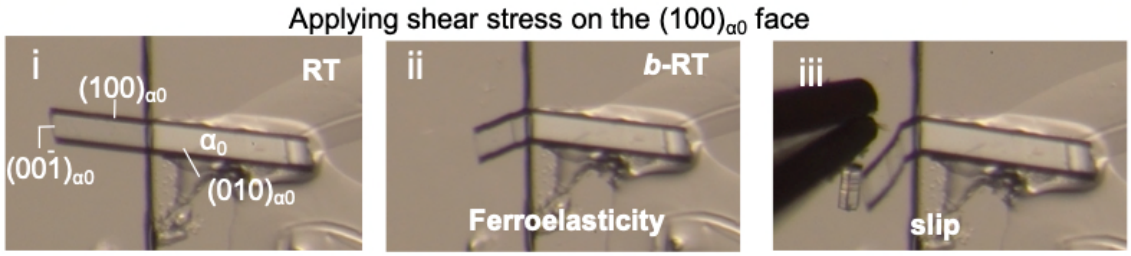

Figure S17. Photographic images of a deformed **RT** crystal upon applying shear stress on the $(100)_{\alpha 0}$ face.

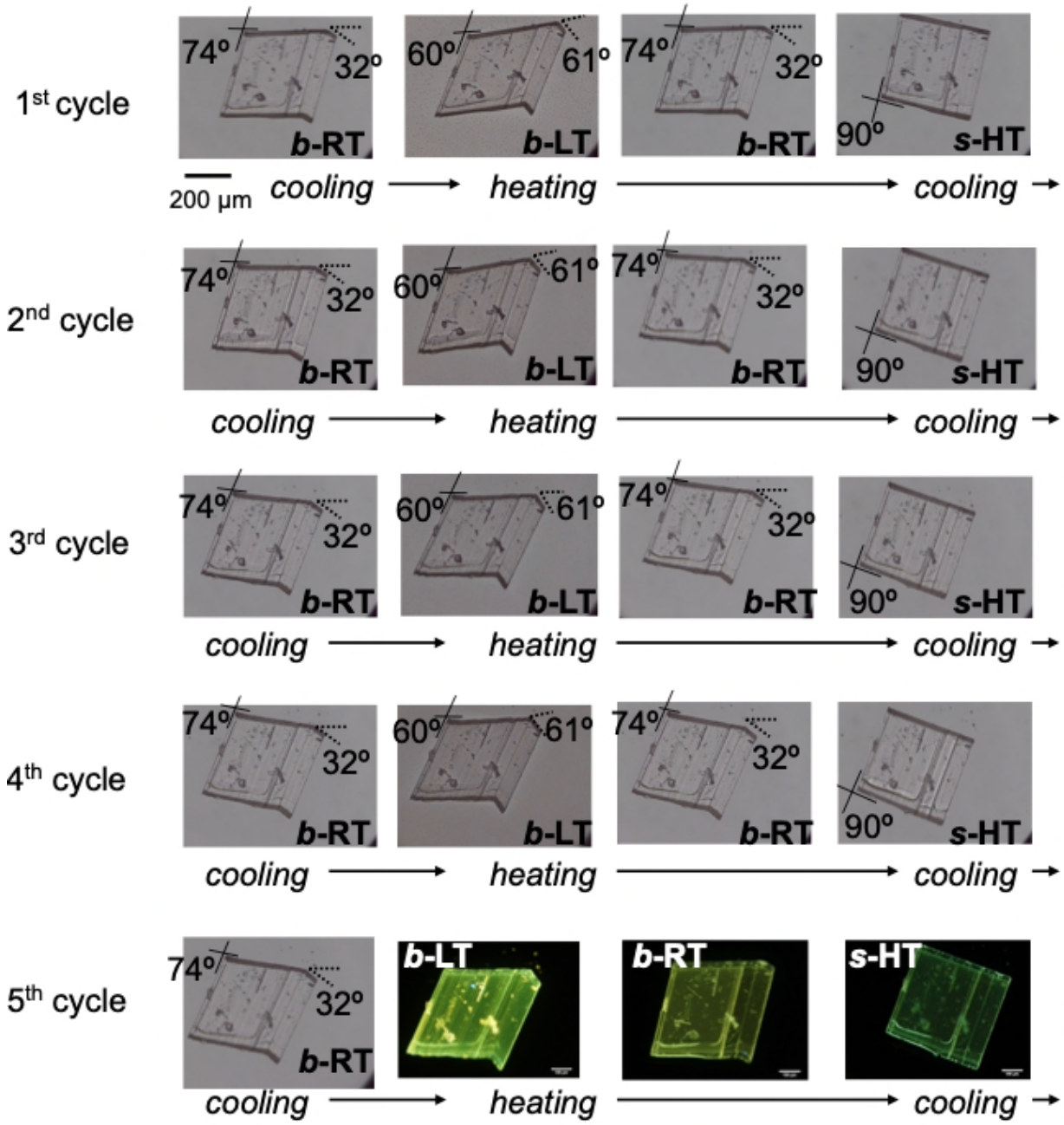

Figure S18. Photographic images of reversible multi-stage shape-changing effect of ***b*-RT** upon heating/cooling at 20 K min^{-1}.

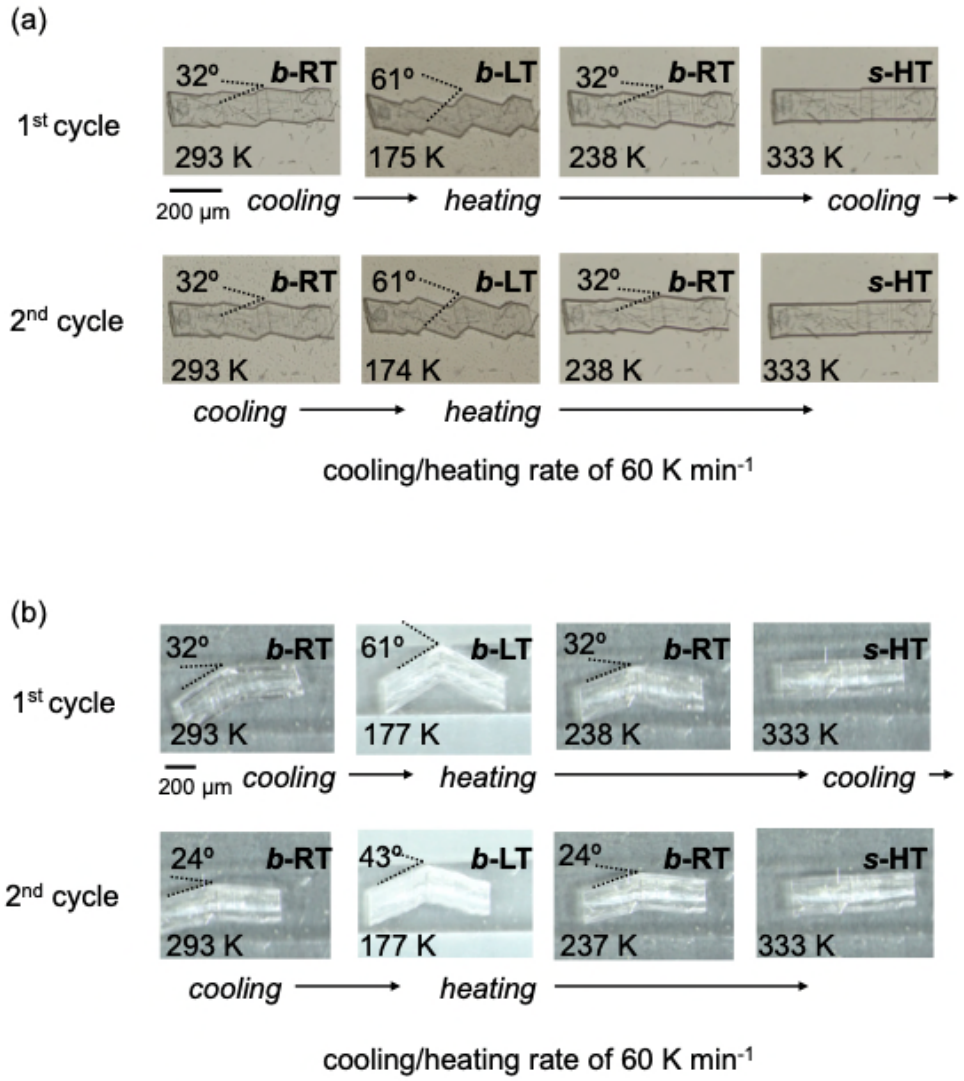

Figure S19. Photographic images of reversible multi-stage shape-changing effect of ***b*-RT** upon heating/cooling at 60 K min^{-1}.

Table S3 X-ray crystallographic data for ***b*-LT**, ***b*-RT**, and ***s*-HT**

compound	***b*-LT**	***b*-RT**	***s*-HT**
CCDC Number	2081350	2081351	2081352
Empirical Formula	$C_{11}H_8AuBrF_4N_2$	$C_{11}H_8AuBrF_4N_2$	$C_{11}H_8AuBrF_4N_2$
Formula Weight	521.07	521.07	512.07
Crystal Size / mm	0.35×0.25×0.06	0.40×0.15×0.07	0.40×0.15×0.07
Crystal System	monoclinic	monoclinic	orthorhombic
a / Å	7.6985(5)	14.0976(5)	12.9715(6)
b / Å	15.3528(8)	15.4992(5)	6.8326(3)
c / Å	12.9738(8)	12.9484(4)	15.6063(8)
α / °	90	90	90
β / °	120.533(9)	106.584(4)	90
γ / °	90	90	90
V / Å^3	1320.79(17)	2711.55(16)	1383.17(11)
Space Group	$P2_1/c$	$P2_1/c$	Pnma
Z value	4	8	4
D_{calc} / g cm^{-3}	2.620	2.553	2.502
Temperature / K	123	293	363
$2\theta_{max}$ / °	56.752	59.006	58.126
μ / cm^{-1}	141.79 (Mo K$_\alpha$)	138.30 (Mo K$_\alpha$)	135.80 (Mo K$_\alpha$)
No. of Reflections	Total: 5301 Unique: *N*/*A*[a] (R_{int}: *N*/*A*[a])	Total: 12298 Unique: *N*/*A*[a] (R_{int}: *N*/*A*[a])	Total: 12492 Unique: 1812 (R_{int}: 0.0509)
R_1[b]; wR_2[c]	0.0714; 0.2239	0.0836; 0.2241	0.0387; 0.1187
GOF[d]	1.050	1.039	1.058
Max./Min. peak I[d] / Å^3	4.55 e$^-$/−3.38 e$^-$	1.81 e$^-$/−1.58 e$^-$	1.71 e$^-$/−1.49 e$^-$

[a]: Not available because of the twin analyses. [b]: For data with $I > 2.00\sigma(I)$. [c]: For all reflection data. [d]: Goodness of Fit.

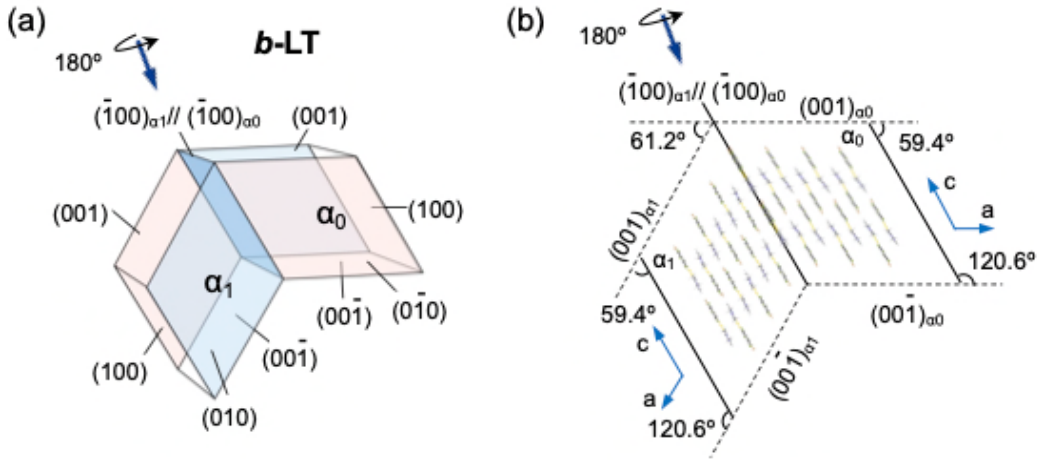

Figure. S20. The crystal face indices and packing arrangements of ***b*-LT**.

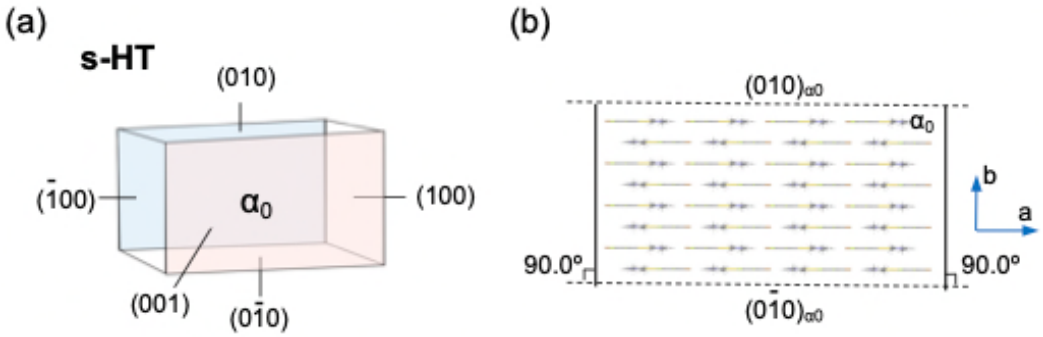

Figure. S21. The crystal face indices and packing arrangements of ***s*-HT**.

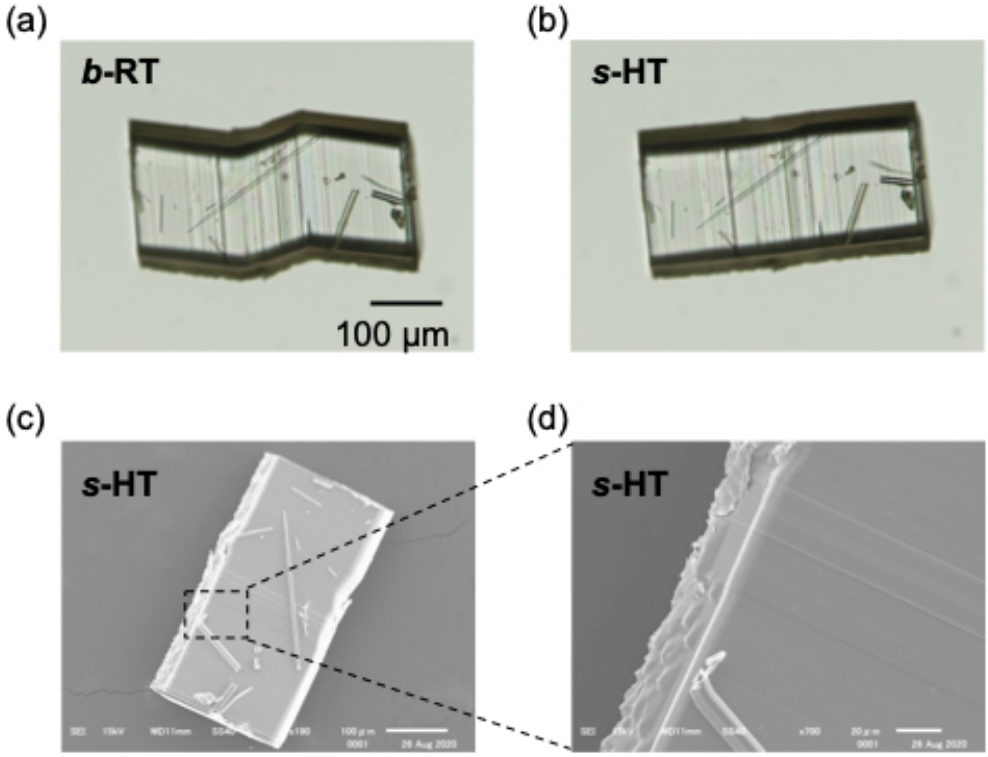

Figure S22. Photographs of ***b*-RT** upon heating to recover the original straight shape through the phase transition into ***s*-HT**. (a, b) Photographic image of ***b*-RT** and ***s*-HT**. (c, d) SEM images of ***s*-HT**.

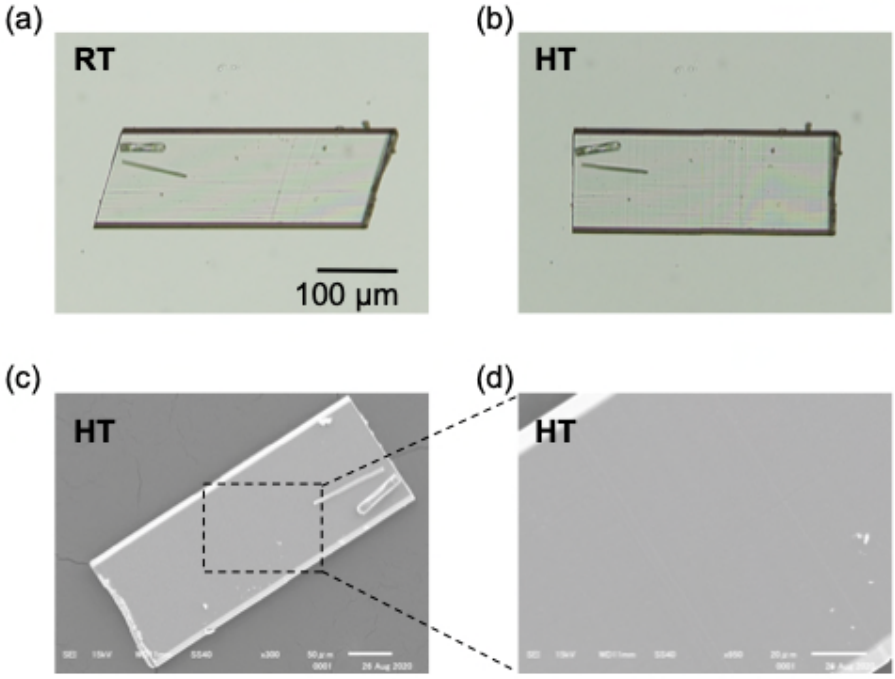

Figure S23. A crystal **RT** transformed into **HT** upon heating. (a, b) Photographic images of **RT** and **HT**. (c, d) SEM images of **HT**.

8. NMR spectra

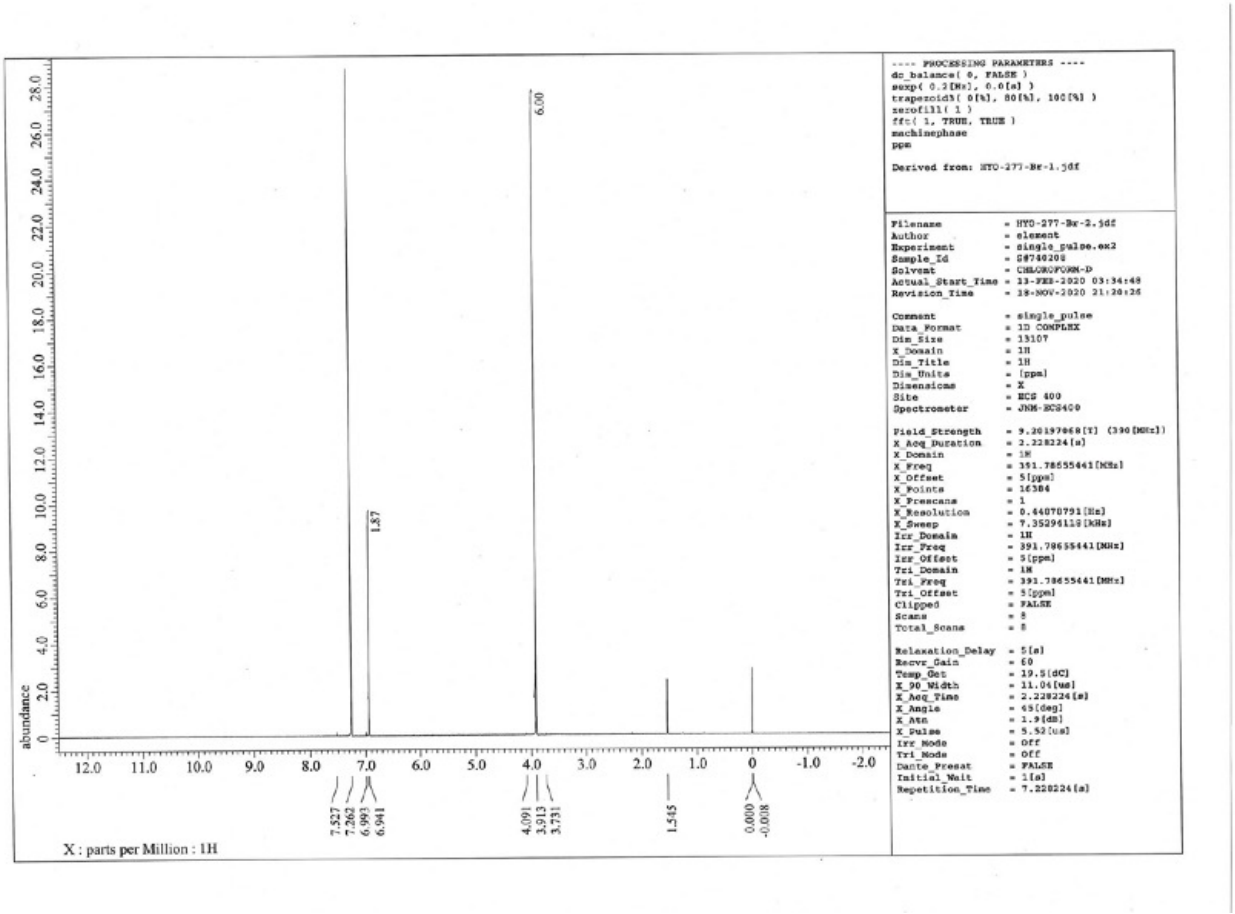

Figure S24 ^{1}H NMR spectrum of **1j** in $CDCl_3$.

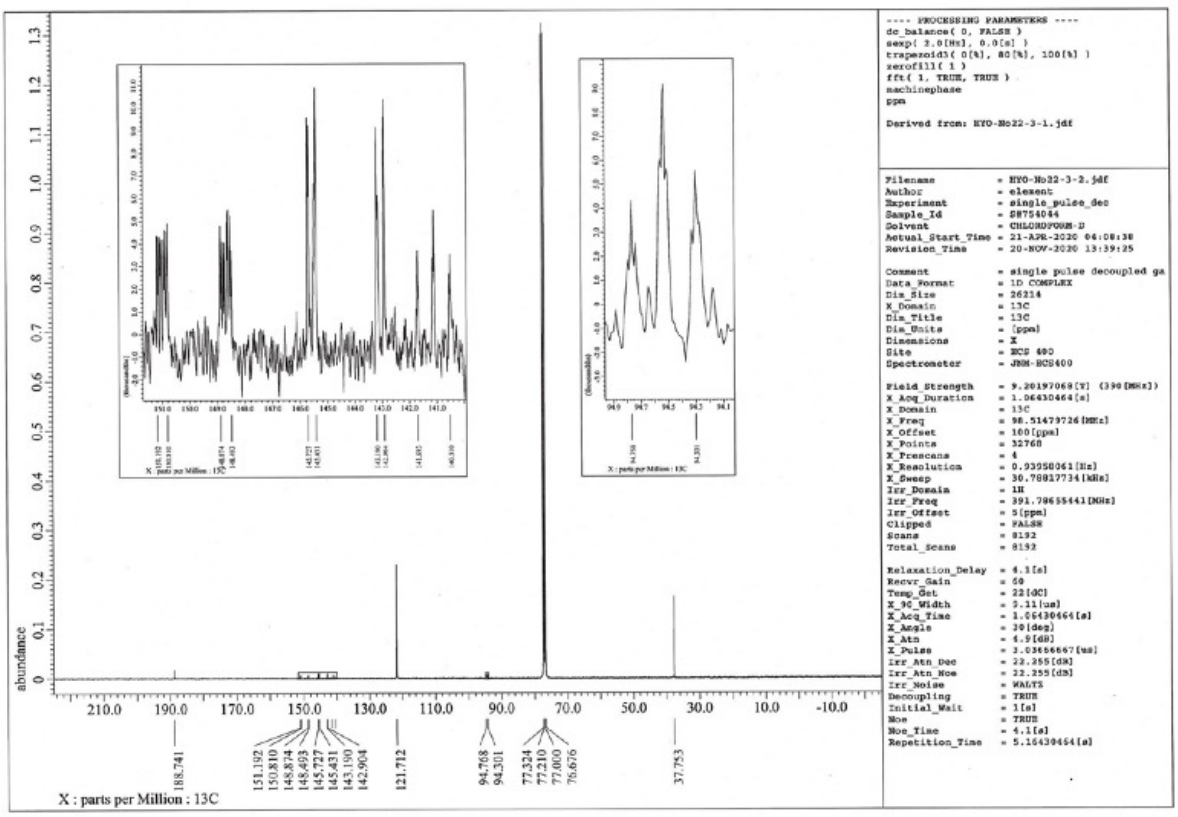

Figure S25 ^{13}C NMR spectrum of **1j** in $CDCl_3$.

3.6 References

1. Chang, L. C.; Read, T. A. Plastic Deformation and Diffusionless Phase Changes in Metals — the Gold-Cadmium Beta Phase. *Transactions of the AIME*, 1951, **189**, 47–52.
2. Sun, L.; Huang, W. M.; Ding, Z.; Zhao, Y.; Wang, C. C.; Purnawali, H.; Tang, C. Stimulus-Responsive Shape Memory Materials: A review. *Mater. Des.* **2012**, *33*, 577–640.
3. Jani, J. M.; Leary, M.; Subic, A.; Gibson, M. A. A Review of Shape Memory Alloy Research, Applications and Opportunities. *Mater. Des.* **2014**, *56*, 1078–1113.
4. Koerner, H.; Price, G.; Pearce, N. A.; Alexander, M.; Vaia, R. A. Remotely Actuated Polymer Nanocomposites—Stress-Recovery of Carbon-Nanotube-Filled Thermoplastic Elastomers. *Nat. Mater.* **2004**, *3*, 115–120.
5. Huang, W. M.; Yang, B.; An, L.; Li, C.; Chan, Y. S. Water-Driven Programmable Polyurethane Shape Memory Polymer: Demonstration and Mechanism. *Appl. Phys. Lett.* **2005**, *86*, 114105.
6. Lendlein, A.; Jiang, H.; Jünger, O.; Langer, R. Light-Induced Shape-Memory Polymers. *Nature* **2005**, *434*, 879–882.
7. Mohr, R.; Kratz, K.; Weigel, T.; Lucka-Gabor, M.; Moneke, M.; Lendlein, A. Initiation of Shape-Memory Effect by Inductive Heating of Magnetic Nanoparticles in Thermoplastic Polymers. *Proc. Natl Acad. Sci. USA* **2006**, *103*, 3540–3545.
8. Liu, C.; Qin, Q.; Mather, P. T. Review of Progress in Shape-Memory Polymers. *J. Mater. Chem.* **2007**, *17*, 1543–1558.
9. Dotter, C. T.; Buschmann, R. W.; McKinney, M. K.; Rösch, J. Transluminal Expandable Nitinol Coil Stent Grafting: Preliminary Report. *Radiology* **1983**, *147*, 259–260.
10. Lendlein, A.; Langer, R. Biodegradable, Elastic Shape-Memory Polymers for Potential Biomedical Applications. *Science* **2002**, *296*, 1673–1676.
11. Yakacki, C. M.; Shandas, R.; Safranski, D.; Ortega, A. M.; Sassaman, K.; Gall, K. Strong, Tailored, Biocompatible Shape-Memory Polymer Networks. *Adv. Funct. Mater.* **2008**, *18*, 2428–2435.
12. Das, D.; Jacobs, T.; Barbour, L. J. Exceptionally Large Positive and Negative Anisotropic Thermal Expansion of an Organic Crystalline Material. *Nat. Mater.* **2010**, *9*, 36–39.
13. Sahoo, S. C.; Sinha, S. B.; Kiran, M. S. R. N.; Ramamurty, U.; Dericioglu, A. F.; Reddy, C. M.; Naumov, P. Kinematic and Mechanical Profile of the Self-Actuation of Thermosalient Crystal Twins of 1,2,4,5-Tetrabromobenzene: A Molecular Crystalline Analogue of a Bimetallic Strip. *J. Am. Chem. Soc.* **2013**, *135*, 13843–13850.
14. Yao, Z.-S.; Mito, M.; Kamachi, T.; Shiota, Y.; Yoshizawa, K.; Azuma, N.; Miyazaki, Y.;

Takahashi, K.; Zhang, K.; Nakanishi, T.; Kang, S.; Kanegawa, S.; Sato, O. Molecular Motor-driven Abrupt Anisotropic Shape Change in a Single Crystal of a Ni Complex. *Nat. Chem.* **2014**, *6*, 1079–1083.

15. Su, S.-Q.; Kamachi, T.; Yao, Z.-S.; Huang, Y.-G.; Shiota, Y.; Yoshizawa, K.; Azuma, N.; Miyazaki, Y.; Nakano, M.; Maruta, G.; Takeda, S.; Kang, S.; Kanegawa, S.; Sato, O. Assembling an Alkyl Rotor to Access Abrupt and Reversible Crystalline Deformation of a Cobalt(II) Complex. *Nat. Commun.* **2015**, *6*, 8810.
16. Commins, P.; Desta, I. T.; Karothu, D. P.; Panda, M. K.; Naumov, P. Crystals on the Move: Mechanical Effects in Dynamic Solids. *Chem. Commun.*, **2016**, *52*, 13941–13954.
17. Karothu, D. P.; Weston, J.; Desta, I. T.; Naumov, P. Shape-memory and Self-healing Effects in Mechanosalient Molecular Crystals. *J. Am. Chem. Soc.* **2016**, *138*, 13298–13306.
18. Chung, H.; Dudenko, D.; Zhang, F.; D'Avino, G.; Ruzié, C.; Richard, A.; Schweicher, G.; Cornil, J.; Beljonne, D.; Geerts, Y.; Diao, Y. Rotator Side Chains Trigger Cooperative Transition for Shape and Function Memory Effect in Organic Semiconductors. *Nat. Commun.* **2018**, *9*, 278.
19. Seki, T.; Mashimo, T.; Ito, H. Anisotropic Strain Release in a Thermosalient Crystal: Correlation Between the Microscopic Orientation of Molecular Rearrangements and the Macroscopic Mechanical Motion. *Chem. Sci.* **2019**, *10*, 4185–4191.
20. Gupta, P.; Karothu, D. P.; Ahmed, E.; Naumov, P.; Nath, N. K. Thermally Twistable, Photobendable, Elastically Deformable, and Self- Healable Soft Crystals. *Angew. Chem. Int. Ed.* **2018**, *57*, 8498–8502.
21. Li, L.; Commins. P.; Al-Handawi, M. B.; Karothu, D. P.; Halabi, J. M.; Schramm, S.; Weston, J.; Rezgui, R.; Naumov, P. Martensitic Organic Crystals as Soft Actuators. *Chem. Sci.* **2019**, *10*, 7327–7332.
22. Duan, Y.; Semin, S.; Tinnemans, P.; Cuppen, H.; Xu, J.; Rasing, T. Robust Thermoelastic Microactuator Based on an Organic Molecular Crystal. *Nat. Commun.* **2019**, *10*, 4573.
23. Srirambhatla, V. K.; Guo, R.; Dawson, D. M.; Price, S. L.; Florence, A. J. Reversible, Two-Step Single-Crystal to Single-Crystal Phase Transitions between Desloratadine Forms I, II, and III. *Cryst. Growth Des.* **2020**, *20*, 1800–1810.
24. Park, S. K.; Diao, Y. Martensitic Transition in Molecular Crystals for Dynamic Functional Materials. *Chem. Soc. Rev.* **2020**, *49*, 8287–8314.
25. Kobatake, S.; Takami, S.; Muto, H.; Ishikawa, T.; Irie, M. Rapid and Reversible Shape Changes of Molecular Crystals on Photoirradiation. *Nature* **2007**, *446*, 778–781.

26. Panda, M. K.; Runčevski, T.; Sahoo, S. C.; Belik, A. A.; Nath, N. K.; Dinnebier, R. E.; Naumov, P. Colossal Positive and Negative Thermal Expansion and Thermosalient Effect in a Pentamorphic Organometallic Martensite. *Nat. Commun.* **2014**, *5*, 4811.
27. Jin, M.; Yamamoto, S.; Seki, T.; Ito, H.; Garcia-Garibay, M. A. Anisotropic Thermal Expansion as the Source of Macroscopic and Molecular Scale Motion in Phosphorescent Amphidynamic Crystals. *Angew. Chem. Int. Ed.* **2019**, *58*, 18003–18010.
28. Mutai, T.; Sasaki, T.; Sakamoto, S.; Yoshikawa, I.; Houjou, H.; Takamizawa, S. A Superelastochromic Crystal. *Nat. Commun.* **2020**, *11*, 1824.
29. Kitagawa, D.; Tsujioka, H.; Tong, F.; Dong, X.; Bardeen, C. J.; Kobatake, S. Control of Photomechanical Crystal Twisting by Illumination Direction. *J. Am. Chem. Soc.* **2018**, *140*, 4208–4212.
30. Saha, S.; Mishra, M. K.; Reddy, C. M.; Desiraju, G. R. From Molecules to Interactions to Crystal Engineering: Mechanical Properties of Organic Solids. *Acc. Chem. Res.* **2018**, *51*, 2957–2967.
31. Das, S; Mondal, A.; Reddy, C. M. Harnessing molecular rotations in plastic crystals: a holistic view for crystal engineering of adaptive soft materials. *Chem. Soc. Rev.*, 2020, **49**, 8878–8896.
32. Naumov, P.; Karothu, D. P.; Ahmed, E.; Catalano, L.; Commins, P.; Halabi, J. M.; Al-Handawi, M. B.; Li, L. The Rise of the Dynamic Crystals. *J. Am. Chem. Soc.* **2020**, *142*, 13256–13272.
33. Karothu, D. P.; Halabi, J. M.; Ahmed, E.; Ferreira, R.; Spackman, P. R.; Spackman, M. A.; Naumov, P. Global Analysis of the Mechanical Properties of Organic Crystals. Angew. Chem. Int. Ed. **2022**, e202113988.
34. Karothu, D. P.; Weston, J.; Desta, I. T.; Naumov, P. Shape-Memory and Self-Healing Effects in Mechanosalient Molecular Crystals. *J. Am. Chem. Soc.* **2016**, *138*, 13298–13306.
35. Takamizawa, S.; Takasaki, Y. Shape-Memory Effect in an Organosuperelastic Crystal. *Chem. Sci.* **2016**, *7*, 1527–1534.
36. Abe, Y.; Karasawa, S.; Koga, N. Crystal Structures and Emitting Properties of Trifluoromethylaminoquinoline Derivatives: Thermal Single-Crystal-to-Single-Crystal Transformation of Polymorphic Crystals That Emit Different Colors. *Chem. Eur. J.* **2012**, *18*, 15038–15048.
37. Gu, X.; Yao, J.; Zhang, G.; Yan, Y.; Zhang, C.; Peng, Q.; Liao, Q.; Wu, Y.; Xu, Z.; Zhao, Y.; Fu, H.; Zhang, D. Polymorphism-Dependent Emission for Di(*p*-methoxylphenyl)dibenzofulvene and Analogues: Optical Waveguide/Amplified Spontaneous Emission Behaviors. *Adv. Funct. Mater*. **2012**, *22*, 4862–4872.
38. Seki, T.; Ozaki, T.; Ohkura, T.; Asakura, K.; Sakon, A.; Uekusa, H.; Ito, H. Interconvertible

Multiple Photoluminescence Color of a Gold(I) Isocyanide Complex in the Solid State: Solvent-Induced Blue-Shifted and Mechano-Responsive Red-Shifted Photoluminescence. *Chem. Sci.* **2015**, *6*, 2187–2195.

39. Seki, T.; Sakurada, K.; Muromoto, M.; Seki, S.; Ito, H. Detailed Investigation of the Structural, Thermal, and Electronic Properties of Gold Isocyanide Complexes with Mechano-Triggered Single-Crystal-to-Single-Crystal Phase Transitions. *Chem. Eur. J.* **2016**, *22*, 1968–1978.
40. Seki, T.; Takamatsu, Y.; Ito, H. A Screening Approach for the Discovery of Mechanochromic Gold(I) Isocyanide Complexes with Crystal-to-Crystal Phase Transitions. *J. Am. Chem. Soc.* **2016**, *138*, 6252–6260.
41. Du, X.; Xu, F.; Yuan, M.-S.; Xue, P.; Zhao, L.; Wang, D.-E.; Wang, W.; Tu, Q.; Chen, S.-W.; Wang, J. Reversible Luminescence Color Switching in the Crystal Polymorphs of 2,7-bis(2′-methyl-[1,1′- biphenyl]-4-yl)-fluorenone by Thermal and Mechanical Stimuli. *J. Mater. Chem. C,* **2016**, *4*, 8724–8730.
42. Abe, Y.; Savikhin, V.; Yin, J.; Grimsdale, A. C.; Soci, C.; Toney, M. F.; Lam, Y. M. Unique Reversible Crystal-to-Crystal Phase Transition Structural and Functional Properties of Fused Ladder Thienoarenes. *Chem. Mater*. **2017**, *29*, 7686–7696.
43. Jin, M.; Chung, T. S.; Seki, T.; Ito, H.; Garcia-Garibay, M. A. Phosphorescence Control Mediated by Molecular Rotation and Aurophilic Interactions in Amphidynamic Crystals of 1,4-Bis[tri-(*p*-fluorophenyl)phosphane-gold(I)-ethynyl]benzene. *J. Am. Chem. Soc.* **2017**, *139*, 18115–18121.
44. Jin, M.; Sumitani, T.; Sato, H.; Seki, T.; Ito, H. Mechanical-Stimulation-Triggered and Solvent-Vapor-Induced Reverse Single-Crystal-to-Single-Crystal Phase Transitions with Alterations of the Luminescence Color. *J. Am. Chem. Soc.* **2018**, *140*, 2875–2879.
45. Seki, T.; Ida, K.; Ito, H. A *meta*-diisocyanide Benzene-Based Aryl Gold Isocyanide Complex Exhibiting Multiple Solid-State Molecular Arrangements and Luminescent Mechanochromism. *Mater. Chem. Front.* **2018**, *2*, 1195–1200.
46. Yamakado, T.; Otsubo, K.; Osuka, A.; Saito, S. Compression of a Flapping Mechanophore Accompanied by Thermal Void Collapse in a Crystalline Phase. *J. Am. Chem. Soc.* **2018**, *140*, 6245–6248.
47. Ge, C.; Liu, J.; Ye, X.; Han, Q.; Zhang, L.; Cui, S.; Guo, Q.; Liu, G.; Liu, Y.; Tao, X. Visualization of Single-Crystal-to-Single-Crystal Phase Transition of Luminescent Molecular Polymorphs. *J. Phys. Chem. C* **2018**, *122*, 15744–15752.
48. Jiang, M.-S.; Tao, Y,-H.; Wang, Y.-W.; Lu, C.; Young, D. J.; Lang, J.-P.; Ren, Z.-G. Reversible

Solid-State Phase Transitions between Au−P Complexes Accompanied by Switchable Fluorescence. *Inorg. Chem*. **2020**, *59*, 3072–3078.

49. Sun, H.; Wei, J.-H.; Xu, L.-H.; Jiang, Y.; Miao, B.-X.; Ni, Z.-H. Temperature- and Solvent-Induced Solid-State Emission Changes and AIEE Property of a Pyrene-Based Sulfide Compound. *Dyes and Pigments* **2020**, *177*, 108299.
50. Liu, Y.; Li, A.; Xu, S.; Xu, W.; Liu, Y.; Tian, W.; Xu, B. Reversible Luminescent Switching in an Organic Cocrystal: Multi-Stimuli-Induced Crystal-to-Crystal Phase Transformation. *Angew. Chem. Int. Ed.* **2020**, *59*, 15098–15103.
51. Jin, M.; Ando, R.; Jellen, M. J.; Garcia-Garibay, M. A.; Ito, H. Encapsulating *N*-Heterocyclic Carbene Binuclear Transition-Metal Complexes as a New Platform for Molecular Rotation in Crystalline Solid-State. *J. Am. Chem. Soc.* **2021**, *143*, 1144–1153.
52. Seki, T.; Feng, C.; Kashiyama, K.; Sakamoto, S.; Takasaki, Y.; Sasaki, T.; Takamizawa, S.; Ito, H. Photoluminescent Ferroelastic Molecular Crystals. *Angew. Chem. Int. Ed.* **2020**, *59*, 8839–8843.
53. Mir, S. H.; Takasaki, Y.; Engel, E. R.; Takamizawa, S. Ferroelasticity in an Organic Crystal: A Macroscopic and Molecular Level Study. *Angew. Chem. Int. Ed.* **2017**, *56*, 15882–15885.
54. Mir, S. H.; Takasaki, Y.; Takamizawa, S. An Organoferroelasticity Driven by Molecular Conformational Change. *Phys. Chem. Chem. Phys.* **2018**, *20*, 4631–4645.
55. Engel, E. R.; Takasaki, Y.; Mir, S. H.; Takamizawa, S. Twinning Ferroelasticity Facilitated by the Partial Flipping of Phenyl Rings in Single Crystals of 4,4′-dicarboxydiphenyl ether. *R. Soc. Open Sci.* **2018**, *5*, 171146.
56. Mir, S. H.; Takasaki, Y.; Engel, E. R.; Takamizawa, S. Controllability of Coercive Stress in Organoferroelasticity by the Incorporation of a Bulky Flipping Moiety in Molecular Crystals. *CrystEngComm.* **2018**, *20*, 3807–3811.
57. Mir, S. H.; Takasaki, Y.; Engel, E. R.; Takamizawa, S. Enhancement of Dissipated Energy by Large Bending of an Organic Single Crystal Undergoing Twinning Deformation. *RSC Adv.* **2018**, *8*, 21933–21936.
58. Engel, E. R.; Takamizawa, S. Versatile Ferroelastic Deformability in an Organic Single Crystal by Twinning About a Molecular Zone Axis. *Angew. Chem. Int. Ed.* **2018**, *57*, 11888–11892.
59. Takamizawa, S.; Takasaki, Y. Versatile Shape Recoverability of Odd-numbered Saturated Long-Chain Fatty Acid Crystals. *Cryst. Growth Des.* **2019**, *19*, 1912–1920.
60. Sakamoto, S.; Sasaki, T.; Sato-Tomita, A.; Takamizawa, S. Shape Rememorization of an Organosuperelastic Crystal via Superelasticity–Ferroelasticity Interconversion. *Angew. Chem.*

Int. Ed. **2019**, *58*, 13722–13726.

61. Sasaki, T.; Sakamoto, S.; Takasaki, Y.; Takamizawa, S. A Multi-Directional Superelastic Organic Crystal via Versatile Ferroelastical Manipulation. *Angew. Chem. Int. Ed.* **2020**, *59*, 4340–4343.
62. Sasaki, T.; Sakamoto, S.; Takamizawa, S. Organoferroelastic Crystal Prepared by Supramolecular Synthesis. *Cryst. Growth Des.* **2020**, *20*, 1935–1939.
63. Sasaki, T.; Sakamoto, S.; Nishizawa, K.; Takamizawa, S. Ferroelasticity with a Biased Hysteresis Loop in a Co-Crystal of Pimelic Acid and 1,2-di(4-pyridyl)ethane. *Cryst. Growth Des.* **2020**, *20*, 3913–3917.
64. Park, S. K.; Sun, H.; Chung, H.; Patel, B. B.; Zhang, F.; Davies, D. W.; Woods, T. J.; Zhao, K.; Diao, Y. Super- and Ferroelastic Organic Semiconductors for Ultraflexible Single-Crystal Electronics. *Angew. Chem. Int. Ed.* **2020**, *59*, 13004–13012.
65. Sasaki, T.; Sakamoto, S.; Takamizawa, S. Flash Shape-Memorization Processing and Inversion of a Polar Direction in a Chiral Organosuperelastic Crystal of 1,3,5-Tricyanobenzene. *Cryst. Growth Des.* **2020**, *20*, 4621–4626.
66. Takasaki, Y.; Sasaki, T.; Takamizawa, S. Temperature-Diversified Anisotropic Superelasticity and Ferroelasticity in a 3-methyl-4-nitrobenzoic Acid Crystal. *Cryst. Growth Des.* **2020**, *20*, 6211–6216.
67. Sheldrick, G. M. SHTLXT - Integrated space-group and crystal-structure determination. *Acta Cryst.* **2015**, *A71*, 3–8.
68. Dolomanov, O. V.; Bourhis, L. J.; Gildea, R. J.; Howard, J. A. K.; Puschmann, H. OLEX2: a complete structure solution, refinement and analysis program. *J. Appl. Crystallogr.* **2009**, *42*, 339–341.
69. A. Johnson M. C. Gimeno, *Chem. Commun*. **2016**, *52*, 9664–9667.
70. Bayón, B.; Coco, S.; Espinet, P.; Fernández-Mayordomo, C.; Martín-Alvarez, J. M. *Inorg. Chem.* **1997**, *36*, 2329–2334.

IV Summary of This Thesis

Flexible molecular crystals, ordered materials capable of adapting to variable operating and environmental conditions through deformation to gain the ability to move or perform work, are rapidly forming a new research direction in materials science. Recently, organic ferroelastic and superelastic crystals were discovered as new classes of flexible solid materials. The research for such molecular crystals is at an early stage, and only a few examples of superelastic and ferroelastic crystals were reported. In this thesis, I focused on the development of luminescent ferroelastic and shape-memory organic materials. Furthermore, it provides more insight into the structural characteristics and deformation mechanisms of superelasticity and ferroelasticity.

In Chapter 2, I described the first photoluminescent ferroelastic molecular crystals. In this work, I prepared various structurally simple NHC gold complexes and discovered an NHC gold(I) complex that exhibits ferroelastic behavior as well as photoluminescence for the first time. Moreover, I found that the ferroelastic crystals undergo a ferroelastic to superelastic transition at low temperatures. Based on single-crystal X-ray diffraction (XRD) measurements, a comparison with the single-crystal structures of related NHC gold(I) complexes without ferroelasticity elucidates the structural origin of the ferroelastic behavior.

In Chapter 3, I described a reversible multi-stage shape-changing effect after mechanical deformation in a molecular crystal. The interesting mechanical properties of gold (I) complexes described in Chapter 2 suggested that the further screening of gold (I) complexes can give an opportunity for the development shape memory effect of gold(I) complexes by combining the ferro- and super elasticity and thermal phase changes. In this work, I discovered an NHC gold(I) complex with a reversible multi-stage shape-changing effect after mechanical deformation with luminescent color changes. Based on XRD, spectroscopic and thermal analyses, and mechanical property measurements, the origin of this unique stimulus-responsivity was discussed.

Through this thesis, I developed photoluminescent ferroelastic and shape-changing organic materials in gold(I) complexes. As demonstrated in the thesis, crystals composed of gold complexes tend to exhibit pronounced phosphorescent properties, which allow for changes in the luminescent color associated with shape-changing phenomena. This study also revealed the structural origin of the ferroelastic behavior and the multi-stage shape-changing effect. The development of luminescent ferroelastic and shape-changing materials and insight into their mechanisms will facilitate the further development of new flexible organic materials.

List of Publication

Chapter II:

Photoluminescent Ferroelastic Molecular Crystals

Seki, T.*; Feng, C.; Kashiyama, K.; Sakamoto, S.; Takasaki, Y.; Sasaki, T.; Takamizawa, S.*; Ito, H.* *Angew. Chem., Int. Ed.* **2020**, *59*, 8839–8843.

Chapter III:

Mechanical deformation and multiple thermal restoration of organic crystals: reversible multi-stage shape-changing effect with luminescence-color changes

Feng, C.; Seki, T.*; Sakamoto, S.; Sasaki, T.; Takamizawa, S.*; Ito, H.* *Chem. Sci.* **2022**, *13*, 9544-9551.

Other publicaitons:

Efficient Access to Materials-Oriented Aromatic Alkynes via the Mechanochemical Sonogashira Coupling of Solid Aryl Halides with Large Polycyclic Conjugated Systems

Gao, Y.; Feng, C.; Seo, T.; Kubota, K.; Ito, H. *Chem. Sci.* **2022***, 13,* 430–438.

Stereospecific Synthesis of Silicon-Stereogenic Optically Active Silylboranes and their Application to Synthesis of Chiral Organosilanes

Wang, X.; Feng, C.; Kubota, K.; Ito, H. *Chem. Rxiv*. **2022**.

DOI: 10.26434/chemrxiv-2022-ft3c6

A New Structural Motif for NIR and Mechano-Thermochromic Emission: Gold(I) Iodide Complexes with a Thiazole-Based NHC Ligand

Matsuura, S.; Ozawa, Y.; Feng, C.; Jin, M.; Seki, T.; Ito, H. *manuscript in preparation.*

Searching flexible gold isocyanide complexes by halogen scan

Feng, C.; Jin, M.; Ito, H. *manuscript in preparation.*

Acknowledgements

The Studies presented in this thesis have been carried out under the direction of Professor Doctor Hajime Ito *at the Faculty of Engineering, Hokkaido University and Institute for Chemical Reaction Design and Discovery (WPI-ICReDD), Hokkaido University* during 2018–2023. I received financial support from the Leading Graduate Schools Program (Hokkaido University's "Ambitious Leaders Program"). This work was supported by the Hokkaido University Ambitious Leaders Program.

First, I would like to express my deepest gratitude to Professor Hajime Ito, whose constant guidance, tremendous support, and insightful comments during the research process have been invaluable. I also wish to express my thanks to Associate Professor Tatsuo Ishiyama, Lecturer Tomohiro Seki (currently at Shizuoka University), Associate Professor Koji Kubota, and Associate Professor Mingoo Jin for their sound advice, insightful suggestions and encouragement during the research process. I would also like to express my great appreciation to Kentaro Kashiyama, Shunichi Sakamoto, Dr. Yuichi Takasaki, Dr. Toshiyuki Sasaki, and Professor Satoshi Takamizawa for their help in the measurement of strain-stress curves. I would also like to thank Assistant Professor Hirotaka Hosoi for teaching me to measure surface potential and helping me in this regard. And I would also like to thank Professor Hiroshi Hirata for teaching me about electron spin resonance measurements.

Finally, I would like to express my deepest gratitude to my wife for giving up so much of her research time to stay at home and take care of our child. And I am grateful that my little one is exceptionally well behaved so that I can get enough sleep.